Doctoral dissertation

Feasible material design of Si anodes for high-energy and advanced Li-ion batteries

Yoonkwang Lee

Department of Energy Engineering

(Battery Science and Technology)

Graduate School of UNIST

2020

Feasible material design of Si anodes for high-energy and advanced Li-ion batteries

Yoonkwang Lee

Department of Energy Engineering
(Battery Science and Technology)

Graduate School of UNIST

Feasible material design of Si anodes for high-energy and advanced Li-ion batteries

A thesis/dissertation
submitted to the Graduate School of UNIST
in partial fulfillment of the
requirements for the degree of
Doctor of Philosophy in Energy Engineering

Yoonkwang Lee

6. 18. 2020

Approved by

Advisor
Jaephil Cho

Feasible material design of Si anodes for high-energy and advanced Li-ion batteries

Yoonkwang Lee

This certifies that the thesis/dissertation of Yoonkwang Lee is approved.

6. 18. 2020

Advisor: Jaephil Cho

Hyun-Kon Song

Nam-Soon Choi

Kyeong-Min Jeong

Sung Youb Kim

Abstract

The unprecedentedly expanded use of energy storage devices has accentuated the requisition of improved energy density and long-life span lithium-ion batteries (LIBs). Though the commercial graphite demonstrates low working potential (versus Li^+/Li), exceptional initial Coulombic efficiency, electric conductivity, and cycle stability, unfortunately, commercially applied graphite anodes are imminent their theoretical capacity (372 mAh g^{-1}). A variety of anodes candidates alternating the graphite with higher capacity have been studied to overcome its capacity limit. Furthermore, explosive demands for sustainable electromobility with high-energy density have motivated tremendous researchers to improve next-generation anode materials, but high gravimetric and volumetric capacity anodes retain obvious limits in the stability of the cell properties.

In terms of theoretical gravimetric capacity, silicon has been illuminated as the most promising candidate for the specific capacity, which surpasses more than 10 times comparing to that of graphite. Besides, silicon exhibits low operation voltage, low cost and abundant in the earth. Despite these outstanding advantages, the application of Si as practical anodes still has been avoided by its fundamental problem of volume changes during the charge and discharge procedure. These extreme volume changes could cause material fracture, resulting in electrical contact loss from the current collector and formation of fresh surface to electrolyte. The fresh surface will be provided to reactive site of solid electrolyte interphase (SEI) formation, ascribing excessive electrolyte consumption.

Recently, small quantity of Si applied batteries are produced with improved properties. And higher quantity of Si applied batteries has been commercialized in specific application such as power tools. For these reasons, a breakthrough strategy is required to utilize Si-dominant practical anodes. Previously reported void and nano engineering strategies have inherent problems in battery operation and commercial aspects. Enlarged particle size, densified morphology, high tap density, and low specific surface area should be contemplated for the rational active material design.

In terms of post-generation technologies, lithium metal anodes have been perceived due to its highest theoretical gravimetric (3,860 mAh g^{-1}) and volumetric (2,061 mAh cm^{-3}) capacity with the lowest potential (–3.04 V, SHE). Unfortunately, there are impregnable challenges to be solved by worldwide researchers to introduce the lithium metal anodes in commercial battery. Effortless dendritic Li formation causes fatal safety issues, accompanying the low cycling efficiency. To suppress the dendrite formation and stabilize the cyclability, vigorous efforts and various strategies have been devoted lately; electrolyte and additive improvement, protective materials to inhibit the dendrite formation, host materials for rational Li deposition, and lithiophilic materials addition for selective Li deposition. Nonetheless, the performance of lithium metal battery is still in the infancy level to be applied in practical batteries, remaining huge gap between academic state and commercial requirements.

In this dissertation, I describe brief interpretation of lithium ion batteries including principles and components of lithium ion batteries in chapter 1. Then, I briefly introduce the current and next generation anode materials for high energy density lithium ion batteries; Si-based anodes and Li metal anodes.

In chapter 2, I proposed high gravimetric and volumetric capacity composite anodes for next-generation lithium-ion batteries. I emphasized that nano and void-engineering strategies had showed intrinsic limit in fabrication of practical electrode condition. Achieving high electrode density is particularly paramount factor in terms of the commercial feasibility that the tap density of active material was enhanced to 1.1 g cm^{-3}. I introduced micron-sized double passivation layered Si/C design with restrictive lithiation state, based on finite element method calculation. The structure integrity was demonstrated under the industrial electrode fabrication with electrode density (1.6 g cm^{-3}), areal capacity (>3.5 mAh cm^{-2}), and electrode composition (additives < 4 wt%). Such design takes advantages in long-term cycling performances even at high gravimetric capacity (1400 mAh g^{-1}), withstanding the induced stress from Li insertion upon repeated cycling. We performed the 1 Ah pouch-type full-cell evaluation with high mass loading and electrode density (~3.75 mAh cm^{-2} and ~1.65 g cm^{-3}), which demonstrates superior cycle stability without rapid capacity drop during 800 cycles.

In chapter 3, I briefly reviewed lithium metal anodes, and described this work to overcome the current issue. We synthesized ion and electron conductive carbon structure, which contains enough space to accommodate metallic Li during plating process. Li is intensely light metal denoting 0.534 g/cm^3 density that the required dense lithium thickness is 14.6 μm for areal capacity (≥ 3 mAh/cm^2). The interconnected pore structure containing 500 nm pore and showing 0.2 g/cm^3 tap density takes merits in expanded potential area for Li deposition. To incorporate lithiophilic surface layer, thermal decomposed Si nano-layer was deposited uniformly with 3 nm. The lithiophilic lithiated Si (Li_xSi) alleviated the polarization that it could induce planar Li nucleation and continuous Li accumulation at inner pore and outer surface region, followed by dense and smooth Li plating in electrode. The volume expansion of the electrode at lithiated state of 3 mAh/cm^2 was just 30% from 27 μm to 35 μm because of the adequate pore volume. And lithiophilic layer induced electrode exhibited prolonged lifespan and high power at high current density comparing to carbon frame without the Si layer.

Contents

List of Figures

Chapter 1

Figure 2-16 XPS spectra of Si 2p for (a) Si@SiO_2 and (b) Si@SiO_2@C.

Figure 2-17 Electrochemical and TEM elemental characterizations. (a) Elemental composition ratio of SCM and u-SCM by Si, O, and C elemental mappings (inset STEM images by ion slicing), (b) first-cycle voltage profiles for solely and blended electrodes of SCM and u-SCM, (c) discharge capacity and Coulombic efficiency for solely and blended electrodes of SCM and u-SCM, (d) Rate capabilities of SCM and u-SCM blending electrodes under various current densities: 0.72, 1.8, 3.6, 7.2 and 18 mA cm^{-2}.

Figure 2-18. Rate capabilities under various current densities: 0.2, 0.5, 1, 2 and 5C.

Figure 2-19 Electrochemical characterization of full-cells. (a) Full-cell test of SCM and u-SCM electrodes for 300 cycles and cycle life of reassembled cell with the fresh cathode and cycled SCM anode, (b) optical images of cycled anode and cathode, (c) discharge capacity of full-cell at first formation cycle and reassembled cycle, (d) first-cycle and reassembled cycle profiles of SCM applied full-cell, (e) discharge dQ/dv plot of initial and re-assembled formation cycle.

Figure 2-20 Re-assembled half-cell evaluation with cycled electrodes. (a) Voltage profiles of re-assembled SCM and (b) voltage profiles of re-assembled LCO with fresh Li foil after 300 cycles on the full-cell.

Figure 2-21 Re-assembled full-cell. Voltage profile of re-assembled full-cell with cycled u-SCM and fresh LCO after 300 cycles on the full-cell.

Figure 2-22 (a) Voltage profile of excessive C applied (e-SCM) Si/C micro particle (40 wt% blending for 650 mAh g^{-1}) and (b) full-cell cycle test for 300 cycles.

Figure 2-23 Re-assembled half-cell evaluation. Discharge dQ/dv plot of initial and re-assembled formation cycle with cycled SCM and fresh Li foil after 300 cycles on the full-cell.

Figure 2-24 Electrochemical characterization of full-cells. (a) 1 Ah full-cell test of SCM electrode at 25 and 50 ℃, (b) electrode swelling behaviors during 50 cycles.

Figure 2-25 Rate capability at room temperature (25 ℃). Discharge profiles of SCM applied 1 Ah full-cell under various current densities: 0.5, 1, 2, 3, 4 and 5C.

Figure 2-26 Scheme and cross-section analysis of post cycling electrodes. (a) Schematic illustration of the mechanical degradation and irreversible reaction effects in Si/C micro-particles during the long cycles. Cross-sectional SEM of u-SCM (b) bare and after 50 and 100 cycles, (c) after 300 cycles. Cross-sectional SEM of SCM (d) bare and after 50 and 100 cycles, (e) after 300 cycles. (f) Cross-sectional elements (Si, F and C) mapping of SCM after 100 cycles.

Figure 2-27 STEM cross-sectional images of cycled u-SCM (after 300 cycles) with EDS mapping for

List of tables

Chapter 1

Introduction of Lithium-ion batteries

1.1 Introduction

In today's society, advances in technology have facilitated the use of portable energy sources.[1-5] The existing representative portable energy source was fossil fuel and has been being supplied as a major energy since the industrial revolution. However, in recent years, by-products such as carbon dioxide (CO_2) and methane (CH_4) generated during the combustion of fossil fuels have highly threated the environment with potential risk. This has played a threatening role in global environmental change, declaring intensive management worldwide. The smartest way to suppress it is to lower their incidence rate. Therefore, enormous attentions have been focused on restraining the use of fossil fuels and using eco-friendly energy sources.[6,7] This motivates interests and development in renewable energy as in the (Fig. 1-1).

In addition to interest in renewable energy, electric devices in modern life, which are developing at an incredible speed, have increasingly expanded the need for a portable energy source. Battery system storing the energy by electrochemical procedure are attracting attention as an alternative.[8-10] Batteries are devices that convert the chemical energy into electrical energy, which have been applied since the 19th century with primary cell. A primary cell reaches its end of life just with once use. However, a battery being discarded after once use has obstacles to tale environmental benefits. Therefore, developing a battery that can be used repeatedly was required, which was defined as a secondary battery or rechargeable battery.[11-13] The discovery of lead acid batteries marked the beginning of the secondary battery. This is used as a battery for vehicles, but its heavy weight and the low energy showed limits in applicable fields. Such a low energy density battery is not suitable for the modern devices requiring high energy capacity and light weight. Furthermore, the target for vehicles, vessels and even aircraft obligates maximized energy density. The discovery of lithium-ion batteries has successfully achieved an improvement in energy density of secondary batteries and has been commercialized in many fields to date (Fig. 1-3). The rapid growth of the world battery market clearly demonstrates this. (Fig. 1-4).[14] In addition, LIBs have design flexibility to manufacture in various sizes and shapes according to the application, and the stability has been sustainedly improved.

LIBs have been getting the more attention as they begin to be applied to electric vehicles. Because

vehicles serve as a major provision consuming the fossil fuels. The development and dissemination of electric vehicles (EV) have accelerated the necessity of advanced LIBs,[15-18] and the battery has become a priority of the next generation of eco-friendly energy sources. Consolidating the EV proportion increasement in the next few decades became the worldwide principal goal. Along with this, the application fields of batteries are expended to the large-capacity energy storage systems.[19,20] To meet this, a high-performance battery of high energy and power density with superior stability is required. The enhanced energy density enables smaller and lighter batteries.[21-23] For this, the development of next-generation active materials will be the prerequisite, which will contribute to the expansion of LIB's application field.[24,25]

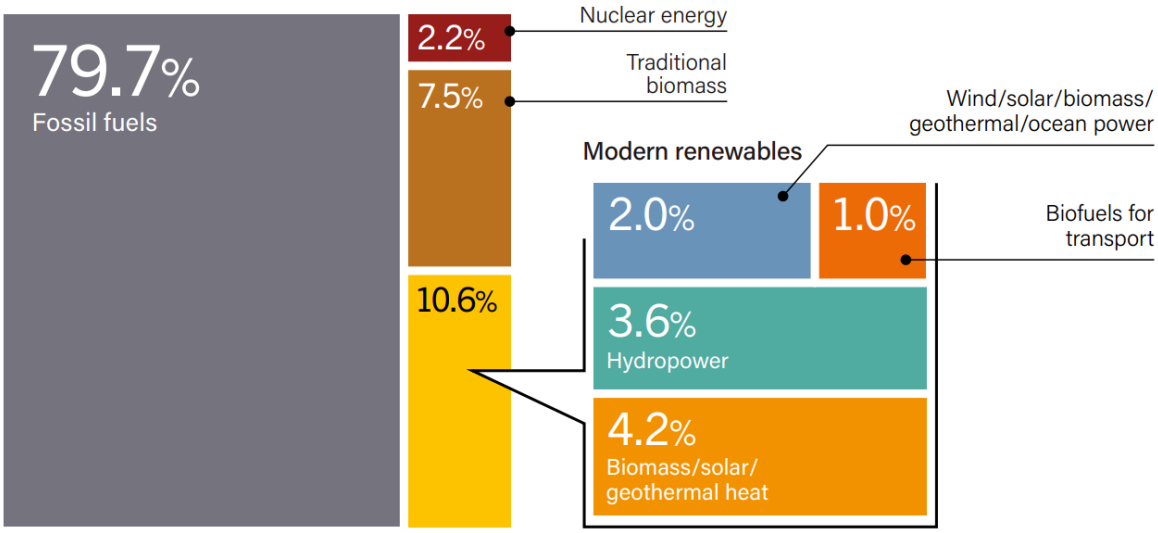

Figure 1-1. Estimated global renewable energy share of total final energy consumption.

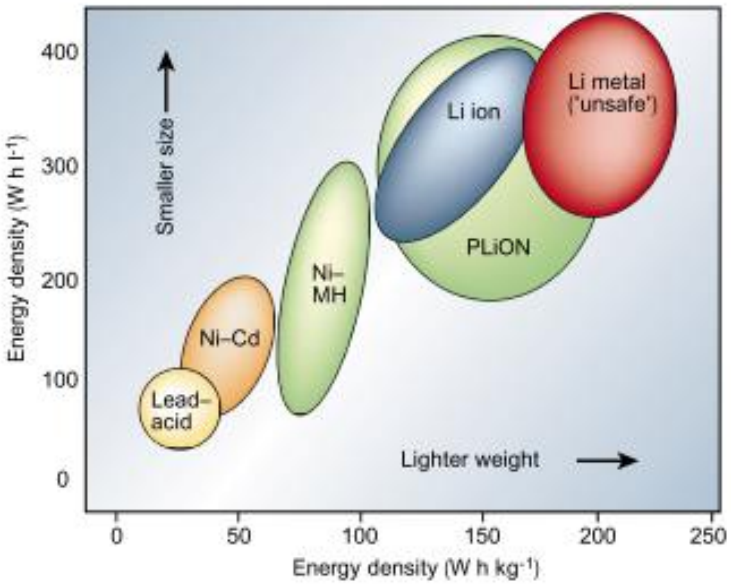

Figure 1-2. Comparison of various battery systems in terms energy density. 26

Nature **volume 414**, pages359–367(2001)

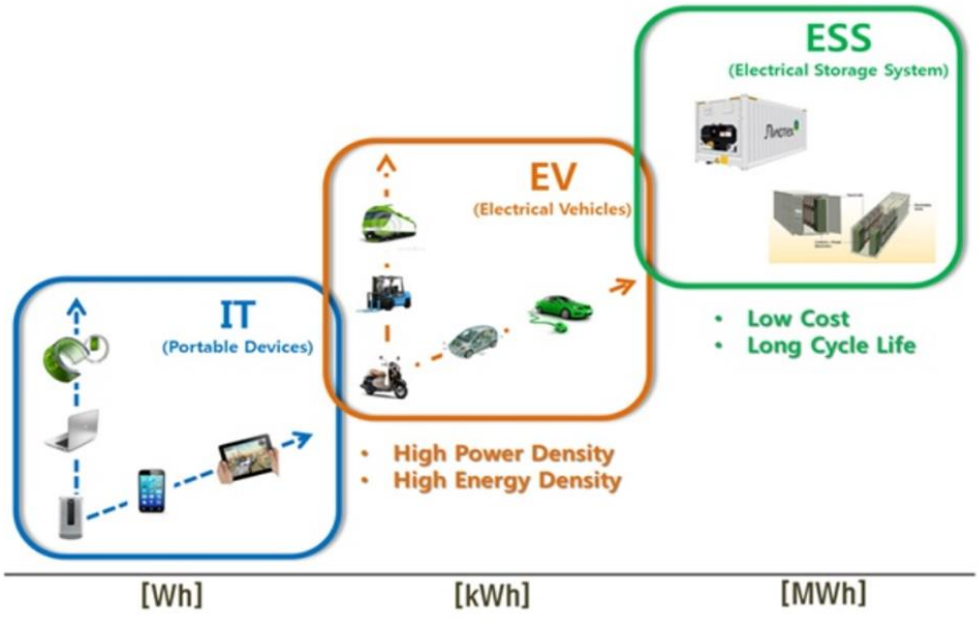

Figure 1-3. Fields adopting lithium-ion batteries and the required energy density of various applications.

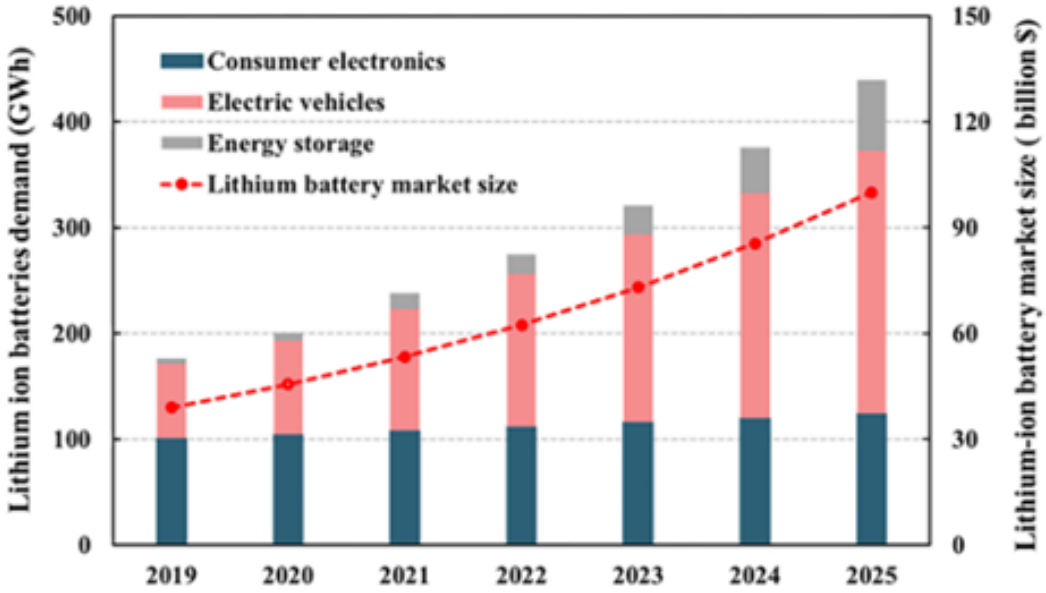

Figure 1-4. Global market size and demanded energy forecast on lithium ion battery applications.[26]

1.2 Principle of lithium ion battery

Basic principle

Fig. 1-5 illustrates typical lithium ion battery components and brief operation principles. Li-ion batteries are commonly constructed with negative electrode (anode) and positive electrode (cathode),[27] which are faced to each other and physically isolated by the separator. The separators are essential to prevent short circuits. Within these structural model, Li-ions transfers to anodes and cathodes during the charge and discharge process, leading the redox reaction ($Li^+ + e^- \leftrightarrow Li$) in both electrodes. Electrons generation will be transported through the external circuit by the potential difference and outer electric field. In contrast to electrons, Li ions should be transferred within the battery passing through the separator. The electrolyte, consisting of solvent and Li ion containing salt, gives an ionic conducting pathway, acting as transporter. In conventional LIBs, lithium transition metal oxide contains Li sources, acting as cathode materials. The Li ions consisting of the cathode transfers to anode parts at charging stage that the anode materials should have Li storage capability. A graphite is generally applied as anode materials, working as lithium storing materials by reduction of Li ion with the transported electrons.

Cathode

A cathode is the materials to be oxidized during the charge process, which means the materials lose electrons ($Li \rightarrow xLi^+ + xe^-$). By the oxidized process, the Li ions and electrons are provided, and the cathode exists as the delithiated state of metal oxide. During the charge procedure, the Li ions are transferred to counterpart electrode through the separator by electrolyte and the electrons are transported through external circuit. Then, they are reduced in anode materials. On the contrary, the reduction reaction receiving the Li ions and electrons from the anodes occurs at the cathode during the discharge step. Equal reaction occurs at anodes during the charging process. High specific capacities, tap density, chemical stability, stable cycle lifespan, and high operating potentials versus Li/Li^+ are required to cathode materials.

Numerous candidates of cathode active materials have been considered in terms of each advantages for LIBs. In general, classifications of the positive electrode are determined by their crystallographic structure. Typical structures can be categorized with olivine, layered and spinel structure, which determine the dimensional diffusion characteristics (Fig 1-6). The olivine structure represented by LiFePO4 has one-dimensional Li diffusion channel. Layered ($LiCoO_2$) and spinel ($LiMn_2O_4$) structured cathode demonstrate 2D and 3D Li diffusion channels, respectively.

From the early LIBs, the Lithium cobalt oxide ($LiCoO_2$) has been generally utilized as a cathode active material. LCO ($LiCoO_2$) provides high and stable operation voltage during the discharge process.

It also exhibits commercial feasibility in mass production that LCO is suitable for cathode materials. Though the LCO takes up substantial market share, high cost of cobalt raw materials brings about hindrance from a commercial point of view. Furthermore, different from the theoretical capacity, the available capacity is restricted due to its instability at highly delithiated state. that request the advanced cathode materials in terms of specific energy.

In this regard, the advanced cathode materials in terms of specific energy are desired. Ni-contained cathode materials are noticeable candidate with nest generation cathodes owing to its higher reversible capacity. In addition, for these materials, nickel element can reduce the amount of cobalt element by alternating it with Ni in the crystallographic structure (Fig. 1-7).[28] Even though their merits in commercial aspect, its high chemical instability of lithium nickel oxide ($LiNiO_2$) hinders the utilization for commercials LIBs. However, Ni-based compounds are widely challenge, in which incorporation of transition metals such as Mn, Co and Al. NMC (Co with Ni and Mn) and NCA (Co with Ni and Al) are representative ones. Higher Ni content in Ni-contained cathodes indicates the enhanced specific capacity (Fig. 1-8). In general, the specific capacity of $LiNi_{1/3}Mn_{1/3}Co_{1/3}O_2$ (NMC111) exhibits about 160 mAh g^{-1}, and $LiNi_{0.8}Mn_{0.1}Co_{0.1}O_2$ (NMC811) can show the reversible capacity over 200 mAh g^{-1} with higher Ni ratio.

From the above things, higher Ni content has been investigated to increase the specific capacity, resulting in higher energy density. Additionally, this strategy can reduce the cost by minimizing the use of expensive Co element. However, the high content Ni contained cathode exhibits poor cyclability, thermal instability, and so on. (Fig. 1-9).[30] Various studies have been reported to overcome the problems with doping, surface coating, single crystal structuring and gradient element distribution in particles. In addition, these technologies have continued to develop and shown the performance close to the commercialization level.[31-33]

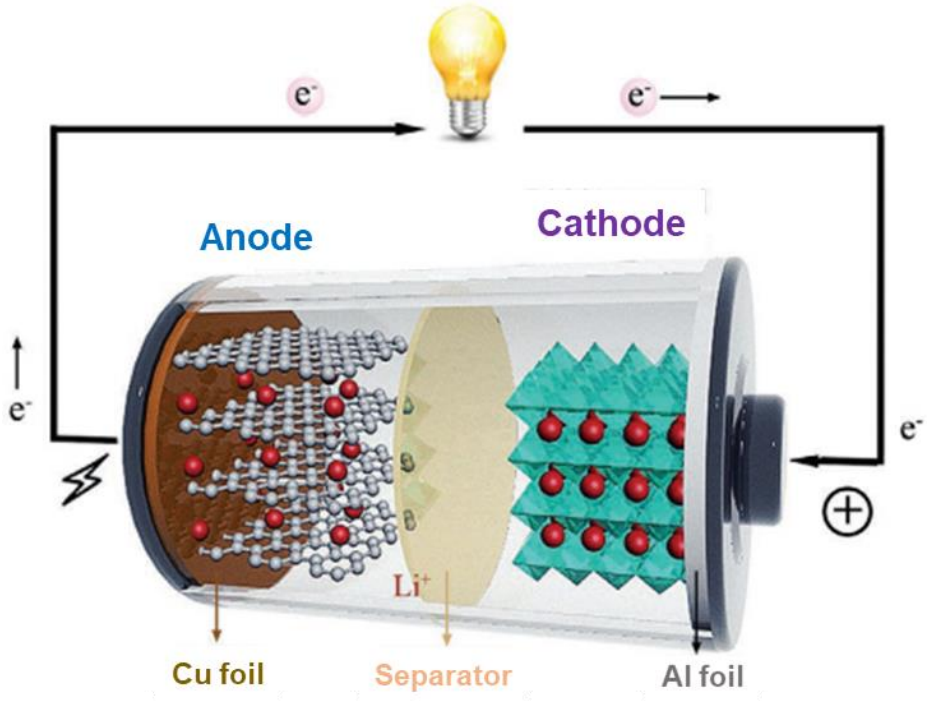

Figure 1-5. The structural image of lithium-ion batteries on the operating state.

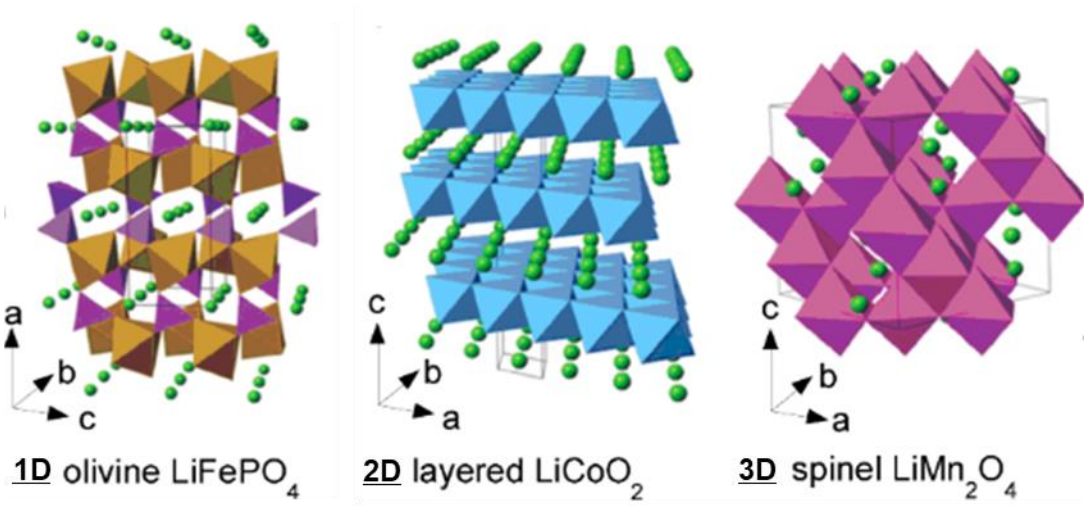

Figure 1-6. Crystal structures of different cathode materials; the olivine (1D), layered (2D), spinel (3D) structured cathode.

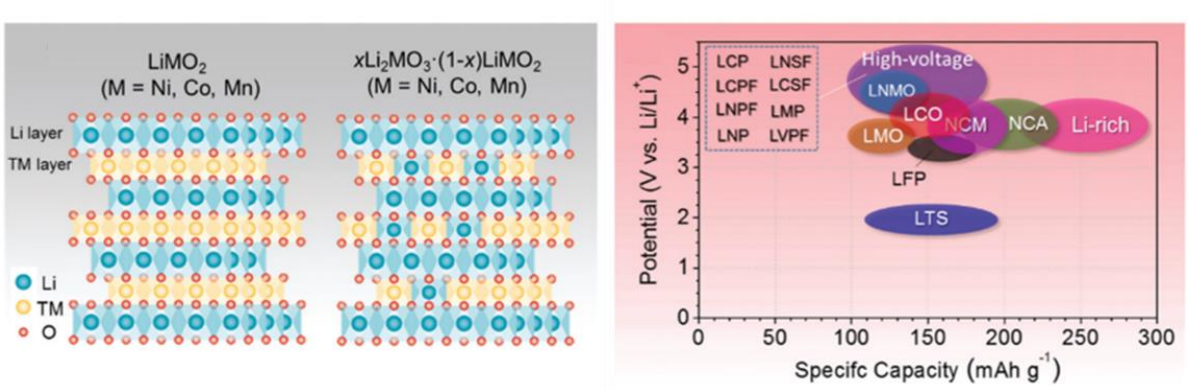

Figure 1-7. Crystal structure of LiMO2 and potential comparison of high voltage commercial cathode materials.

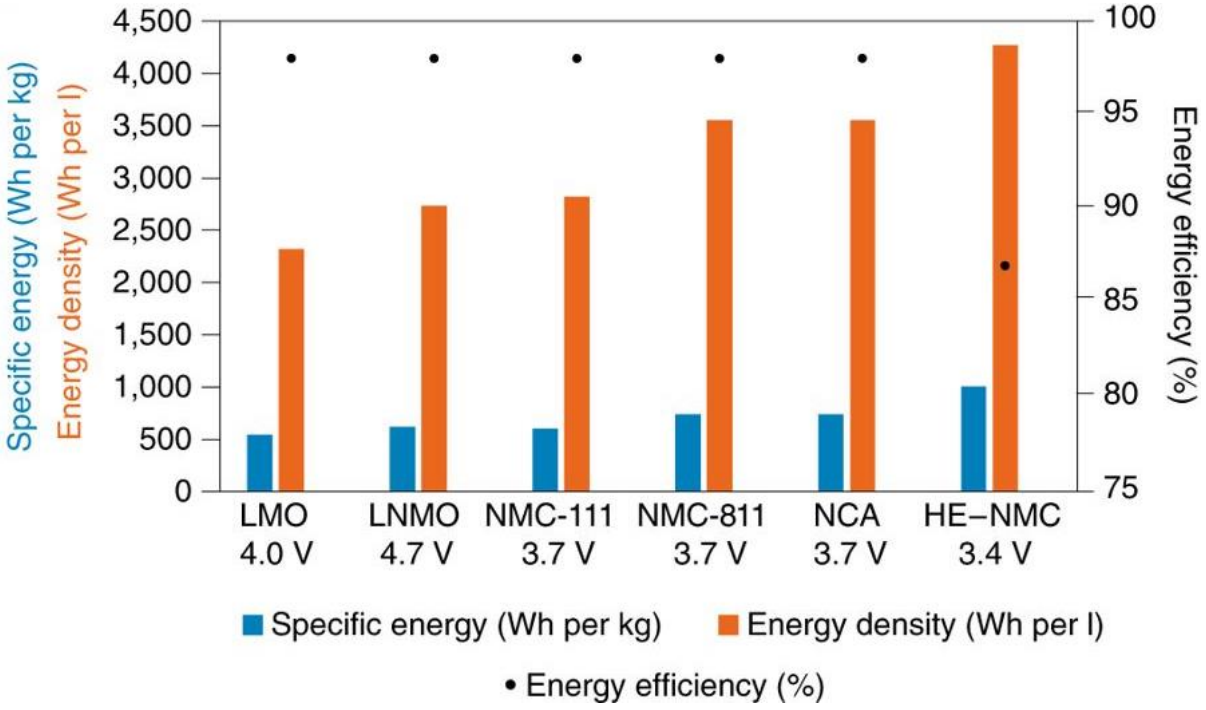

Figure 1-8. Energy density, specific energy and energy efficiency of various cathode materials in assumption of typical active material size.

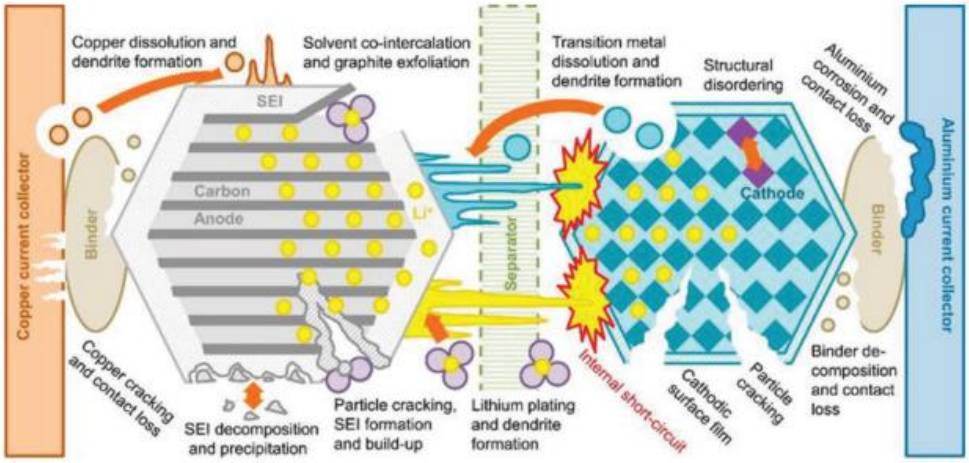

Figure 1-9. Degradation mechanisms of anode and cathode in Li-ion batteries.

Anode

As opposed to cathode, Li ions are reduced at anodes during the charging reaction. The Li ions and electrons are transported by different pathway of electrolyte and external circuit, respectively. They reunite at anodes ($xLi^+ + xe^- \rightarrow xLi$), which are the host materials to accommodate the reduced Li ions within the material structure. During the discharge process, the opposite reactions (oxidation of Li: $xLi \rightarrow xLi^+ + xe^-$) occur, resulting in the formation of Li ions and electrons.[34.35] Then, the oxidized provisions move to counterpart electrode (cathode). These corresponsive reactions simultaneously take place at each electrode. In this regard, there are various Li hosting mechanisms with intercalation, alloy and conversion reaction (Fig. 1-10).[36] For these types, various candidates have been investigated as anodes of LIBs. Graphite and $Li_4Ti_5O_{12}$ are typically recognized as the intercalation anodes, which accommodate the reduced Li ion within the interspace of hosts. These materials demonstrate the layered structure that Li could occupy the space. Another type of alloy reaction material is generally metal element such as Si, Sn and tin, which brings about covalent bond with Li ($M + xLi^+ + xe^- \rightarrow Li_xM$) during the charging process. Conversion type anodes generate structural changes ($M_xZ_y + 2yLi^+ + 2ye^- \rightarrow xM + yLi_2Z$), in which M and Z will be metallic (Fe, Ni, Mn and so on) and oxidative (O, F, N, P and so on) elements.

Key requisites of anode active materials are high specific capacities, high tap density, stable cyclability and low operating potential versus Li/Li^+. In this regard, carbonaceous materials are regarded as proper materials for feasible anodes of current commercial LIBs. In the early stage, Li metal was utilized, because this exhibits extremely high specific capacity and low working voltage. However, during the charge process, Li plating was unstable, inducing the dendritic Li growth. For this reason, graphite has been widely used as a major material. Even though the artificial graphite is expensive than natural graphite, this revealed better performances comparing to natural graphite, which is ascribed to the difference in surface area, packing density, purity and surface treatment. However, the carbonaceous anodes faced limitations in their theoretical specific capacity (graphite: < 360 mAh g^{-1}). Advanced technologies and expanded application fields such as electric vehicles require higher energy density storage.[37-39] On this account, Si and Li as next-generation anodes have attracted a lot of attentions and illuminated prospect of advanced LIBs (Fig. 1-11).[29] Recently, researchers have reported the developed results of Li metal anodes with the highest capacity and lowest potential.

Electrolyte

As a major component of LIBs, the electrolyte works as Li-ion carrier exchanging Li^+ between the cathode and anode through a separator. Key requirements of electrolyte are ionic conductivity, chemical stability with active materials, available temperature range and cost.[40] There are various types of

electrolyte such as liquid, polymer, gel polymer and solid-state electrolytes applied differently depending on the type of battery. Nonaqueous liquid electrolytes containing lithium salts and additives are commonly utilized in commercial LIBs. These salts and additives are dissolved in carbonate solvents such as ethylene carbonate (EC), propylene carbonate (PC), dimethyl carbonate (DMC) and diethyl carbonate (DEC). $LiPF_6$, $LiBF_4$, $LiClO_4$, and $LiAsF_6$ are general lithium containing salt. And functional additives with restricted amount are applied to stabilize the surface reaction with active materials. The concentration of lithium salts determines the characteristics of electrolyte such as the viscosity and ionic conductivity. The mixed composition can be easily modified corresponding to the demand characteristics of their applications.

Separator

The separator physically isolates the cathode and anode to prevent direct contact of them because the physical connection of both electrodes leads to electron transfer at the point with extremely fast transport. The short circuits could cause serious fires. That is, separator is an essential component in LIBs to assure the safety enhancement. The key factors to be obligated are thickness, low electric resistance, permeability, porosity, thermal stability wettability and mechanical properties. In this regard, the main materials to fabricate the separator are polymer and ceramic, which have insulating characteristics. In general, separator is mostly constructed with polymer body and thin ceramic coating due to the thickness, mass and cost.

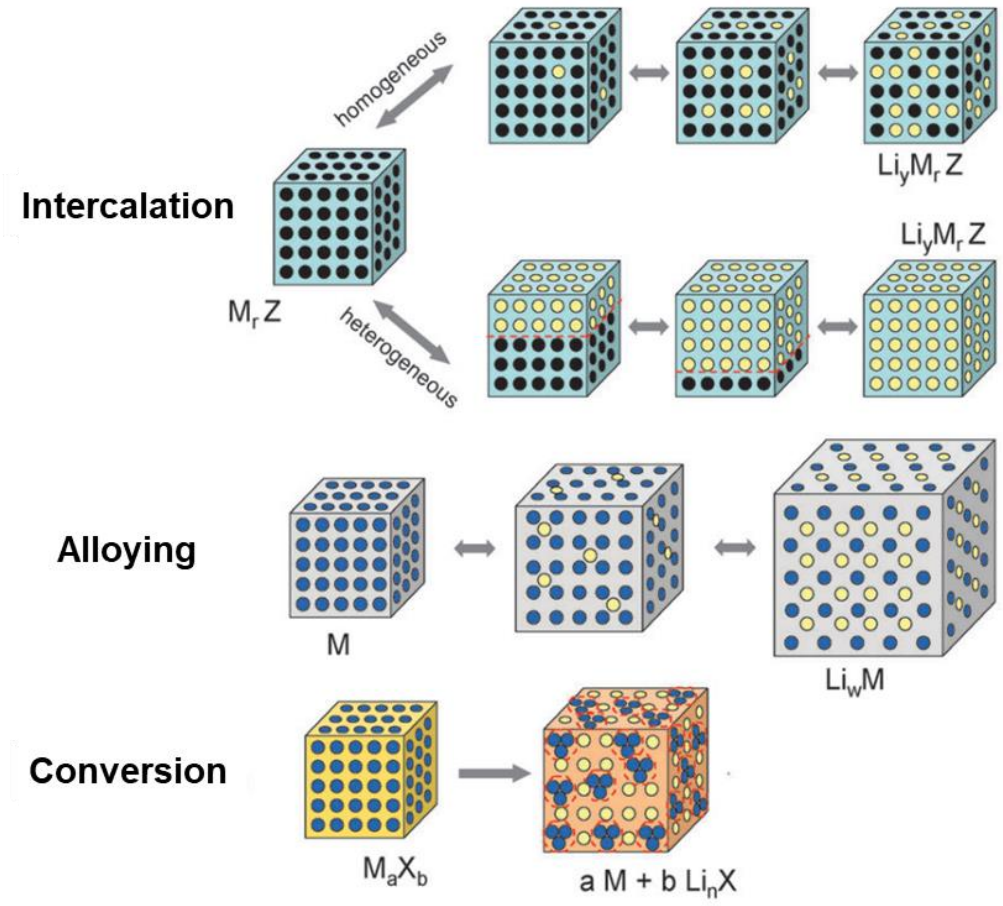

Figure 1-10. Scheme of the different reduction mechanisms categorized in anode materials; intercalation, alloy and conversion reaction.

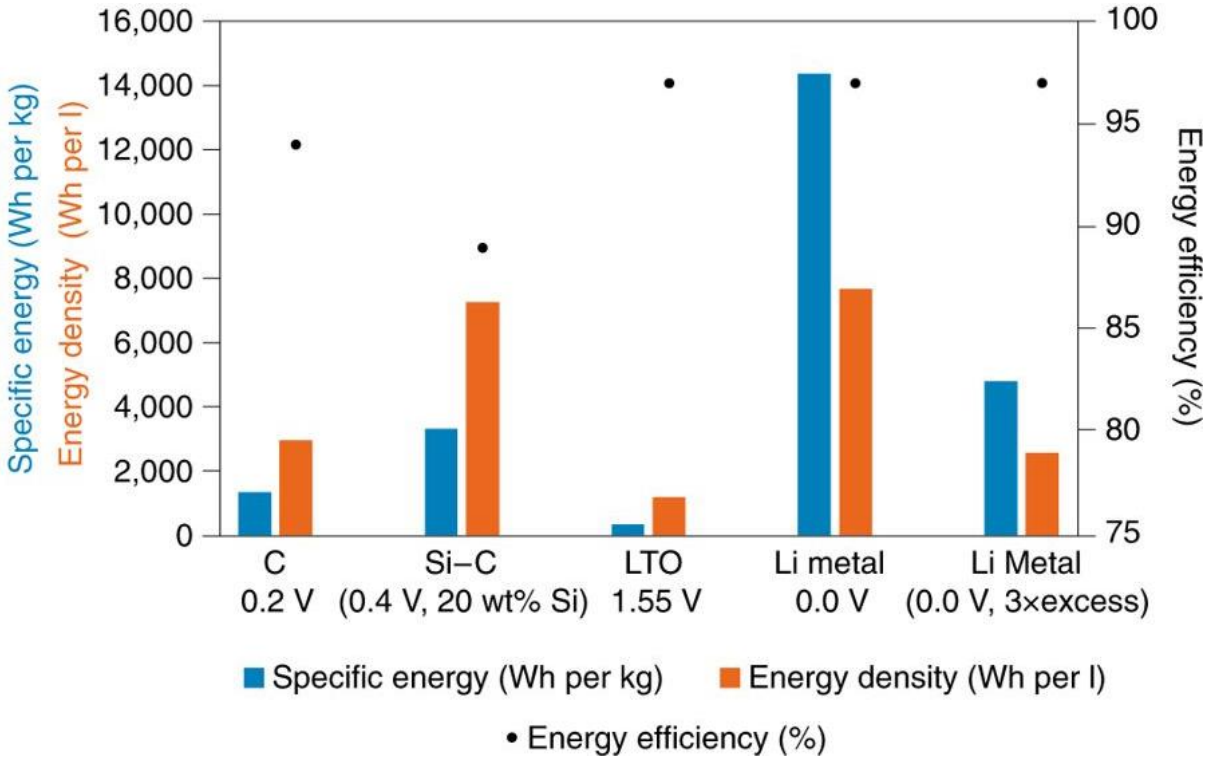

Figure 1-11. Energy density, specific energy and energy efficiency of various anode materials in assumption of conventional electrode composition.

1.3 Current limits and advanced anode materials

Current commercial anode: Graphite

By rapidly developing applications, higher energy density of Lithium-ion batteries is intensively demanded. In EV, which has recently been regarded as a representative battery application field, the maximum distance that can be driven by a single charge is considered as the main requirement. This will be directly affected by the performance of the battery, and in order to meet this, the development of high energy density LIB is indispensable. For practical improvement of LIB in the aspect of energy density, the fundamental parameters affecting energy density should be considered and satisfied with the required characteristics. In this regard, the operating voltage (V), specific capacity (mAh g^{-1}), mass loading (g cm^{-2}) and electrode density (g cm^{-3}), which directly affect the energy density value, must be contemplated.

Conventional graphite anode exhibits low working potential, extremely high initial Coulombic efficiency, good calendering suitability, and superior cyclability. At least to date, graphite has been an appropriate anode active material that generally meets these various requirements. Nevertheless, even if all other parameters are improved, the enhancement of energy density has been limited by the theoretical specific capacity (372 mAh g^{-1}). This low specific capacity of graphite significantly hinders its application in EV and energy storage systems (ESS). There is no choice but to adopt alternatives to overcome the upper limit in energy density (Fig 1-12).[41] Among them, Si has been attracted enormous attentions as the most promising candidate to alter graphite, due to its intensely higher theoretical capacity (3579 mAh g^{-1}).[42-44] Lithium metal anode has also been demonstrated as the eventual target anode due to its exceptionally high gravimetric and volumetric capacity (3,860 mAh g^{-1} or 2,061 mAh cm^{-3}) and the lowest potential (–3.04 V, SHE).[45,46] Higher capacity anodes such as Si and Li can adequately diminish the required thickness of electrodes, leading to increased energy density LIBs.

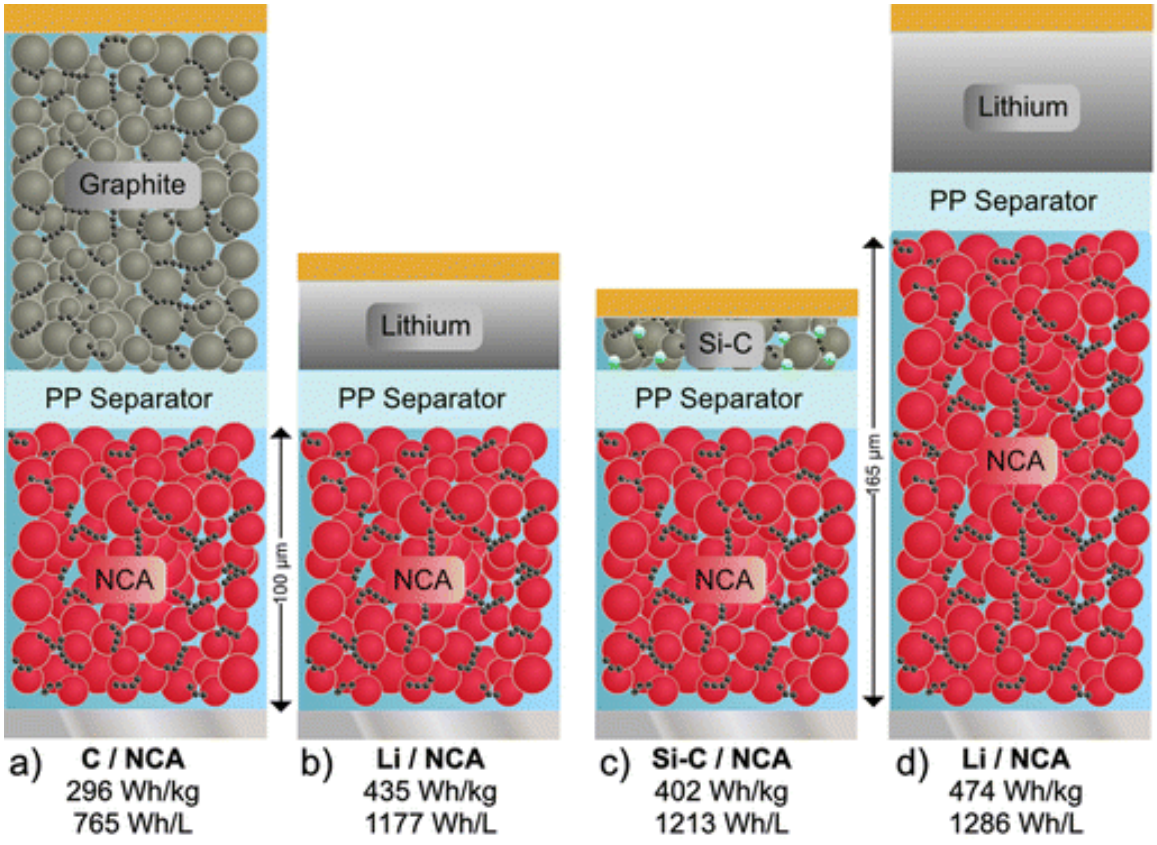

Figure 1-12. Schematic descriptions of various LIB anodes with NCA cathode according to the calculated specific energy and energy densities.

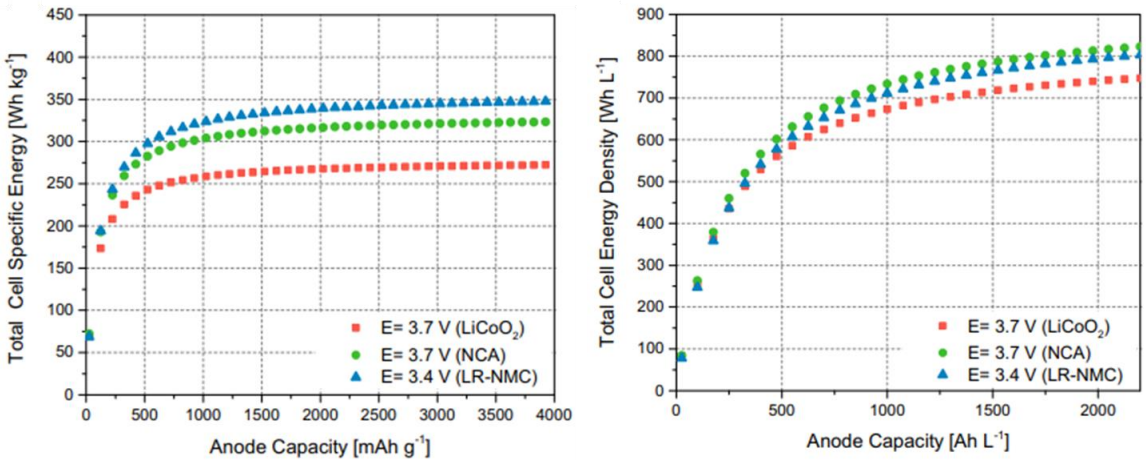

Figure 1-13. Total cell capacity and cell energy according to varying anode capacities with different cathode materials.[41]

Challenges for advanced anodes: Si

High gravimetric capacity active materials directly affecting the energy density of LIBs have attracted enormous attentions (Fig 1-13),[41] and Si has been regarded as one of the most promising candidates to alter conventional graphite due to the diverse advantages: low cost and abundance in Earth; high gravimetric and volumetric capacity comparing to commercial graphite anode; low operating potential.[47-50] Based on these merits, great number of researchers have intensively studied Si as anode active materials for more than 20 years. The performances have been significantly improved under limited conditions and restricted amount of Si (< 4wt %) applied anode materials are already used in certain applications. However, Si inherently involve severe volume change (expansion/contraction) as much as Li occupies during the lithiation/de-lithiation processes, which causes diverse and fateful problems in LIBs. The representative failure mechanisms are overviewed in Fig. 1-14;[51] electrical isolation by materials delamination, unstable solid electrolyte interphase (SEI) formation by newly exposed surface, particle pulverization. Because these critical problems bring about poor performance of LIBs, the Si applied anodes still has been hesitate in commercial batteries.

To address these fatal obstacles, comprehensive researches about nano-engineered strategy have been performed with nano sized materials (nanoparticle, wire, layer, tube etc.). And void containing materials (yolk shell, hollow structure, etc.), the surface coating method and inactive phase composition trails are also studied by worldwide researchers. (Fig. 1-15)[52] These strategies demonstrate the significantly developed performances in the aspect of limited conditions. For the practical application of Si anodes to LIBs, the key parameters should be satisfied with commercial electrode level. Especially, the reported publications commonly have deficiencies in low Coulombic efficiency (large irreversible capacity from huge specific surface area);[53] low electrode density (induced by particle size and tap density);[54] low areal capacity (lower energy density);[55] expensive and embarrassing production process (nano and void structure);[56] high electrical resistance (intrinsic property of Si). Nonetheless, most of results focused on high specific capacity without considering other major factors. Low mass loading, areal capacity, electrode density, and high additive (binder and conductive agent) composition have been frequently conjugated to the investigation of the battery performances. The inferred results by these conditions would be unreliable electrochemical performances for practical LIBs.

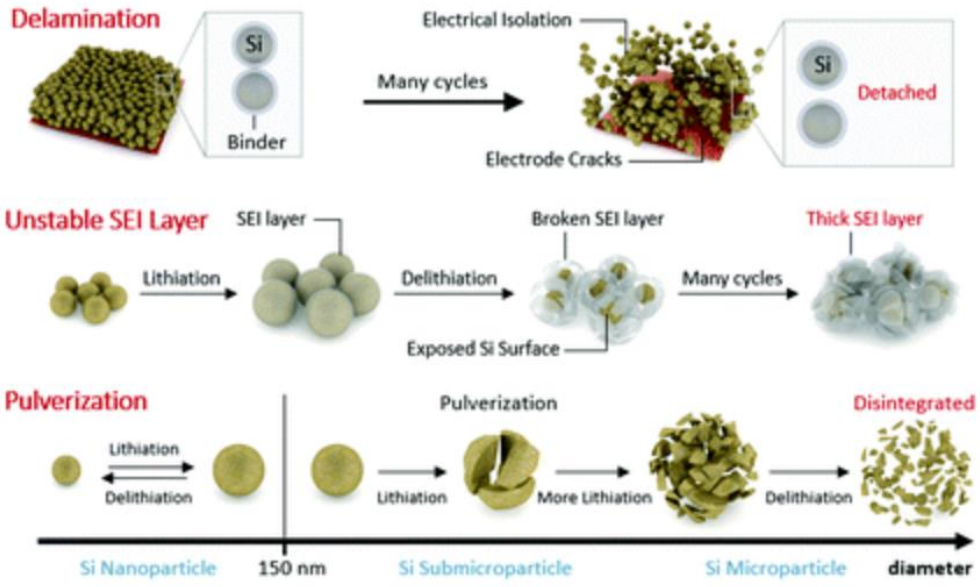

Figure 1-14. Overview of failure mechanisms of Si anodes by intrinsic volume expansion: delamination, unstable SEI layer, and pulverization.

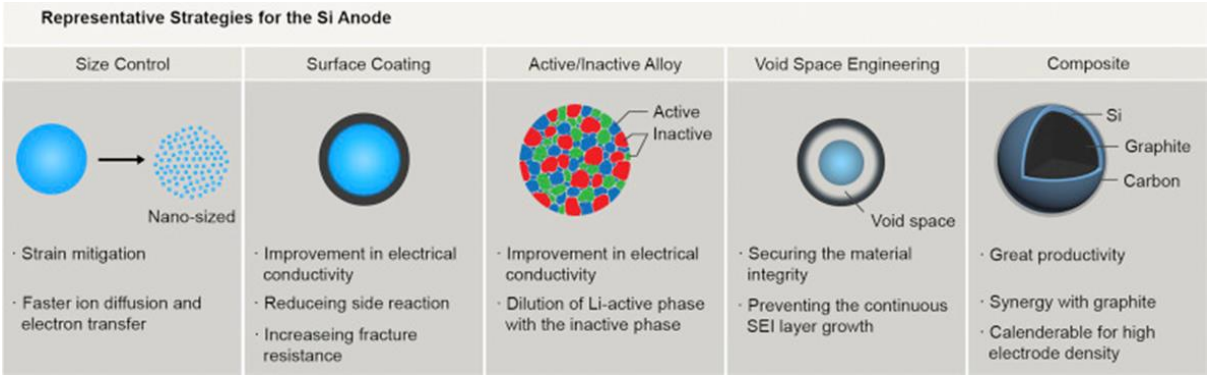

Figure 1-15. Representative strategies being frequently reported for the Si anode.

Challenges and progress for next generation anode: Li

Lithium metal has been regarded as the ultimate candidate due to its highest theoretical capacity and lowest operating voltage among the possible anode applicants.[57-59] By the reported study, a Li metal applied cells can release higher specific energy and energy density (Fig. 1-16). Furthermore, Li metal is crucial component for next-generation battery systems such as the Li-sulfur and Li-air batteries, which have almost theoretical value to access the energy density of gasoline applied devices (Fig. 1-17).[60]

Despite these formidable advantages and expectations, the Li metal anodes cause to be reluctant in terms of safety issue and cyclability. During the cell operation, Li ions are reduced and plated at anode part, which tend to form the dendrite on the electrode surface. The dendritic lithium growth is the well-known reason of internal short circuit. The internal short circuit can cause thermal runaway and severe explosion. Additionally, such continuously formed Li dendrites during the cycles generate several serious problems, resulting in fatal obstacles use Li metal anodes. 1) Dead Li formation from dendrites; the huge volume change during the plating/stripping process can give rise to electrical and physical isolation from the current collector. 2) Thick solid electrolyte interphase (SEI); The continuous side reaction with dendrites can consume large amount of electrolyte, causing thick SEI layer on electrode surface. It can interrupt the accessibility Li ions to current collectors, converting isolated dead Li. These effects influence severe decrease of Li sources, resulting in low cycling Coulombic efficiency. 3) SEI crack and accelerated side reactions; The dendritic Li growth can pierce the SEI layer, which expose fresh surface area of Li. Increased Li surface induce adverse reactions with electrolyte, which consume the Li sources and electrolyte irreversibly. The irreversible reaction is the main reason of poor cyclability of Li metal batteries. 4) Polarization; The dendritic Li metal generally has uneven morphology consisting of numerous tips and furrows. This ununiform electrode surface generates increased diffusion pathway and internal resistance. (Fig. 1-18) Dendritic Li brings about the decreased Li deposition density, ascribed to pore space within the deposited Li films, accelerating the volume change.

In summary, dendritic Li leads to severe problems such as fatal safety issue and poor cycle characteristics as Li ion batteries. Concomitantly, huge volume change and low Coulombic efficiency should be solved. To achieve these goals, suppression the dendritic Li growth is efficient method to approach the practical applications of Li anodes. Recently, researches related to the advanced Li anodes have been grown to resolve intrinsic and critical issues of Li metal anodes for practical battery application (Fig. 1-19).

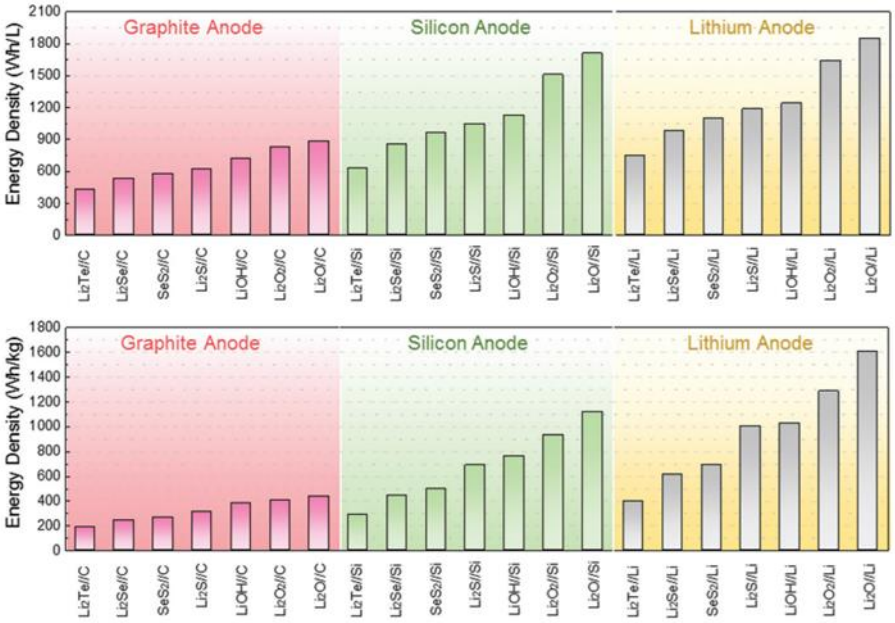

Figure 1-16. Volumetric and gravimetric energy densities of rechargeable batteries using graphite, Si, and Li metal anode.[28]

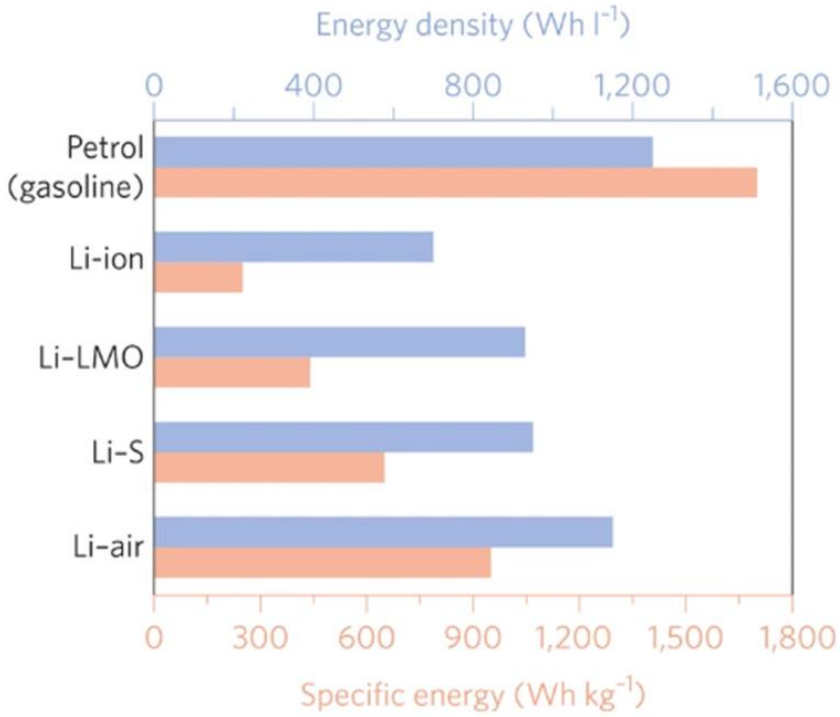

Figure 1-17. Practical specific energy and energy densities of various type of typical Li batteries

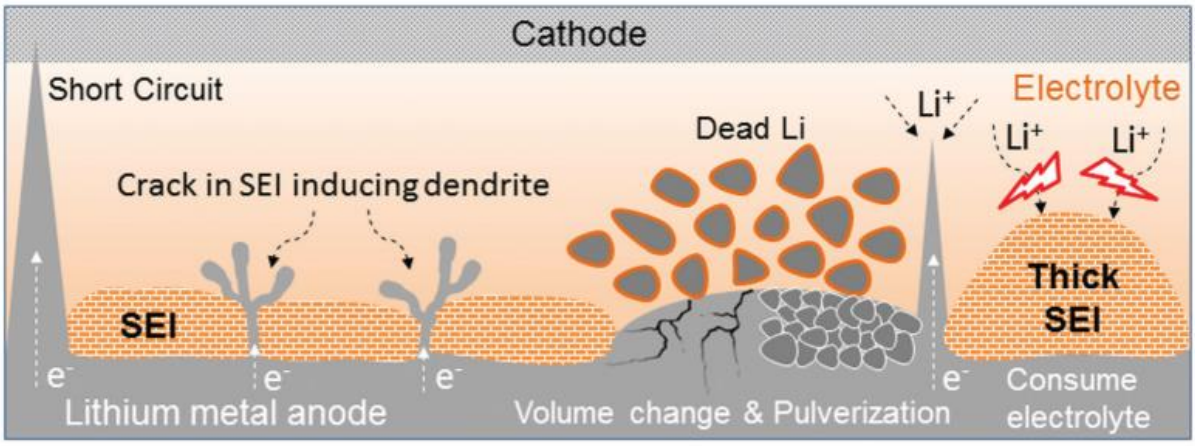

Figure 1-18. The schematic view of unfavorable interaction on the lithium metal anode.

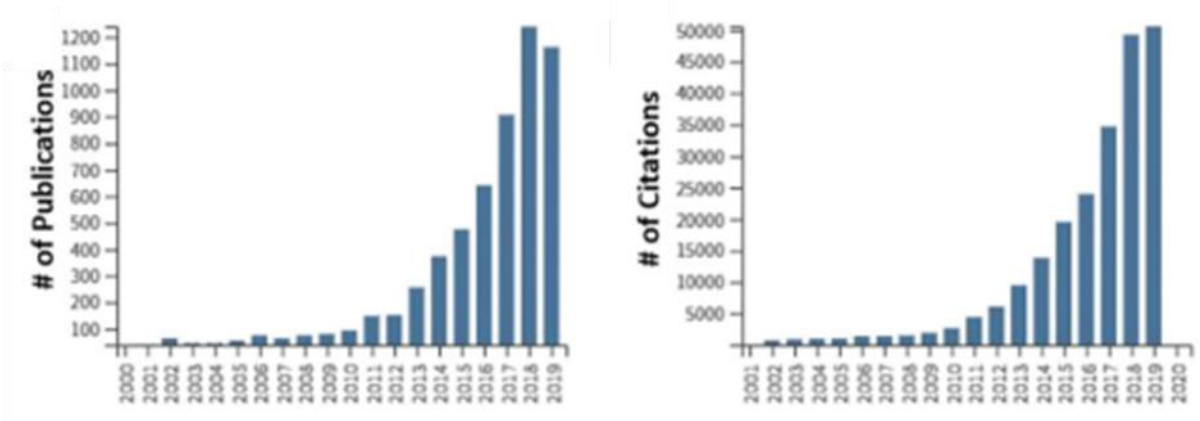

Figure 1-19. The number of publications and citations related to lithium metal batteries from 2000 to 2017.

1.4 Scope and organization of this dissertation

The objective of this dissertation is the feasible material design study of alloy type Si based anodes for high energy density lithium ion batteries and advanced lithiophilic lithium metal anodes for next-generation secondary batteries.

The chapters in this dissertation are categorized as follows:

Chapter 2 presents stress relief principle of micron-sized Si based anodes with large volume variation for practical high-energy lithium-ion batteries via the finite element method (FEM)

Chapter 3 presents the lithiated lithiophilic Li_xSi layered Li host materials for next-generation high-energy Li-metal batteries

Chapter 2

Stress Relief Principle of Micron-sized Anodes with Large Volume Variation for Practical High-Energy Lithium-Ion Batteries

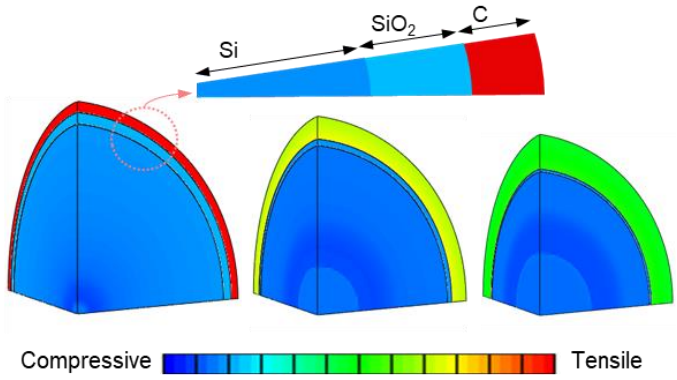

Practical applications of high gravimetric and volumetric capacity anodes for next-generation lithium-ion batteries (LIBs) have attracted unprecedented attentions, but still faced challenges by their severe volume changes, rendering low Coulombic efficiency and fast capacity fading. Nano and void-engineering strategies had been extensively applied to overcome the large volume fluctuations causing the continuous irreversible reactions upon cycling, but they showed intrinsic limit in fabrication of practical electrode condition. Achieving high electrode density is particularly paramount factor in terms of the commercial feasibility, which is mainly dominated by the true density and tapping density of active material. Herein, based on finite element method calculation, we introduce micron-sized double passivation layered Si/C design with restrictive lithiation state, which can withstand the induced stress from Li insertion upon repeated cycling. Such design takes advantage in structural integrity during long-term cycling even at high gravimetric capacity (1400 mAh g^{-1}). In 1 Ah pouch-type full-cell evaluation with high mass loading and electrode density (~3.75 mAh cm^{-2} and ~1.65 g cm^{-3}), it demonstrates superior cycle stability without rapid capacity drop during 800 cycles.

This chapter has been submitted.

Reproduced with permission from Y. Lee, T. Lee, J. Hong, J. Sung, N. Kim, Y. Son, J. Ma, S. Kim,* and J. Cho* Stress Relief Principle of Micron-sized Anodes with Large Volume Variation for Practical High-Energy Lithium-Ion Batteries. *Advanced Functional materials*

2.1 Introduction

The unprecedentedly expanded use of energy storage devices (portable devices and electric vehicles) has accentuated the requisition of improved energy density and long-life span lithium-ion batteries (LIBs) satisfying light weight, small volume and long-term use on a single charge[61-64]. For these reasons, alloying anodes with high capacity have attracted enormous attention for increasing the energy density of LIBs[65-68]. However, high capacity alloy type anodes inherently involve tremendous volume change as much as Li occupies during the lithiation/de-lithiation processes[69-71]. Even worse, it precipitates electrical contact loss due to the generation of irregular void spaces within the material during Li extraction, leading to Li trapping effects[72]. In order to address these severe imperfections, comprehensive researches about nano-engineered (nanoparticles, wires, layers, etc.)[73-75] and void containing materials[76-78], have intensively performed with phenomenal improvements due to their alleviated mechanical stress and volume change[79-81]. However, these strategies missing some essential factors determining the energy density of LIBs have reported only with good electrochemical evaluations, despite their significant vulnerability in industrial feasibility.

In this regard, the key parameters affecting the electrode density (i.e. particle size distribution, tap density, and volume ratio of active materials in electrode) and the mutual relationship to be mandatorily considered in designing the active materials with highly commercial opportunity are presented in Figure 2-1 and 2. Particle size is notably paramount consideration in electrode aspect. Because the electrode porosity is mainly determined by tap density of electrode materials, anode with low tapping density would cause high proportion of voids in the electrode resulting in thicker electrodes, longer electric pathway, and limit the electrochemical properties in LIBs. Moreover, the volume occupied by the active material in the electrode should also be considered. The utilization of excessive binder and conductive agent to improve mechanical stability and electrical conductivity should be suppressed. Materials with low tap density lead to increased particle volume to fulfill the equivalent areal capacity, increasing cell volume, which constrains feasibility in terms of volumetric energy density.

To address these issues lowering the electrode density, active material design with enlarged particle size, densified morphology, high tap density, and low specific surface area should be contemplated. As in Figure 2-1, enlarged particle size can reduce and enhance the number and tap density of particles, respectively. Furthermore, the densified particles can essentially mediate reduced size and number of particles in the same materials mass, which has advantages of lowering the specific surface area and facilitating higher electrode density, resulting in improved energy density. In case of the specific surface area, it could be highly increased in nano or void containing materials since the specific surface area is inversely proportional to the particle size[82]. Such highly increased surface area of the active material

could become reactive site with the electrolyte, formation quantitative solid electrolyte interphase (SEI). Therefore, the study of non-porous and high tapping density micron-sized composite with low specific surface area would be requisite for its practical feasibility in advanced LIBs.

As in the previous nano-sized material study revealing the critical factors which sustain the morphological integrity, constructive studies for stabilizing the micron-sized particle during long-term cycling should be investigated in terms of management for stress evolution. Numerous successful studies about Si-based micro-particles have been published with inactive matrix to accommodate volume expansion[83-87]. But qualitative results, realizing whole practical cell components (electrode composition, mass loading, electrode density, working potential, cost, etc.) and according properties in full-cell are rare and elusive. Levelheaded study about high capacity anodes satisfying the whole practical parameters is required for true performance advancement in LIBs.

Herein, we constructed the designing principle of Si-based anodes with no voids via the finite element method (FEM) about the capacity range from 760 to 2100 mAh g^{-1}, while relieving the induced stress with protective carbon. The tensile and compressive stress regulate the mechanical stability and proportion of activated Si, respectively. Consequently, eventual intentions for effective material behaviors can be elucidated in the aspect of protective materials content and concluding capacity. The proposed design of micron-sized double passivation Si/C composite was realized in highly densified structure via simple and scalable synthetic process of vigorous mixing with solvated C precursor. Micro-particles are experimentally substantiated with rational particle size distribution (mean diameter of 10.4 μm), tapping density (~1.1 g cm^{-3}) and specific surface area (1.56 cm^2 g^{-1}). Pouch type full-cell investigation about the typical samples was performed with industrial standards. Mechanically unstable Si/C composite with higher capacity of 1781 mAh g^{-1} resulted in lower capacity retention and cycling efficiency. In contrast, the rationally designed Si/C composite of 1402 mAh g^{-1} showed superior cycling retention even over 800 cycles in the 1 Ah full-cells with industrial electrode specifications. This study would provide the guidelines of feasible active material design to be considered for high energy density commercial battery and report the logical comprehensions of Si degradation in full-cell configuration.

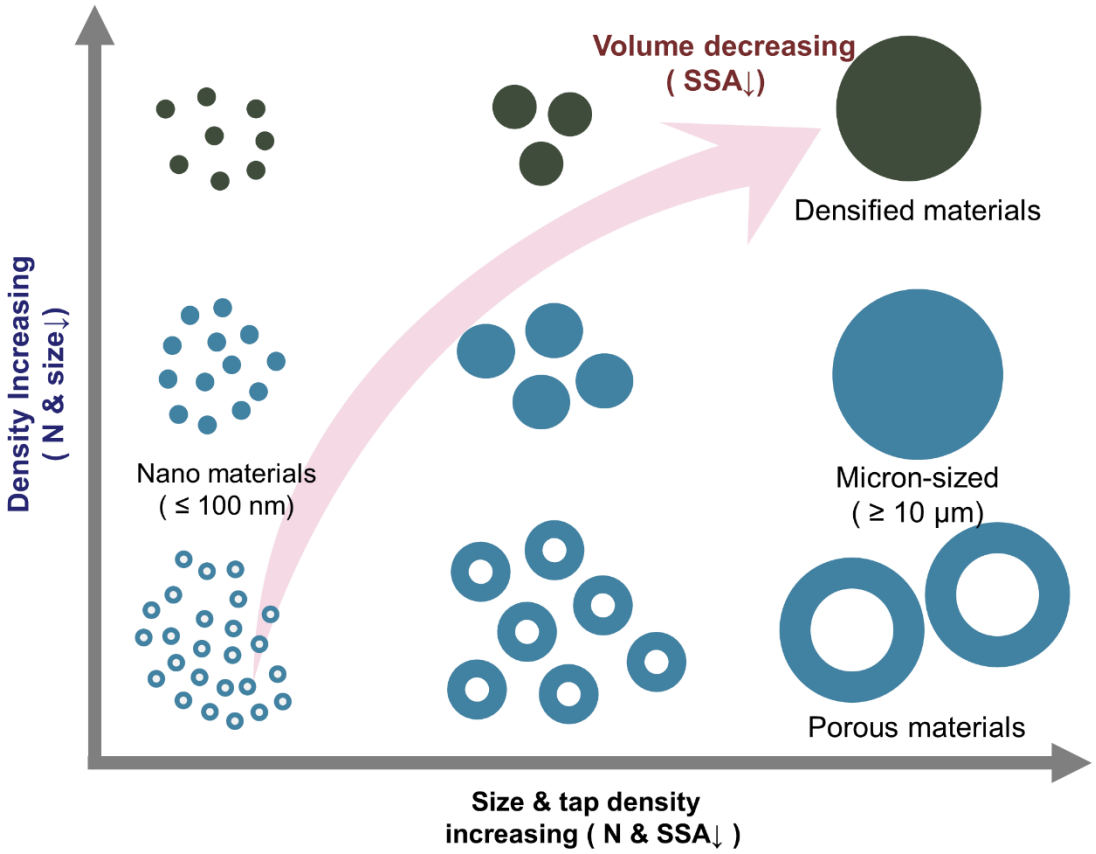

Figure 2-1. Critical considerations and correlation of designing factors for high capacity and energy density active materials.

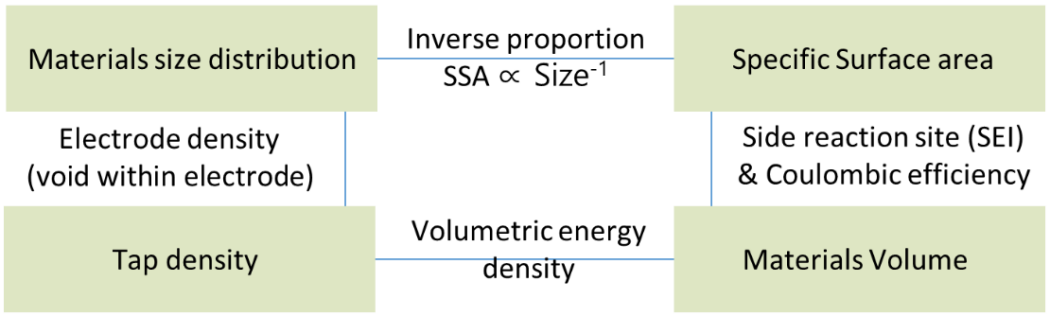

Figure 2-2. Correlation of each factors related to high capacity and energy density active materials.

2.2 Experimental detail

Synthesis of SCM. Initially, Si microparticles (99.995%, 30 μm) was mechanically crushed to the limit size (< 150 nm) of Si nano-seed with SiO_x passivation layer, which was controlled with DI-water content of applied solvent (MiniCer, NETZSCH). To prepare intercalated and outmost carbon passivated micron-scale secondary particles, pitch (POSCO Chemtech) were well dissolved in tetrahydrofuran (THF, Junsei). Si/SiO_x nano seeds were mixed in pitch solution and stirred vigorously in a planetary centrifugal mixer (Thinky) as in the scheme of figure 2-3, which evaporates the solvent then assembles double passivation layered Si/C micro-particles (SCM). Pitch content was designed according to the gravimetric capacity of anode materials. The assembled SCM was annealed in box furnace under nitrogen atmosphere with the batch of 300 g. The heat-treating temperature was established at 950 °C for 5 hours with ramping rate of 5 °C min^{-1}.

Materials characterization. Morphological and cross-sectional investigation of the samples was performed using scanning electron microscopy (SEM, Verios 460, FEI) with energy-dispersive spectroscopy (EDS, XFlash 6130, Bruker) and the high-resolution transmission electron microscopy (HR-TEM, JEM-2100F, JEOL) with EDS(Aztec, Oxford). To prepare the particles and electrodes for cross-sectional view, dual-beam focused ion beam (FIB, NX2000, Hitachi) and ion milling system (IM40000, Hitachi) were utilized. The chemical bonding of the particles was examined using X-ray photoelectron spectroscopy (XPS, Scientific K-Alpha system, Thermo Scientific) with Al Kα radiation. To analyze the particle size distribution, the samples were distributed in ethanol then measured by laser diffraction particle size analyzer (Microtrac S3500, Microtrac). The specific surface area and pore volume distribution were examined with the nitrogen adsorption-desorption analyzer (TriStar II, Micromeritics). T.A.P density analyzer (Micromeritics Instrument Corporation) was utilized to measure the tap density of final products. To investigate the crystallininty and structure, X-ray diffractometer (XRD, D/MAZX 2500V/PC, Rigaku) analysis was conducted (D/MAZX 2500V/PC, Rigaku). To observe the morphological change of cycled electrodes, the electrochemically characterized cells were disassembled in Ar-filled glove box, then rinsed with dimethyl carbonate (DMC).

Electrochemical characterization. The electrodes fabrication was conducted by homogeneously mixed slurry casting on Cu foil, composing of active material (SCM, u-SCM and graphite blending), conductive agent (carbon black, Super P, Imerys), carboxymethyl cellulose (CMC, Nippon paper) and styrene butadiene rubber (SBR, Zeon). The mass ratios of solely used Si/C and graphite belended electrodes were 80:10:5:5 and 96:1:1.5:1.5, respectively. The areal capacity of solely used and blended electrodes was adjusted to 3.6~3.75 mAh cm^{-2} (loading level with 2.0~2.6 and 5.5 mg cm^{-2}), followed drying process at 80 °C for 1 h. Graphite blending electrode was calendered for electrode density over

1.6 g cm^{-3} using press machine, then, dried at 120 °C for 8 h under vacuum state. CR2032 type half-cells were assembled in the Ar-filled glove box with separator (microporous polyethylene, 15 μm, Celgard) and electrolyte (1.3M $LiPF_6$ in mixture of ethylene carbonate/diethyl carbonate (3/7 by volume) with 10% fluoroethylene carbonate, Enchem). The electrochemical characterizations of half-cells were conducted in the voltage window from 0.005 to 1.5 V at 0.1 C (0.01 C cut-off, constant-voltage) for the first formation, then 0.005 to 1.0 V at 0.5 C with equal constant-voltage for the rest of the cycles, which was investigated with battery cycler (TOSCAT-3100, TOYO SYSTEM) at room temperature. The full-cell test was achieved with mono-electrode and stacked 1Ah pouch-type cells, composed of lithium cobalt oxide ($LiCoO_2$, LCO) cathode and graphite blended Si/C anode, which were assembled in humidity controlled dry room. Cathode was fabricated with LCO powder, conductive agent (Super P) and polyvinylidene fluoride (PVDF) binder at a mass ratio of 94:3:3. The areal capacity and electrode density of cathode are 3.3 mAh cm^{-2} with the loading level of 21 mg cm^{-2} and 3.6 g cm^{-3}, respectively. N/P ratio (negative and positive electrode capacity) of the designed full-cell was achieved in 1.1 based on the areal capacity. The detailed electrode and cell design are described in Supplementary table 1. The electrolyte and separator for pouch-type full-cell were same with that used for half-cell fabrication. The electrochemical characterizations of full-cells were investigated in an operating voltage window from 2.5 to 4.2 V at 0.2 C for the 2 cycles and 2.7 to 4.2 V at 0.5 C /1 C (charge and discharge) for the rest of the cycles using a battery cycler (WBCS3000, WonATech) at 25 °C and 50 °C. The electrode swelling of 1 Ah pouch-type full-cells during cycles at 25 °C and 50 °C was estimated using an in-situ dilatometry system with digimatic indicator (Mitutoyo), ignoring the cathode swelling.

Numerical Simulations. We implemented finite element simulation for stress evolution and the corresponding mechanical stability of candidate structures using commercial software ABAQUS/Standard 6.14 (Dassault System). Thermal-mechanical coupled model, which is equivalent to the Li-diffusion model, was conducted to demonstrate the two-phase lithiation model[88] for double passivation layered Si/SiO_2/C micro-particles. Linear elastic material properties of silicon-based material were adopted in simulations with concentration-dependent mechanical properties such as elastic modulus and diffusivity, which had been measured by experiments[89-92]. Each particle was dimensioned from cross-sectional TEM images of Si, SiO_2 and carbon layer and following ratio with the three-dimensional quarter model. We evaluate the diffusion-induced deformation by computing hoop stress and volume expansion ratio.

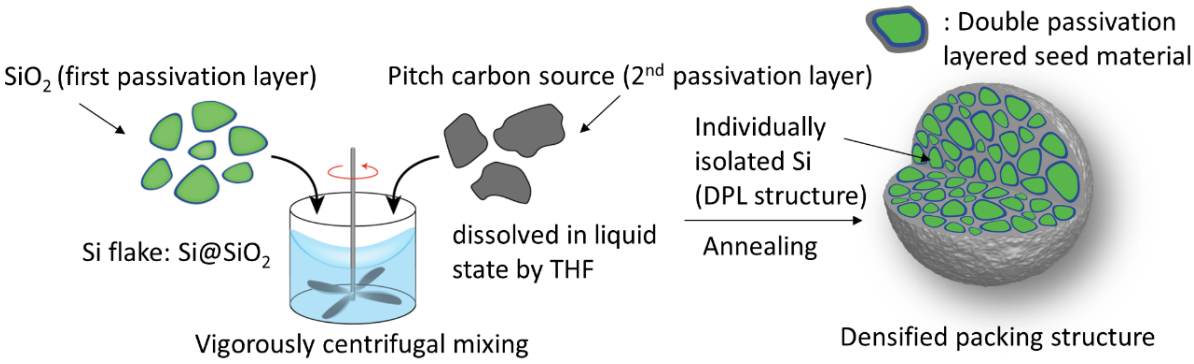

Figure 2-3. Schematic illustration of synthetic procedures of Si@SiO_2@C micro-particles

a

Volume ratio	#1	#2	#3	#4	#5	#6	#7
Si	1	1	1	1	1	1	1
SiO_2	0.375	0.375	0.375	0.375	0.375	0.375	0.375
C	0.05	0.268	0.365	0.67	0.765	1.34	2.01

b

Mass ratio	#1	#2	#3	#4	#5	#6	#7
Si	1	1	1	1	1	1	1
SiO_2	0.396	0.396	0.396	0.396	0.396	0.396	0.396
C	0.073	0.39	0.53	0.977	1.114	1.952	2.949

Table 2-1 (a) Volumetric ratio, (b) mass ratio of double passivated Si@SiO_2@C seed.

2.3 Results and discussion

Numerical Simulations of Stress evolution by lithiation. Although there have been numerous successful Si/C composite designs accommodating volume expansion, quantitative studies on the composite design principle are rare and elusive with rationally balanced Si and C contents. Therefore, this study suggests a practical design principle providing optimal amount of protective matrix with stabilized stress. Diffusion induced stress and corresponding volumetric changes based on finite element analysis are conducted from the structural model, in which SiO_2 and C have double passivated the spherical Si (fixed diameter of 100 nm) with a fixed thickness of SiO_2 (10 nm) and various C content according to each component ratio as shown in the Supplementary Table.1[93]. Hence, we provide rational understanding of $Si/SiO_2/C$ materials and exploit these results in experimental verification for the implementation of practically feasible Si-based anode materials. The volume ratio of C was modified, and the corresponding C thickness variation concerning the Si radius was exhibited in figure 2-4(a). When assuming the structure is not damaged, i.e., under the elastic assumption, figure 2-4(b) exhibits typical three results of inside stress distribution about rational (*4), deficient (*2) and excessive (*6) C content at fully lithiated state. At full lithiation state, A very thin C layer (*2) will result in 2100 mAh g^{-1} leading to extremely strong tensile hoop stress at surface C layer. Maintaining the initial structure will be challenging due to high volume change, which can cause material fracture, resulting in fast capacity decay. In contrast, the thick C layer is ascribed to low tensile stress at full lithiation state with low volumetric and gravimetric charging (* 6, 760 mAh g^{-1}), being verified in relatively large inactive Si volume at core region.

Figure 2-4(c) shows the diffusion induced tensile stress on outer-most C layer at fully Li insertion state and theoretical gravimetric capacity. The diffusion induced tensile stress on surface C layer demonstrates drastic decrease of stress value from 104.4(*1) to 37.5(*4) GPa that enters into elastic limit by stress relaxation with slight increment of C content[94]. The amount of lithiation per volume and corresponding volume expansion were presented in figure 2-4(d). Diffusion induced surface stresses exceeding elastic stress limit were cut off by the range of the stable mechanical property (40 GPa, red line in figure 2-4(c)). With these assumed conditions, charge/discharge behaviors would be stably retained without any fracture of materials. The insufficient mechanical enhancement of surface layer by thinner surface C layer is ascribed to rapid volume expansion even with a small amount of Li (Figure 2-4 (b) and (d)), then reach to elastic limit of surface layer easily just with relatively low lithiation state. In case of *1 model, only limited Li compared to the theoretical capacity can be used for stable behavior as in figure 2-4 (c) and (d), meanwhile the calculated stress value at the full lithiation state far exceeds the acceptable stress limit. Volume fraction of not lithiated Si by the compressive force is considered to derive actual capacity comparing to the theoretical value. Namely, the mechanical stress generated in the material during Li insertion suggests the controlled Li insertion per unit mass of composite. The

strong mechanical constraint by enhanced C content improves Li insertion feasibility with mechanically stable state. Si was noticed only restricted utilization under excess C layer (model *7, Figure 2-5)[95], which means excessive buffer matrix could restrict Li insertion and diffusion within Si, consequently leads developing inactive Si[74, 96]. The model (*4) set to rational C content was found to be 12.7 times lithiation availability compared to the thinner C model (*1). In contrast, with higher content of C than model (*4), compressive limit works instead of tensile limit. Our model of rational C containing model (*4) provides cross point value for two cut off condition, which enables effective Si utilization (Figure 2-5) and stabilized structural properties even at full lithiation. By these results, we can suggest the mechanically stabilized sustainable structure considering the stress limit applied at outmost graphitic C layer.

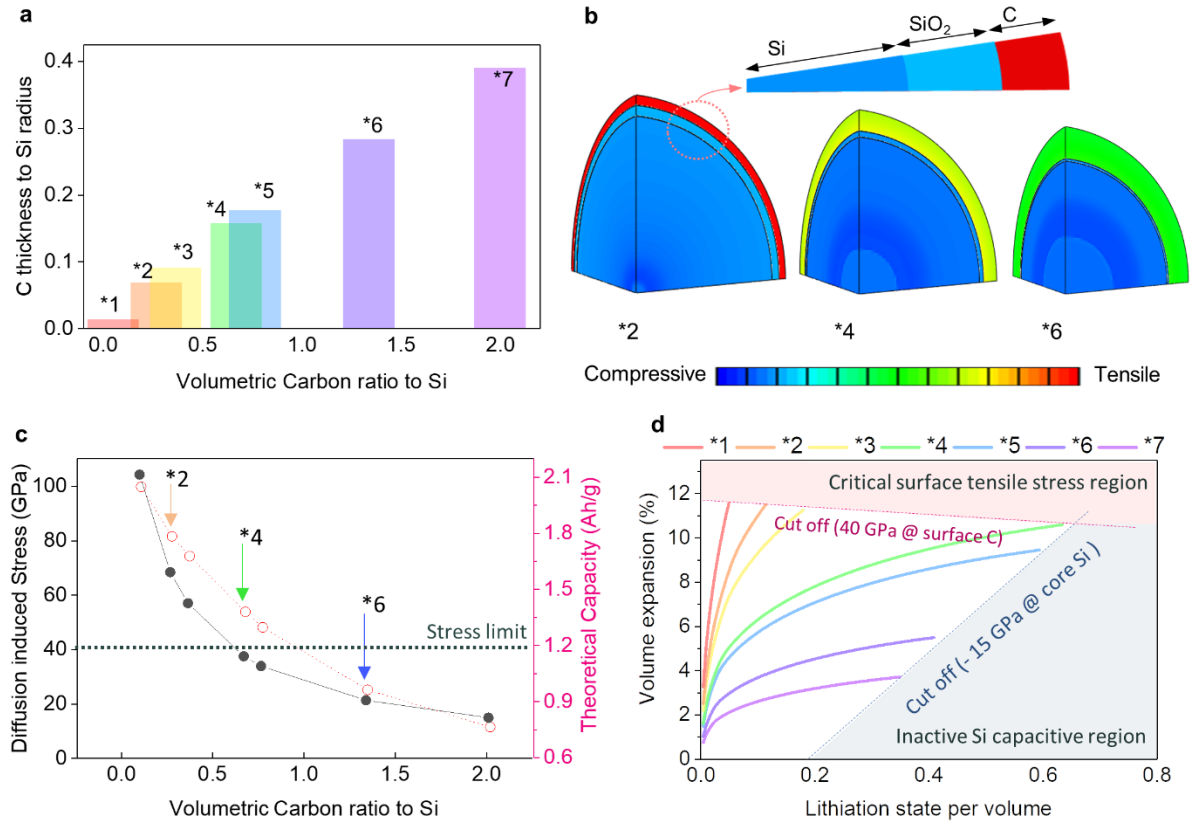

Figure 2-4 FEM calculation (a) Outer carbon thickness considering designed materials volume composition, (b) scheme of cross-sectional tensile and compressive stress distribution at full lithiation state, (c) diffusion-induced tensile stress at surface and corresponding theoretical capacity at full lithiation state, (d) volume expansion ratio according to lithiation state per volume, restrained with tensile and compressive stress.

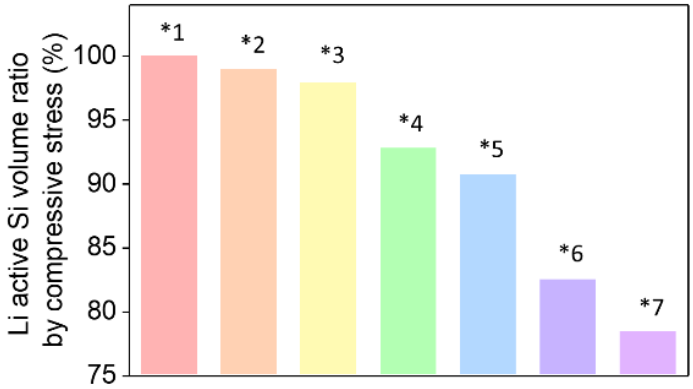

Figure 2-5 FEM calculation. Li insertion active volume ratio based on the *1 model restrained by compressive stress, according to designed models**.**

Materials fabrication and characterization. To substantiate the FEM calculation result regarding the sustainable stress limit, we design double passivation structured Si/C for high density composite micron-sized particles. In this study, we introduced composite material with SiO_2 coated nano-Si and interlayered elastic C for micron-sized particles to achieve high performance anodes, featured with low cost. The designed and synthesized materials achieve the alleviated stress and volume change, resulting in stable reversible capacity. Constructive structure was synthesized by liquid phase method. Pitch precursor dissolved in tetrahydrofuran (THF) is centrifugally mixed with SiO_2 passivated nano-Si in vigorous aqueous state, in which nano-Si can be homogeneously dispersed in C emulsion. Finally, the double passivation layered hierarchical structured composite materials are produced as in Figure 2-3. The centrifugal mixing method used in the synthesis process reduces the internal voids, enabling good packing property and high tap density, in which the nano-Si seed was homogeneously distributed and isolated by the interlayered C matrix. Then, carbonization materializes during calcination, which is beneficial to produce denser and harder particles by shrinkage step of C precursor. Moreover, the intermediate C structure also shows the multiple functions of elastic behavior of micron-sized particles and internal electrical network in the particles.

Figure 2-6(a) shows scanning electron microscopy (SEM) images of Si particles, while the corresponding transmission electron microscopy (TEM) image (Figure 2-6(b)) reveals that the surface of nano-Si was enclosed by amorphous SiO_2 layer, which was recognized to be 10 nm thick on average. The thickness of the SiO_2 layer could be adjusted by the oxidizing solvent (Di-water) content (Figure 2-7). Si particles were manufactured on the average diameter and thickness within 130 nm and 50 nm (Figure 2-8 and 9) by the mechanically downsizing process, and the crystalline Si grains smaller than 10 nm were embedded irregularly within amorphous Si matrix. X-ray diffraction (XRD, Figure 2-10) and electron energy loss spectroscopy (EELS) line scan (Supplementary figure S5) supports the results and elucidates the crystallites and microstructure of nano-Si. The average crystallite size by the diffraction peak using the Sherrer equation is completely consistent with TEM result[97].

The Si/C micro-particles were assembled with a mean diameter of 10.4 μm (Figure 2-11), as shown in figure 2-12(a), which confirms spherical morphology and smoothly formed surface by C encapsulation. The densely compacted composite materials with increased particle size are ascribed to the improvement of tap density (1.0 - 1.1 g cm^{-3}, Figure 2-13) and specific surface area (1.56 cm^2 g^{-1}, Figure 2-14), which were significantly improved values than that of the Si seed particles and therefore favored in improved electrodes and energy density. Cross-sectional observation and TEM energy-dispersive X-ray spectroscopy (TEM-EDS) analysis (Figure 2-15) demonstrates the dispersed and wrapped structure of nano-Si by C without exposed surface, preventing the direct contact of Si to electrolyte (Figure 2-16). The intermediate C layer not only provides electric pathway, buffers volume

change, binds the Si without fracture, but also controls Li insertion by compressive force (Figure 2-4 (c)), advancing the battery performances. The outermost C layer of micro-particles can also effectively stabilize SEI formation on the particle surface[98].

To fundamentally explore the characteristics of elements and chemical bonding before and after the C composite, we carried out the X-ray photoelectron spectroscopy (XPS) about the primary Si(@SiO_2) and assembled microparticles (Si@SiO_2@C). Deconvolution of the Si 2p spectra clearly showed relatively different signal of Si bonding (Si-Si, Si-O and Si-C). Various oxidized substances are confirmed by artificially produced SiO_2 passivation layer on the surface of the Si particles, but the peak intensity of Si-Si significantly decreased after the Si/C composite materials fabrication (Figure 2-16). The results indicate constructions of protective coating layer with suitable coverage to prevent the exposure and deterioration of Si. It can thus be concluded that the double passivation structure of composite materials was successfully fabricated as we intended.

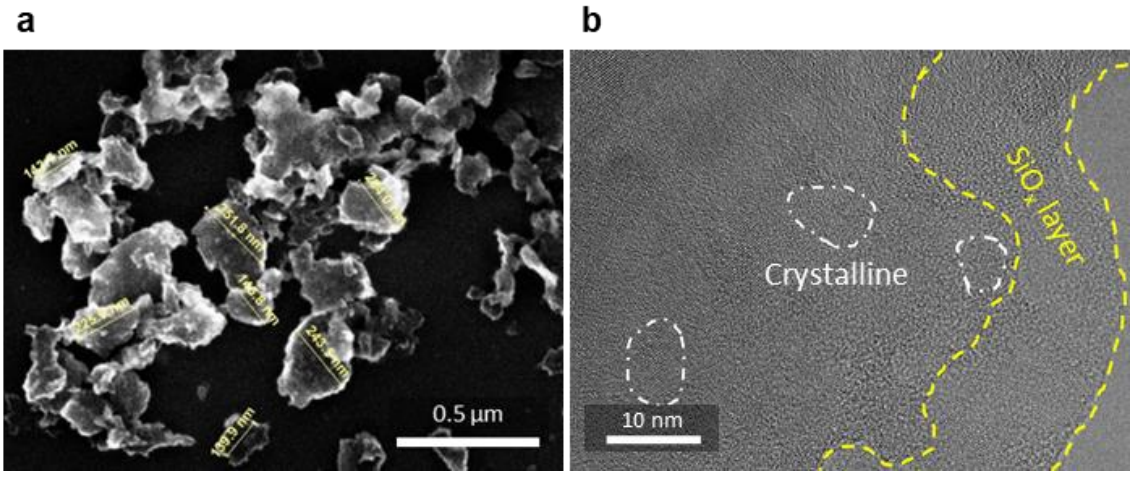

Figure 2-6 (a) SEM and (b) TEM characterization of Si nano-particles passivated with SiO_2 nano-layer

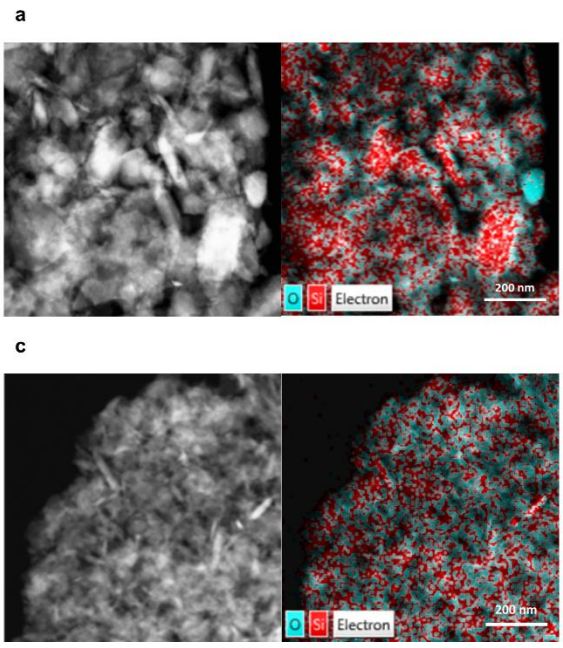

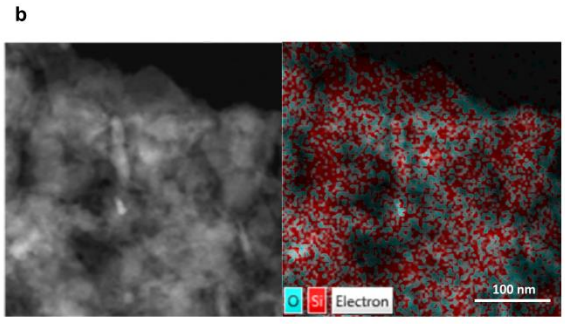

d

wt%	a	b	c
Si	91.8	86.7	79.3
O	8.2	13.3	20.7

Figure 2-7 STEM images of $Si@SiO_2$ with EDS mapping for Si and O elements, respectively. (a) less, (b) rational and (c) high content SiO_2 passivation layer applied $Si@SiO_2$. (d) Elemental ratio by EDS mapping.

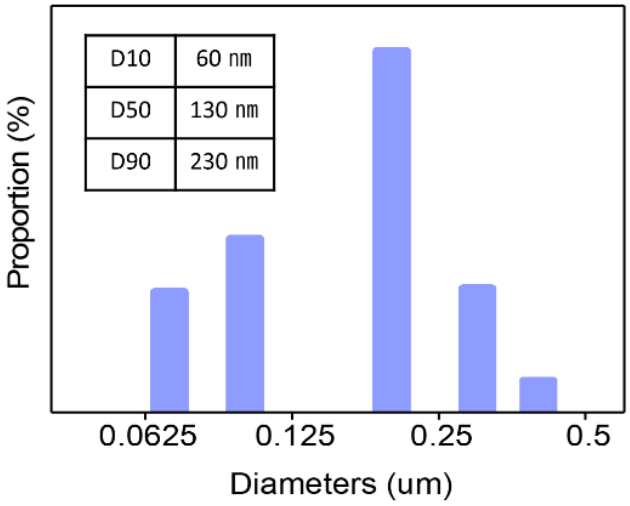

Figure 2-8 PSD (particle size distribution) of Si@SiO_2.

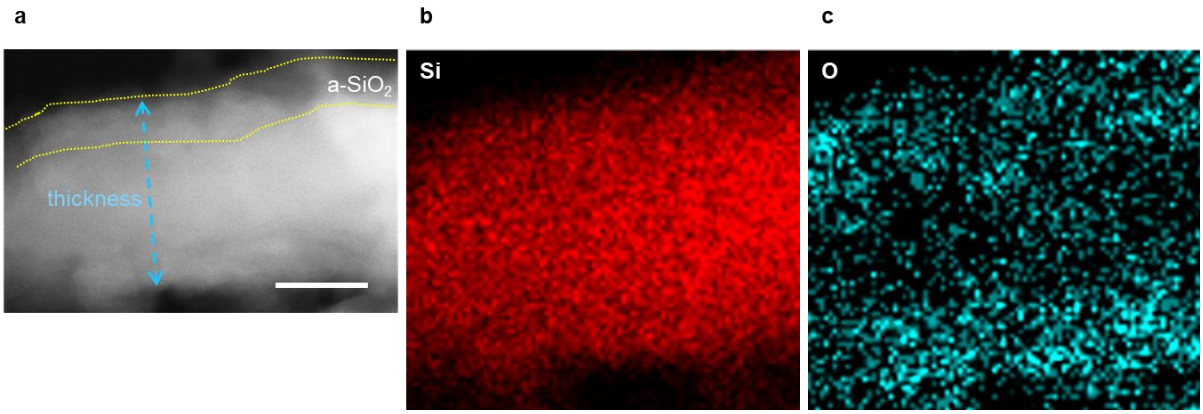

Figure 2-9 STEM image of Si@SiO_2 for the cross-section with EDS mapping by Si and O elements, respectively. Scale bar: 20 nm.

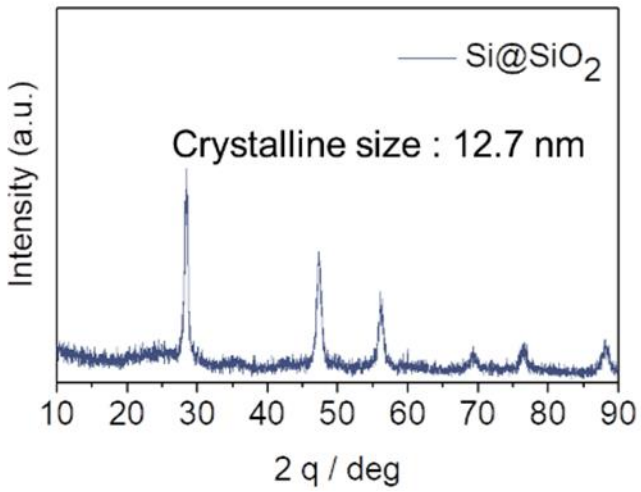

Figure 2-10 XRD characterization of Si nano-particles passivated with SiO_2 nano-layer.

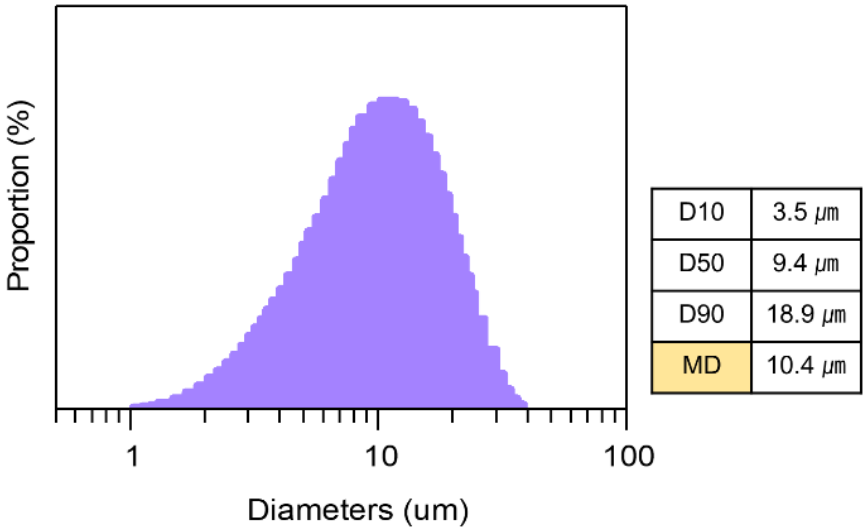

Figure 2-11 PSD and representative size (D10, D50, D90 and mean diameter) of SCM.

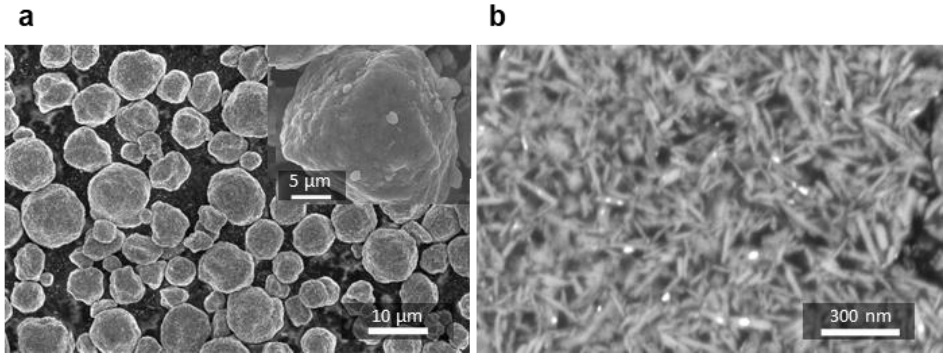

Figure 2-12 (a) morphological and (b) cross-sectional analysis of Si@SiO_2@C by SEM

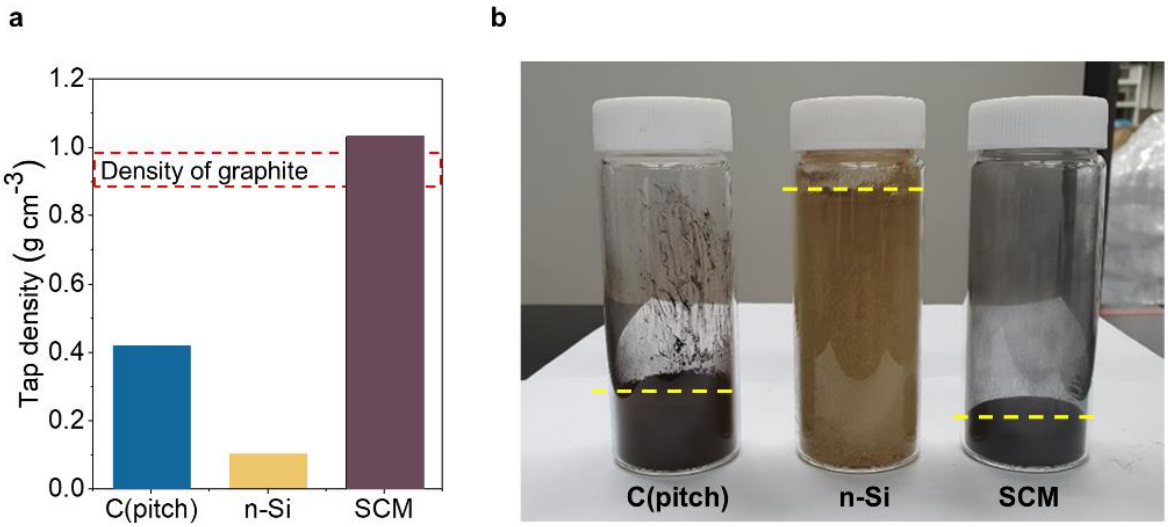

Figure 2-13 (a) Tapping density analysis of C precursor, n-Si and SCM comparing to commercial graphite, (b) photograph for 10 g of C precursor, n-Si and SCM.

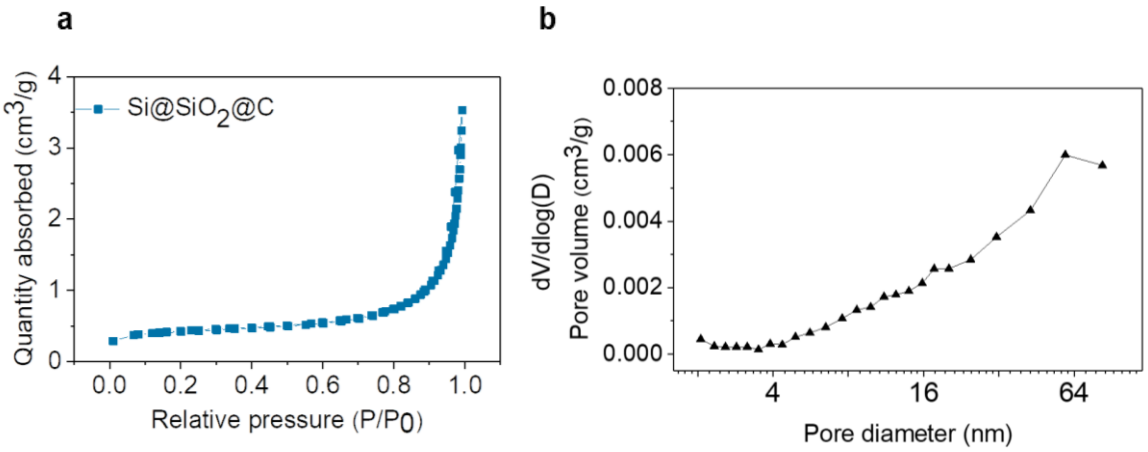

Figure 2-14 (a) BET specific surface area and (b) BJH pore size distribution analysis about Si@SiO_2@C.

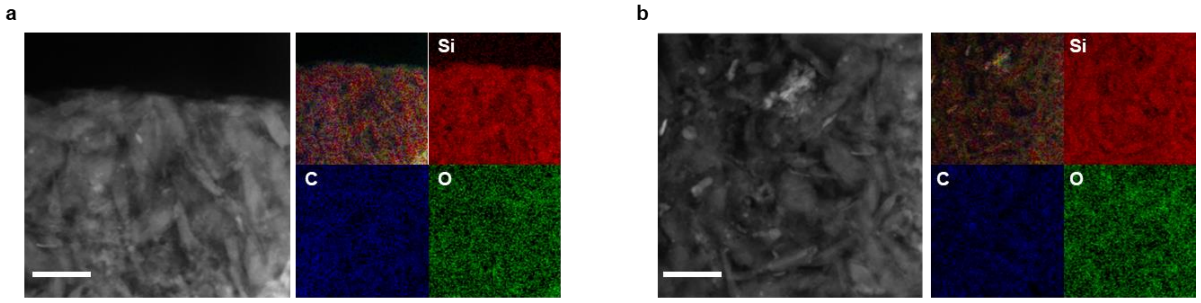

c

wt%	a (u-SCM)	b (SCM)
Si	70.3	61.3
O	14.4	10.2
C	15.3	28.5

Figure 2-15 STEM cross-sectional images with EDS mapping for Si, C and O elements, respectively. (a) u-SCM and (b) SCM. (c) Elemental ratio by EDS mapping. Scale bar: 100 nm.

.

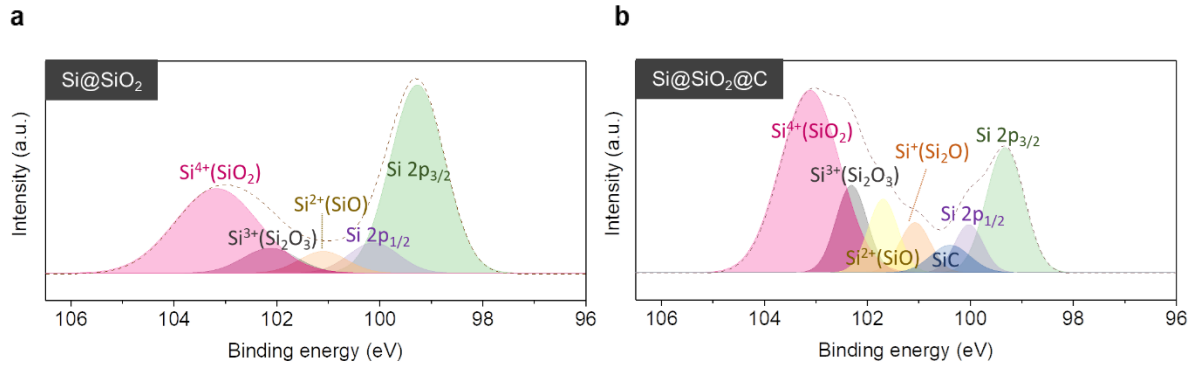

Figure 2-16 XPS spectra of Si 2p for (a) $Si@SiO_2$ and (b) $Si@SiO_2@C$.

Electrochemical characterization. We selected experimentally materialized two types of Si/C composite anodes based on the stress limit value (* 2 and * 4, Figure 2-4(a)). The composition was confirmed by elemental analysis (EA), exhibiting different C content of 15.3 and 26.1 wt% (Figure 2-17(a)), respectively. Inset TEM images show different nano-Si dispersion densities, and corresponding TEM EDS measurements (Figure 2-15) support this. To investigate the beneficial effects of the stress and capacity manipulation on battery performance, we compared the electrochemical properties of unstable stress-induced Si/C microparticles (u-SCM, representing * 2 type in the FEM study) and optimized Si/C microparticles (SCM, representing * 4 type in the FEM study) by coin half-cell configuration. The u-SCM half-cell delivered an initial discharge capacity of 1781 mAh g^{-1} and an initial CE of 85.7%, while the SCM achieved 1402 mAh g^{-1} and 83.3%, respectively low discharge capacity and efficiency (Figure 2-17(b)). Each anode was successfully synthesized with a rational capacity, which was expected by the FEM calculation. The slight difference of initial CE was ascribed to the relatively high composition of protective C content, causing enhanced irreversible reaction during the lithiation[24]. Both electrodes exhibited superior electric conductivity due to the structural merits of interlayered conductive C, with no obstacle in capacity contribution up to nano-Si distributed deep inside the microparticle. The results are well consistent with the calculated theoretical capacity (1784, 1380 mAh g^{-1}, Figure 2-4(a)). To demonstrate the feasibility of high capacity and energy density active materials, SCM and u-SCM were blended with artificial graphite (350 mAh g^{-1}) to fabricate electrodes delivering specific capacity of 650 mA h g^{-1}, which were then tested under practical test conditions presented in Experimental section. The required ratio of blended Si/C composite for SCM and u-SCM was 28.5 and 21 wt%, respectively. The obtained initial Coulombic efficiency (CE) of blended electrodes showed similar and superior results of 87.3 and 87.8%, respectively (Figure 2-17(b)), which exhibits slightly decreased differences comparing to that of solely used Si/C composite electrodes. SCM revealed better cycling stability resulting in 7.6 % retention difference after 50 cycle (96.3, 88.7 % at 50 cycles, respectively), meanwhile, the cycling CE rapidly increased above 99.5% after 5 cycles, and thereafter remained the level. The CE trend of SCM steadily showed about 0.3 % higher than that of u-SCM resulting from the stress stabilized effect, meaning the less consumption of Li source[99, 100]. In the case of the u-SCM, the activated tensile stress and volume change could continuously provide fresh reactive reaction site with electrolyte during the (de)lithiation process, which will contribute to boost production of irreversible Si contents deriving the capacity drop. Therefore, the optimized stress constraint can preserve the structural integrity of Si/C anodes following lower irreversible capacity loss. However, half-cell of the graphite blended electrodes (at the initial discharge capacity of 650 mAh g^{-1}) indicated these distinctions rarely occurred. SCM and u-SCM exhibited stable capacity retention after 50 cycles with 92.8 and 93.2%, respectively. The relatively small ratio of Si/C composite (21 and 28.5 wt%), high electrical conductivity of graphite and high electrode density (1.6 - 1.65 g cm^{-3}) can hinder

the electrical break of active materials and maintain the capacitive contribution of Si within the electrode despite their CE difference (Figure 2-17(c)). In case of half-cell configuration, the Li consumption by irreversible reaction would not be critical for these samples, because they still exhibited evident lithiation compatibility after many cycles in u-SCM with similar retention and lower CE.

We performed rate capability investigation, when the current density was varied from 0.5C to 5C for the same electrodes as half-cell evaluation (Figure 2-17(d)). The results of rate capability for the solely used Si/C composite were presented as with comparable trend (Figure 2-18). As shown in figure 2-17(d), specific capacity was maintained on the both of electrodes up to 2C (7.2 mA cm^{-2}), while rapid capacity drop occurred at 5C (18 mA cm^{-2}) in case of u-SCM, which is possibly due to the massive formation of electrically resistive layer (solid electrolyte interface, SEI) on the anode parts. The capacity recovers following to cycle progression and both of the electrodes were almost achieved original capacity by decreased current density to 0.5C (1.8 mA cm^{-2}).

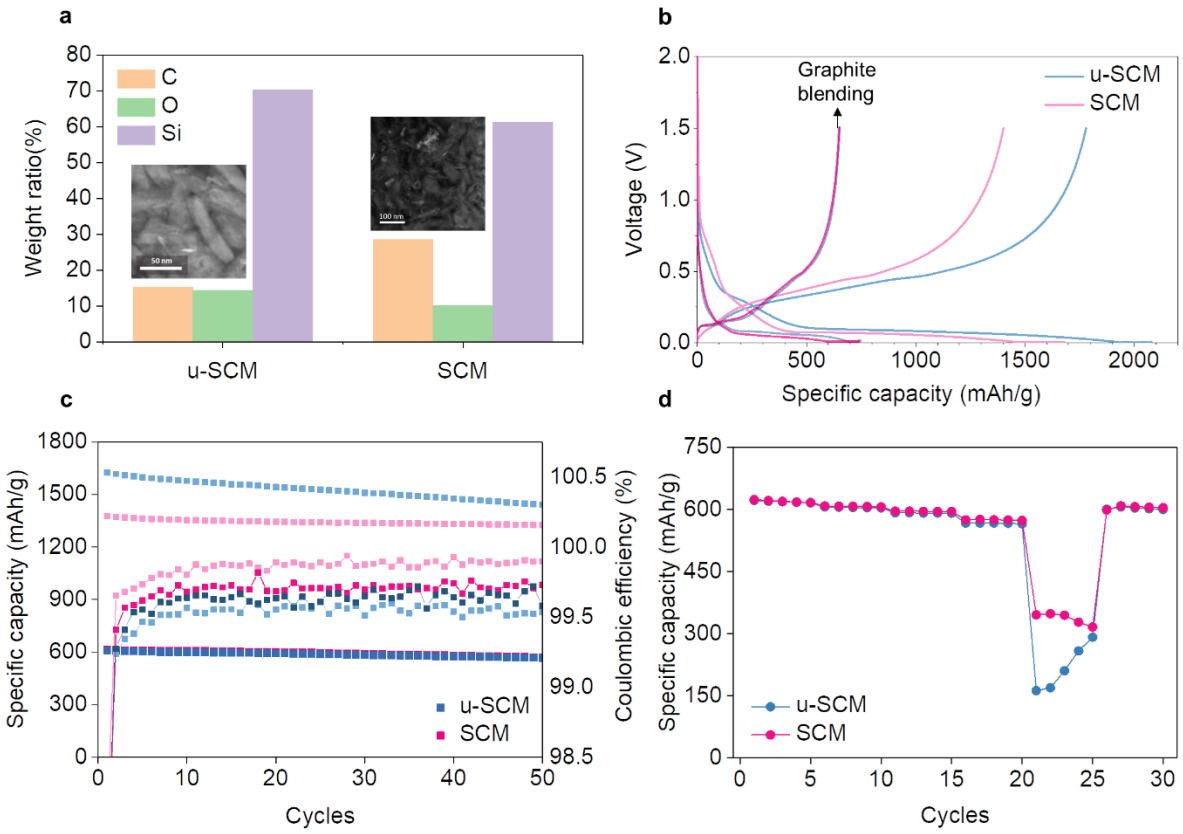

Figure 2-17 Electrochemical and TEM elemental characterizations. (a) Elemental composition ratio of SCM and u-SCM by Si, O, and C elemental mappings (inset STEM images by ion slicing), (b) first-cycle voltage profiles for solely and blended electrodes of SCM and u-SCM, (c) discharge capacity and Coulombic efficiency for solely and blended electrodes of SCM and u-SCM, (d) Rate capabilities of SCM and u-SCM blending electrodes under various current densities: 0.72, 1.8, 3.6, 7.2 and 18 mA cm^{-2}.

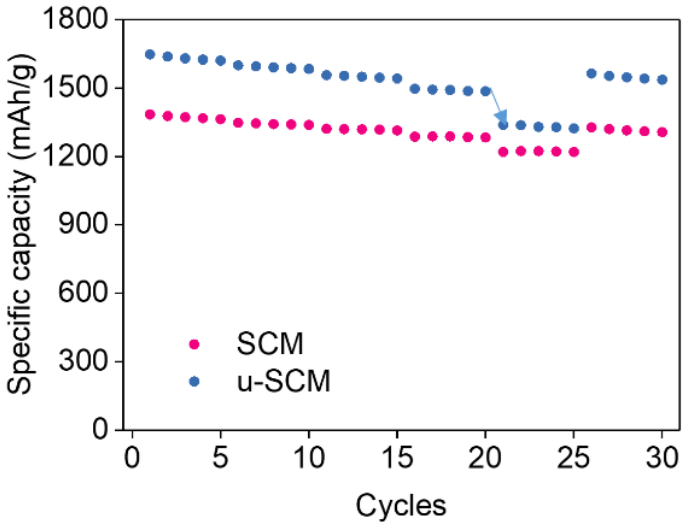

Figure 2-18. Rate capabilities under various current densities: 0.2, 0.5, 1, 2 and 5C.

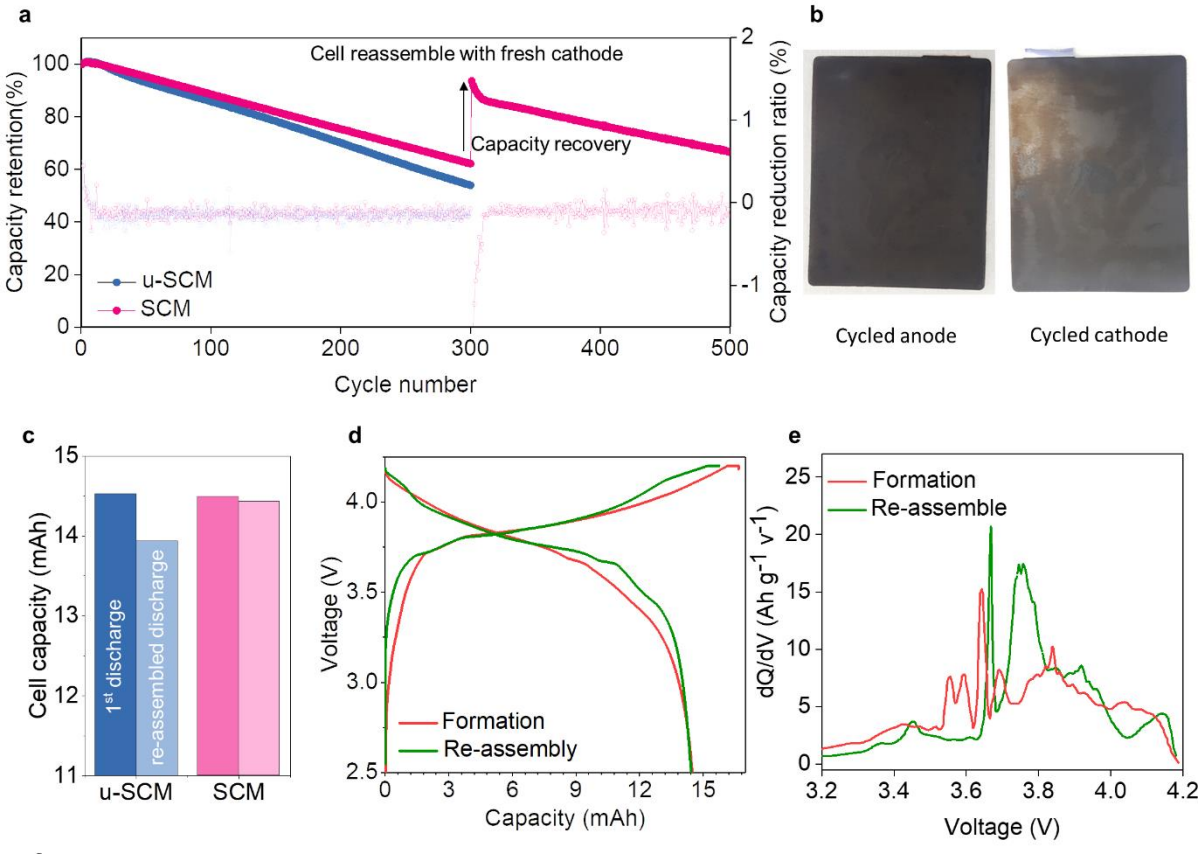

Figure 2-19 Electrochemical characterization of full-cells. (a) Full-cell test of SCM and u-SCM electrodes for 300 cycles and cycle life of reassembled cell with the fresh cathode and cycled SCM anode, (b) optical images of cycled anode and cathode, (c) discharge capacity of full-cell at first formation cycle and reassembled cycle, (d) first-cycle and reassembled cycle profiles of SCM applied full-cell, (e) discharge dQ/dv plot of initial and re-assembled formation cycle.

Full-cell evaluation. To corroborate the feasibility on real battery systems of our composite materials (u-SCM and SCM), we fabricated prototype pouch full-cells and electrodes stacked 1 Ah full-cells with lithium cobalt oxide (LCO) cathode. Figure 2-19 (a) exhibits the cycle retention of pouch full-cells, which was comprised of the anodic areal capacity of 3.6 mAh cm^{-2} and the N/P ratio fixed at 1.1. Corresponding initial CE was 86.1 and 86.9 %, respectively. Electrochemical test was performed to 300 cycles, then we reassembled the full-cell using cycled anode with fresh cathode and electrolyte to demonstrate the reason of capacity fading at anode part. The cycled anode and cathode were shown in figure 2-19 (b) and they were also utilized to half-cell fabrication with Li as the counter electrode (Figure 2-20). Figure 2-19 (c) presents the discharge cell capacity of each cycled anode applied full-cell (see Figure 2-21 to see the voltage profile of u-SCM). While u-SCM presented steadily higher fading rate, SCM featured high cycle stability, resulting in 8 % higher capacity retention than that of u-SCM after 300 cycles (Figure 2-19 (a)). The electrochemical performance of relatively excessive C contained SCM (e-SCM) was presented in figure 2-22. Their average capacity reduction ratio was approximately constant upon cycling with 0.126 and 0.153 %, which is attributed to the mechanical stability of microparticles and comparable to CE difference of half-cell configuration. For the reassembled cell, rapid capacity drop occurred during the initial 10 cycles. However, the capacity reduction rate has been stabilized similarly to that of the original full-cell. The Si/C composite anodes maintained its superior cycle stability after the reassembling. Furthermore, the reduction rate had been improved instead to 0.106 % during 311 ~ 500^{th} cycles. Voltage profiles of before and after the reassembly of full-cell were shown in figure 2-19 (d), and the reassembled full-cell recovered its original capacity, indicating that almost all the embedded Si is active even after long-term cycle. While the discharge capacity expected to be implemented from SCM in reassembled full-cell shifted to decreased value in comparison with the original cell, it is highly small considering the capacity deterioration during 300 cycles. The recovered discharge capacity ratio (95.9%) of reassembled full-cell comparing to the original cell of u-SCM exhibited just 3.7 % less value than that (99.6%) of reassembled SCM full-cell (Figure 2-19 (c)). We developed differential capacity characterization (dQ/dV, Figure 2-19 (e)) about 1^{st} and 301^{th} cycle to clarify the discharge behavior change of reassembled cell. Over potential was generated due to the resistance layer (SEI) formed on the surface of the Si/C composite materials during 300 cycles, but the de-lithiation peak (3.2 - 3.5 V) of Li_xSi is clearly seen. Trends of the corresponding peaks were observed in reassembled half-cell (Figure 2-23). This means that adequately designed Si-based anodes can still maintain cell capacity and implement almost its original capacity by the presence of an extra Li source despite the mechanical degradation of Si, as the half-cell evaluation does with excessive Li. The irreversible Li loss of cathode following the gradual inactivation during the lithiation mechanism of each cycles at anodes can be concluded to the main reason of capacity fading in long life span, rather than the deterioration of anode materials.

To further investigate the feasibility of Si/C composite at industrial standards, we fabricated 1 Ah full-cells with SCM (560 mAh g^{-1}, 20 wt% blending with graphite) then evaluated long-term cyclability at two temperatures (25 ℃ and 50 ℃) and exhibited the results in figure 2-24 (a). Even with industrial standards of electrode fabrication for high energy density, both of cells demonstrates outstanding and enhanced cycling stability at super long-term cycles (800^{th}) in a full-cell without any rapid capacity drop, which demonstrates consistent capacity contribution and no electric isolation of Si-based materials. The SCM presented superior rate capability for the discharge characteristics in 1 Ah full-cells (Figure 2-25). The in-situ thickness measurement was performed with 1 Ah full-cell during the initial 50 cycles (Figure. 2-24 (a))[101]. From the 50 ℃ evaluation, the thickness variation remained higher and showed an increased slope. In high temperature environment, high reactivity is predominant in accelerating the irreversible reaction, which induced the SEI thickening by the enhanced side reaction in the anode part. Nevertheless, while the side reaction stabilizes through the long lifespan, both cycle trends were similar, which would be ascribed to the mechanically stabilized SCM composite materials of our study.

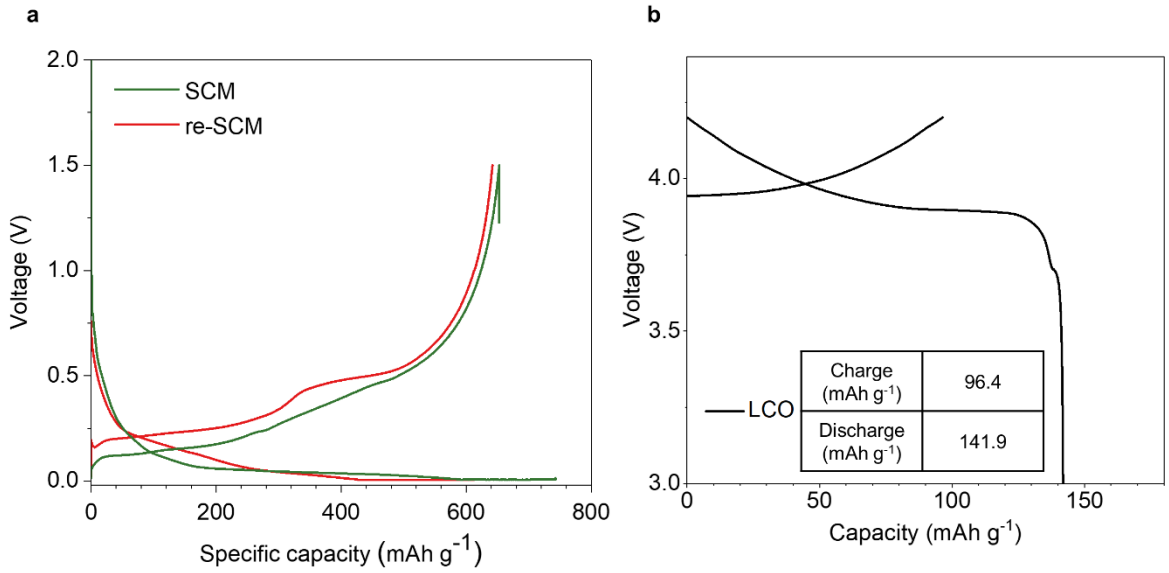

Figure 2-20 Re-assembled half-cell evaluation with cycled electrodes. (a) Voltage profiles of re-assembled SCM and (b) voltage profiles of re-assembled LCO with fresh Li foil after 300 cycles on the full-cell.

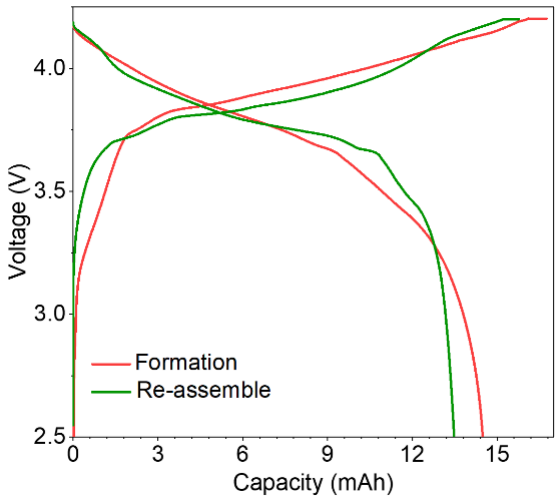

Figure 2-21 Re-assembled full-cell. Voltage profile of re-assembled full-cell with cycled u-SCM and fresh LCO after 300 cycles on the full-cell.

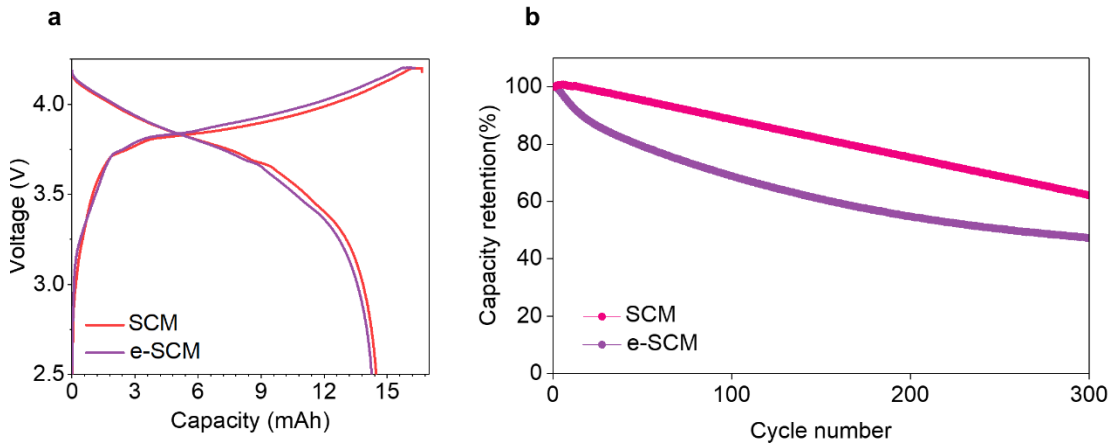

Figure 2-22 (a) Voltage profile of excessive C applied (e-SCM) Si/C micro particle (40 wt% blending for 650 mAh g^{-1}) and (b) full-cell cycle test for 300 cycles.

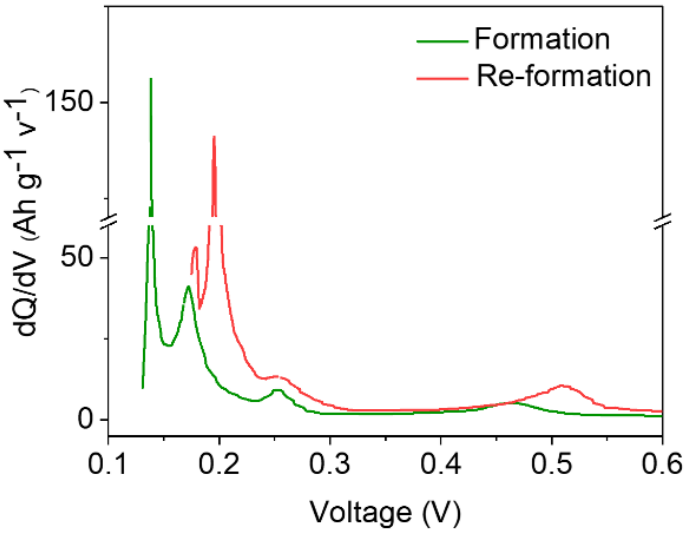

Figure 2-23 Re-assembled half-cell evaluation. Discharge dQ/dv plot of initial and re-assembled formation cycle with cycled SCM and fresh Li foil after 300 cycles on the full-cell.

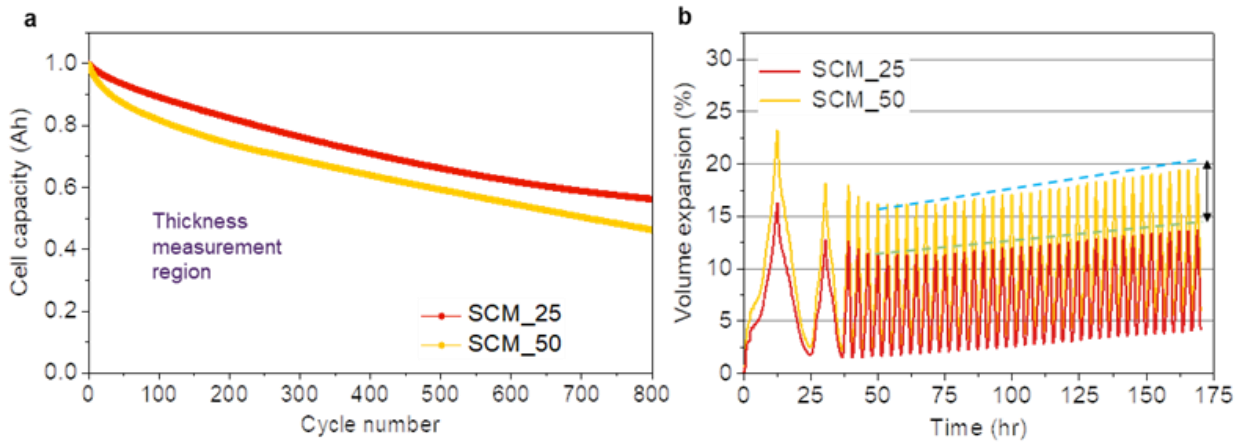

Figure 2-24 Electrochemical characterization of full-cells. (a) 1 Ah full-cell test of SCM electrode at 25 and 50 ℃, (b) electrode swelling behaviors during 50 cycles.

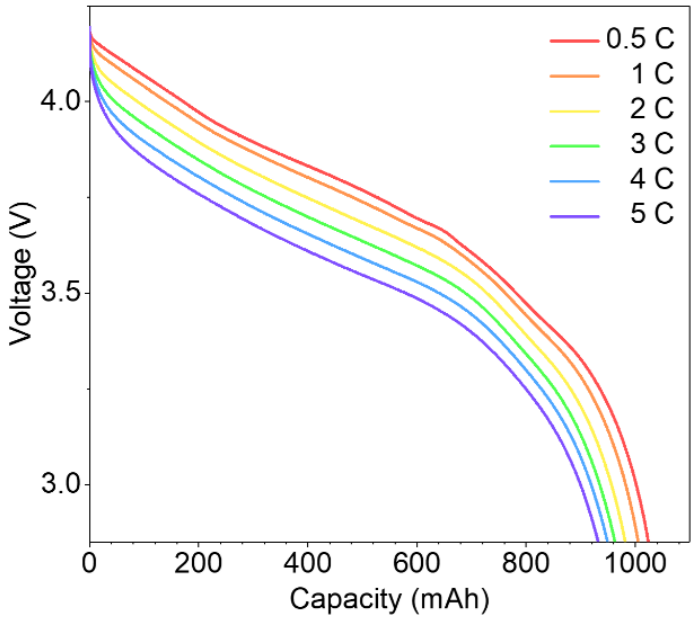

Figure 2-25 Rate capability at room temperature (25 ℃). Discharge profiles of SCM applied 1 Ah full-cell under various current densities: 0.5, 1, 2, 3, 4 and 5C.

Post-cycling analysis. Figure 2-26 (a) demonstrates comparative schematics of SCM and u-SCM with the mechanical stabilization effect of micron-sized particles. The higher nano-Si distribution density of u-SCM as a comparative group, shows relatively thinner interlayered C layer, which would be clear to form the cracks of C layer, accumulating the mechanical deformation upon the repeated cycling. Mechanical instability continuously exposes fresh interface to the electrolyte[102], which repeatedly occurs over the cycle lifetime, contributing to the formation of thick SEI layer. In case of SCM, the mechanical damage would only be focused on the surface of particles, which is attributed to SEI layer stabilization at the particle surface, resulting in superior cycle life.

To further study the results of electrochemical performance in terms of structural stability, we analyzed the cross-sectional SEM images of post-cycling electrodes (Figure 2-26 (b-e)). The contrasting particles stability was revealed even after 50 cycles, while the micro cracks of u-SCM were established at surface and inside of the particles (Figure 2-26 (b)). The morphological deterioration was getting worse upon repeating cycles, which finally enhanced inside pore and severe particle pulverization, resulting in permeated and accumulated SEI layer within the u-SCM (Figure 2-26 (c) and 2-27). The increased Li consumption and enhanced side reaction of u-SCM caused by additional exposure of inner Si to electrolyte are well matched with the result of the slope change at cycle curve after 100 cycle as in figure 2-19 (a). In contrast, SCM maintained its structural integrity without evident morphological degradation over 100 cycles (Figure 2-26 (d)). For the 300th cycled electrode, the SEI formed layer was shown to be thicker, but, the overall degradation of the particles did not proceed, and some deterioration was also confined only at the surface region (Figure 2-26 (e) and 2-28).

A large proportion of Si inside the SCM particles still remains intact compared to the degree of capacity degradation in full-cells, indicating the great part of Si can be operated in active state being blocked to electrolyte. The stable SEI layered structure was also assured by cross-sectional EDS mapping (Figure 2-26 (f)) of the cycled electrode at 100 cycle, presenting F (fluorine) arrangement on the SCM surface without penetration to inside of particles. The micron-sized particles are very well maintained their structure without pulverization, and Si is also observed densely inside the SCM, which are beneficial for preventing the electrolyte contact to Si surface and contributing to the superior improvement of battery properties for commercial feasibility. Consequently, the elastic C prevented the particle pulverization even with micron-size during the repeated cycle test, when the content was adjusted by the calculation method. Identifying the stress limit of the material itself and operating within the range will be imperative for stable operation in a long-term life, then the irreversible deformation of particles would be addressed. The side reaction between electrode and electrolyte could be decreased by enhanced structural integrity, which can mitigate the stress intensification and eventually electrodes deterioration without modifying the electrochemical test conditions.

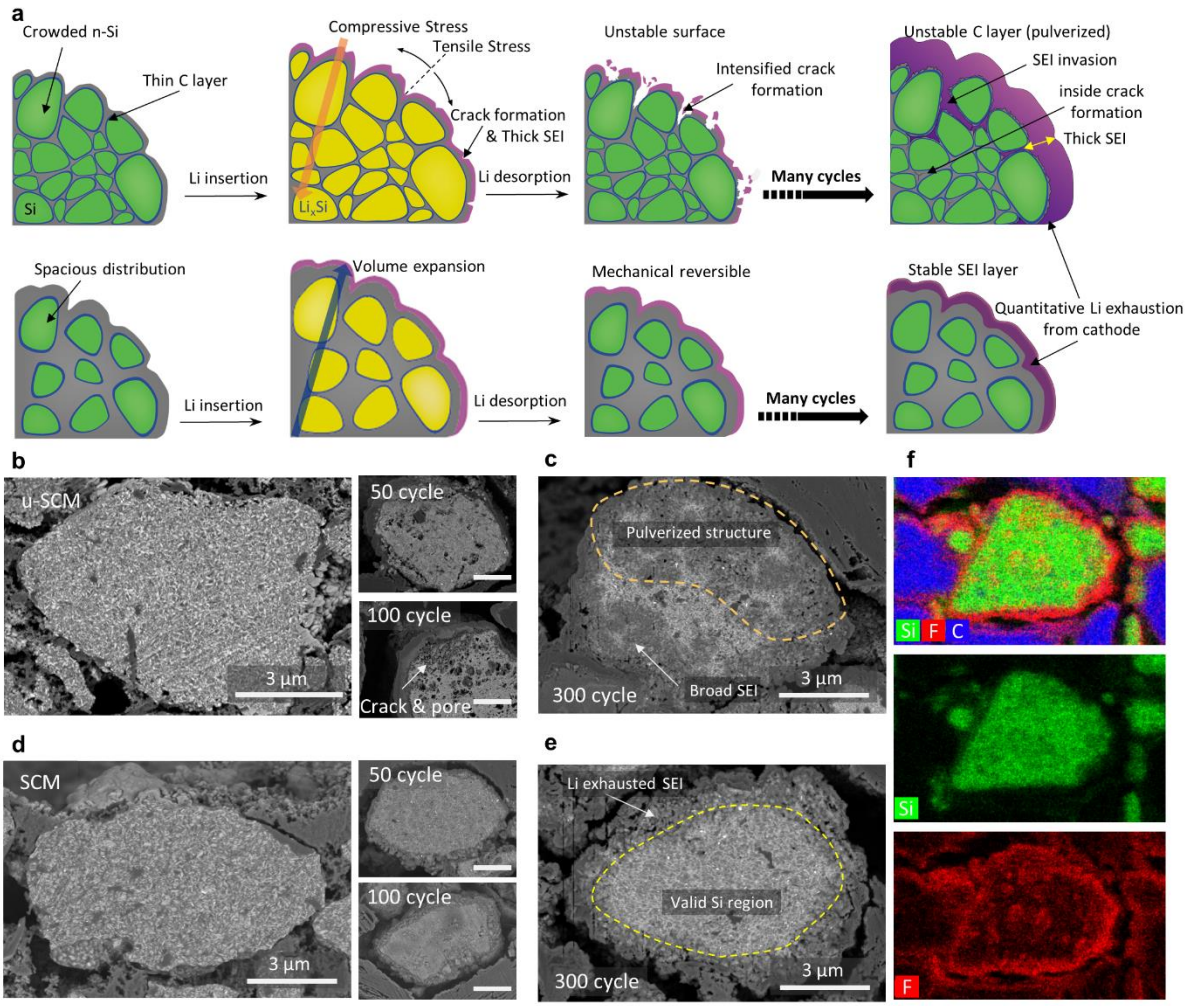

Figure 2-26 Scheme and cross-section analysis of post cycling electrodes. (a) Schematic illustration of the mechanical degradation and irreversible reaction effects in Si/C micro-particles during the long cycles. Cross-sectional SEM of u-SCM (b) bare and after 50 and 100 cycles, (c) after 300 cycles. Cross-sectional SEM of SCM (d) bare and after 50 and 100 cycles, (e) after 300 cycles. (f) Cross-sectional elements (Si, F and C) mapping of SCM after 100 cycles.

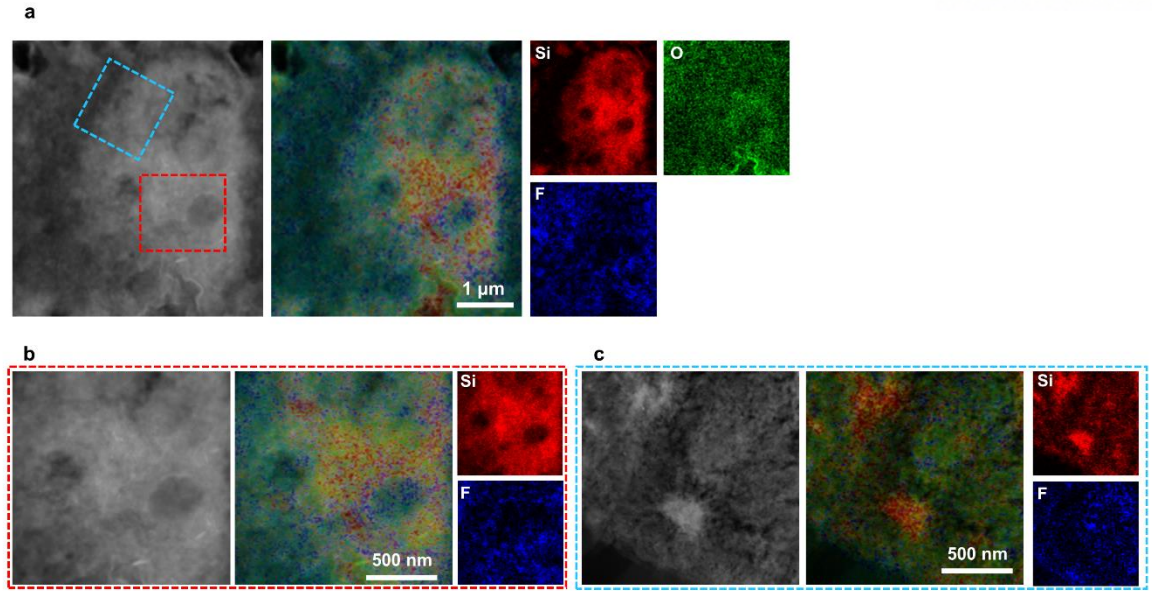

Figure 2-27 STEM cross-sectional images of cycled u-SCM (after 300 cycles) with EDS mapping for Si, O and F elements, respectively. (a) overall particle, (b) red line divided core region and (d) blue line divided surface region.

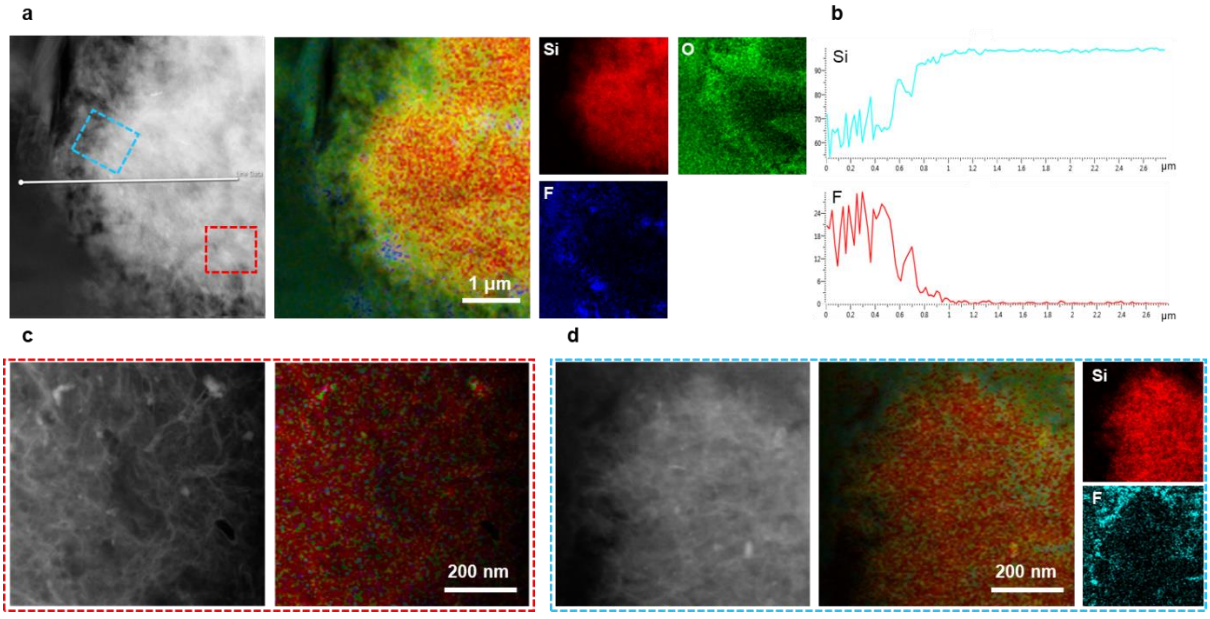

Figure 2-28 STEM cross-sectional images of cycled SCM (after 300 cycles) with EDS mapping for Si, O and F elements, respectively. (a) overall particle, (b) EDS line scan of Si and F from surface to core, (c) red line divided core region and (d) blue line divided surface focused region.

2.4 Conclusion

The diffusion induced stress of designed Si/C composite could be quantitatively revealed depending on C content by FEM study. Based on the calculation, our multifunctional composite material design in micron-sized particles demonstrates the solution for higher energy density anodes, and the stable capacity in long lifespan would be elucidated by lithiation capability decrease from protective matrices composition. When being prepared by calculation results, the well-dispersed nano-Si, mechanically enhancing SiO_2 and elastic interlayered C applied SCM worked collaboratively to overcome the intrinsic constraint of Si. Furthermore, rational size with the enhanced bulk density and extremely low surface area by these material designs developed the chance to be applied for practically feasible anodes with higher energy density under viable evaluation conditions. Mitigating the volume change by enhanced mechanical properties demonstrates the structural integrity of these materials, which contributes maintaining the active state of Si even after long cycle life. In the full cell evaluation, SCM provided outstanding cyclability without rapid capacity drop over 800 cycles, indicating the Si had been steadily utilized, not permanently disabled. Consequently, we believe our study can offer compelling guidelines for the implementation of high capacity and energy density anode materials with highly commercial opportunity for next-generation high energy batteries.

Chapter 3

Lithiated Lithiophilic (Li_xSi) Layer Induced Li Host Materials for Next Generation High-Energy Li-Metal Batteries

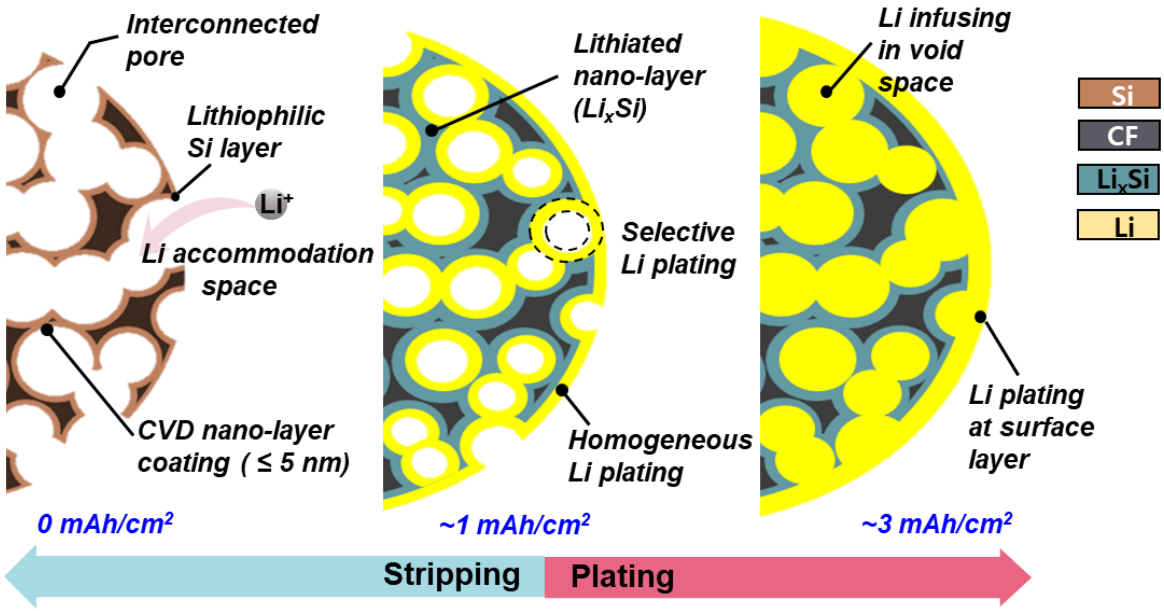

We synthesized ion and electron conductive carbon structure, which contains enough space to accommodate metallic Li during plating process. Li is intensely light metal denoting 0.534 g/cm^3 density that the required dense lithium thickness is 14.6 μm for areal capacity (≥ 3 mAh/cm^2). The interconnected pore structure containing 500 nm pore and showing 0.2 g/cm^3 tap density takes merits in expanded potential area for Li deposition. To incorporate lithiophilic surface layer, thermal decomposed Si nano-layer was deposited uniformly with 3 nm. The lithiophilic lithiated Si (Li_xSi) alleviated the polarization that it could induce planar Li nucleation and continuous Li accumulation at inner pore and outer surface region, followed by dense and smooth Li plating in electrode. The volume expansion of the electrode at lithiated state of 3 mAh/cm^2 was just 30% from 27 μm to 35 μm because of the adequate pore volume. And lithiophilic layer induced electrode exhibited prolonged lifespan and high power at high current density comparing to carbon frame without the Si layer.

This chapter is being prepared for submission.

3.1 Introduction

Li-ion battery application has been simultaneously widened with the development of portable devices. In particular, high volumetric/gravimetric energy density LIBs have attracted attentions due to the increasing demands for mass energy storage devices such as electric vehicles (EV) and energy storage system (ESS). Li metal has been inspired again as next generation preeminent promising anode materials because extensive researches of high-energy silicon anodes to commercialize it was insufficient to substitute graphite in terms of cycle stability.[103-107] Li metal facilitates extremely high specific capacity (3860 mAh/g) and lowest electrochemical potential (−3.04 V) that it features its high power and energy density.[108-110] However, the use of lithium metal batteries (LMB) was hindered from severe safety issues related to volume expansion from non-uniform deposition, uncontrollable dendrite growth and crack induced repeated SEI formation.[111-114] The above-mentioned reasons cause electrolyte consumption, low Coulombic efficiency, resulting in capacity deterioration and, more seriously internal short circuits and explosion.[115,116] Regulating Li plating and suppression of Li dendrites should be realized to solve the problems.

In the previous works, the volume change by Li insertion in anodes active materials for high-capacity LIB is a crucial issue, so porous structured materials were widely studied to accommodate this.[117-119] We reported these results with Si/C composite materials. An artificially formed porous carbon frame was coated with Si to synthesize Si/C composites, which would be expected to exhibit charge/discharge behavior inside the pores. A strategy to restructure the intrinsic pores of natural graphite to form a sufficient inner pore space was studied to accommodate the excess Si, maintaining the structural integrity from the expansion during charging (Figure 3-1).[120,121]

However, as in figure 3-2, the method of utilizing the porous structure has a limitation in improving the energy density because the internal space required for expansion must be emptied. The density of the electrodes demonstrates inevitably low value, which leads to decreased volumetric capacity. In addition, since this porous structure contains an empty space, it contains limitations in mechanical stability. In the charge/discharge behaviors of electrode materials with extreme volume changes, the structural collapse would be possibly generated in the electrodes and this affects fatal effects on deterioration of battery performance. The biggest limitation in practical applications of porous materials will be side reaction byproducts being expanded due to the large reaction area, which exhausts substantial Li and electrolyte. It can be an obstacle to battery performance improvement. Finally, all voids inside the porous structure will act as a resistive layer in electrons conduction. This will contribute to the polarization of the electrode and hinder the uniform electrode reaction.

There are several representative issues in the rechargeable lithium metal batteries (Figure 3-3).[122] They suffer formidable challenges by the Li dendrite formation during the Li plating process, which

enhance the polarization of electrode. Low cycling efficiency is also significant issue directly affecting the poor cycling performance of LMBs. Extreme volume changes are also accompanied by Li metal electrodes during charge and discharge, which leads to unstable SEI formation.[123-127] The above fetal issues are related to safety problems. For these reasons, tremendous studies have been tried to advance the Li metal electrodes in terms of the stability. Several effective strategies have been recently proposed about Li metal anodes via improved experimental approaches. Typical strategy including Li storage materials can store the plated Li reversibly within the sufficient empty space (Figure 3-4).[128] Lithiophilic characteristic materials applied electrodes are broadly researched with the effective Li deposition at the lithiophilic site with low polarization (Figure 3-5).[128-131] However, despite of these ardent studies to overcome the limit, Li metal anodes are still inadequate for practical battery application. There is an insurmountable gap between academic stage and practical level.

Here in, this study proposes a strategy of Li storage materials that satisfies the commercialization conditions. A structure was formed using a carbon material having excellent conductivity. This carbon material has a hyper porous structure, and as a result, the density of the material is extremely low and exhibits high porosity characteristics. Since these pores exist in an inter-connected structure, they have an advantage in diffusion of Li through the electrolyte. The pore diameter was synthesized and increased from 150 nm to 500 nm. This has the advantage of being able to deposit sufficient Li. Lithiophilic Si was added to the conductive carbon frame to increase the ease of deposition of Li by its lithiopjilicity. Since Si is uniformly deposited on all surfaces with a thickness of 3 nm and lithiated Si exhibits improved lithiophilic properties (Figure 3-6),[132] the sequential Li insertion process can have advantages. Compared to the seed type lithiophilic metal reported in the previous study, this 2-dimensional layered lithiophilicity is very effective for dense and uniform plating of Li, which was also verified through simulation. The volume expansion of the electrode at lithiated state of 3 mAh cm^{-2} was just 30% from 27 μm to 35 μm because of the adequate pore volume. And lithiophilic layer induced electrode exhibited prolonged lifespan and high-power performances at high current density comparing to carbon frame without the Si layer.

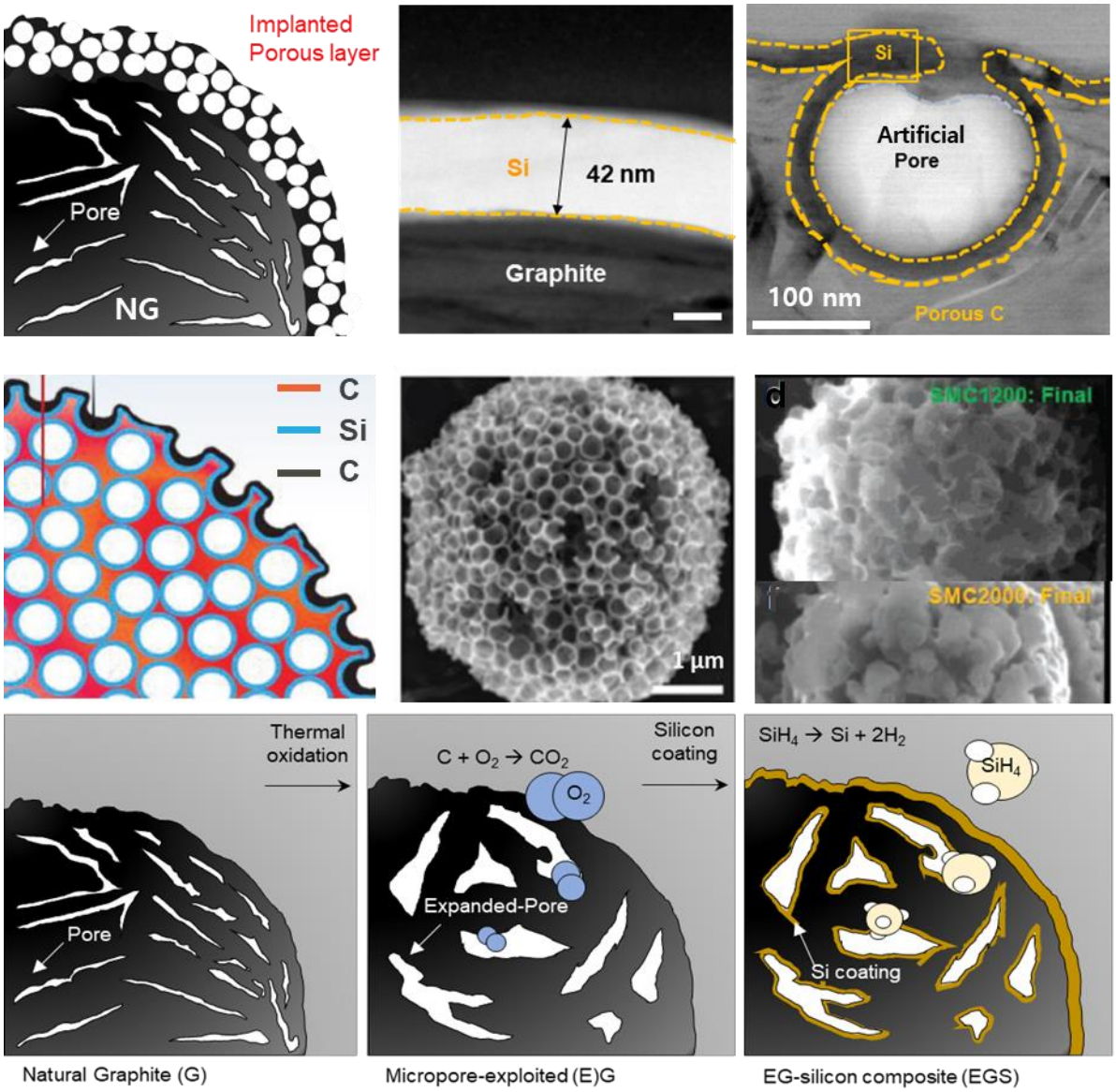

Figure 3-1. Prevoious work utilizing the porous structuire to accommodate the volume expansion of Si by lithiation.

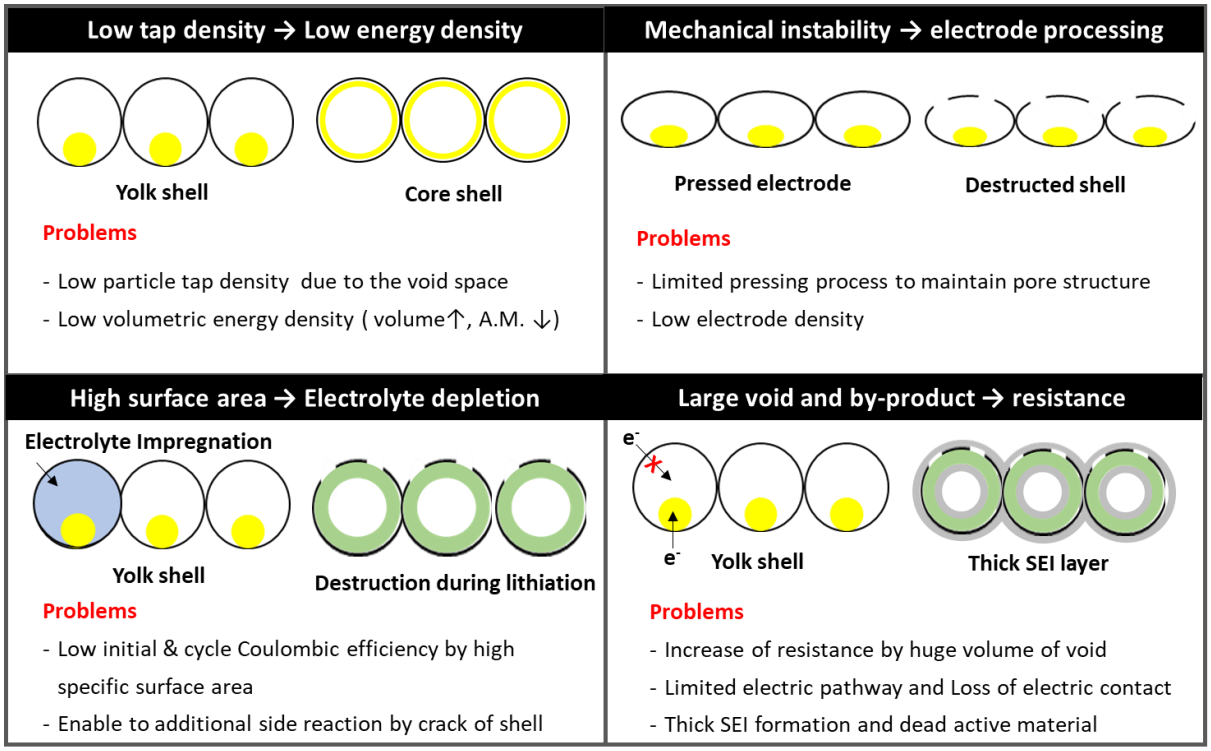

Figure 3-2. Limit of porous materials for practical anodes.

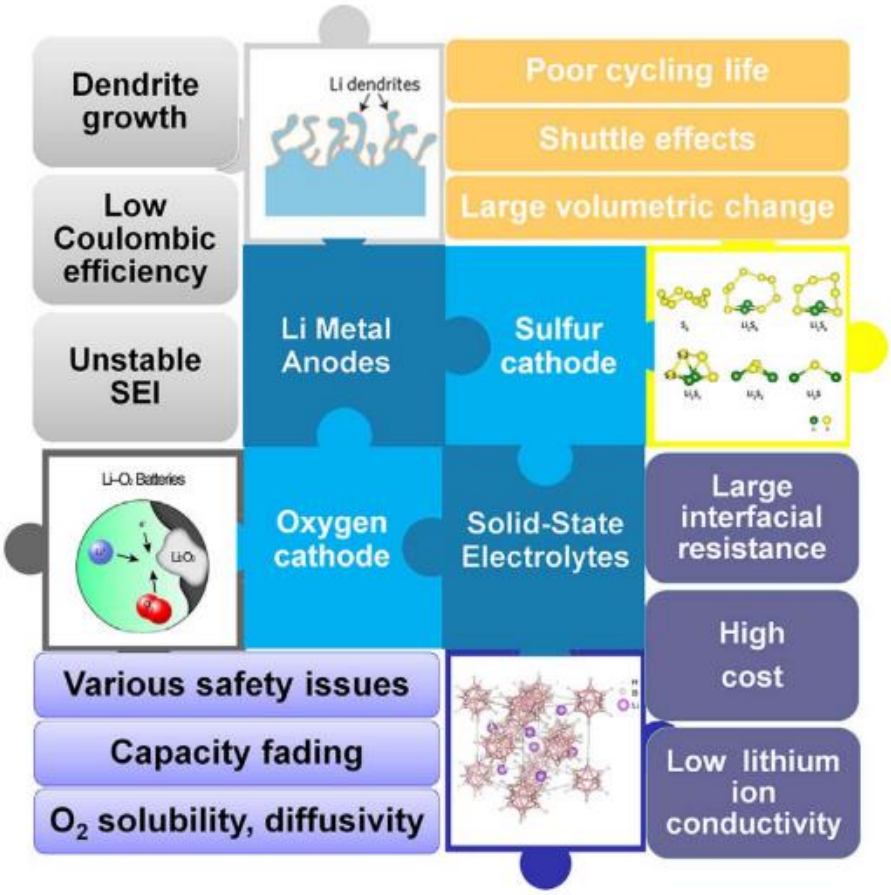

Figure 3-3. Crucial challenges and key parameters in next-generation Li metal batteries; sulfur cathode, oxygen cathode and solid-state batteries.

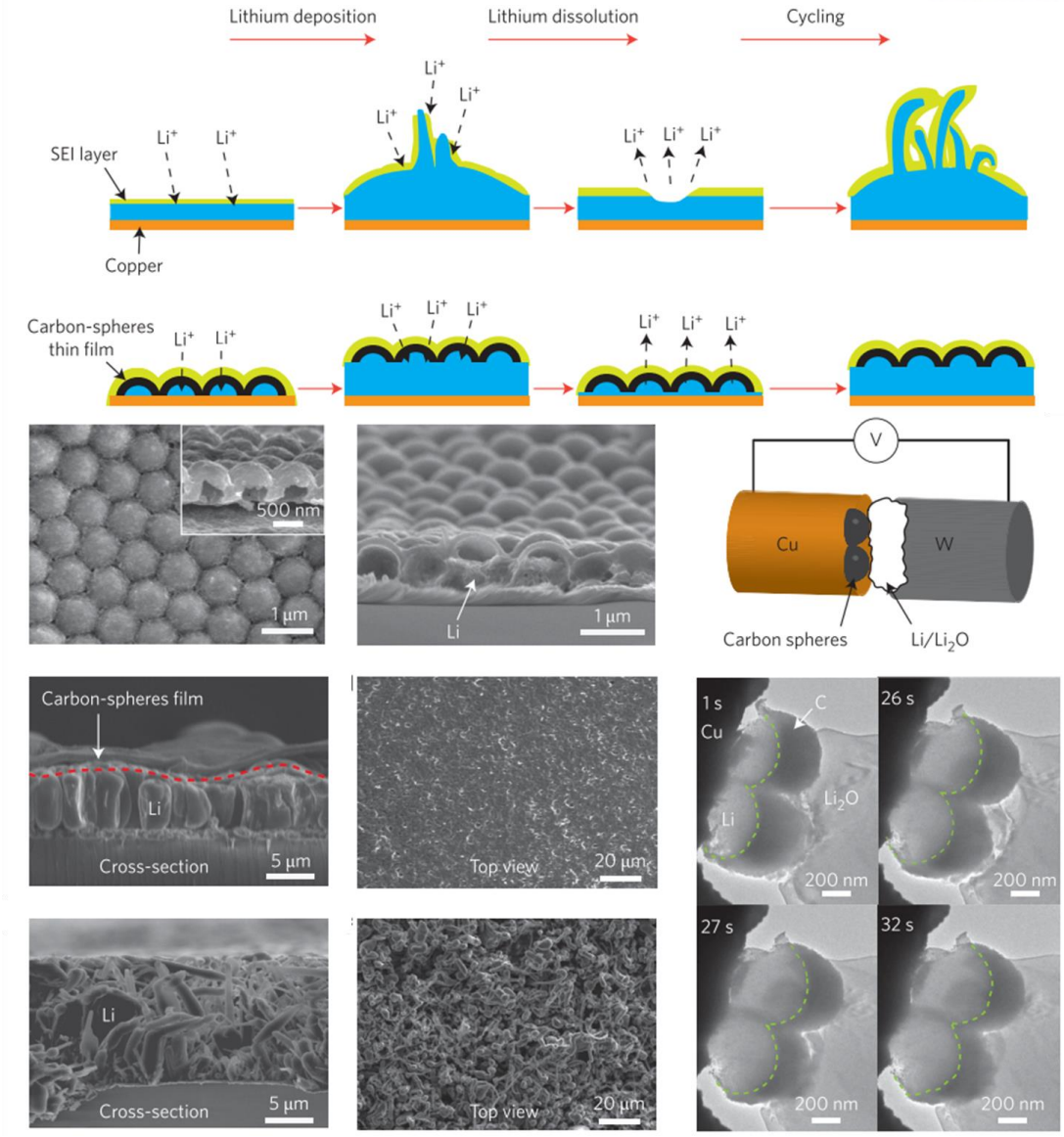

Figure 3-4. Schematic diagrams of hollow carbon nanosphere layer for lithium metal batteries and morphological analysis during and after the lithiation.

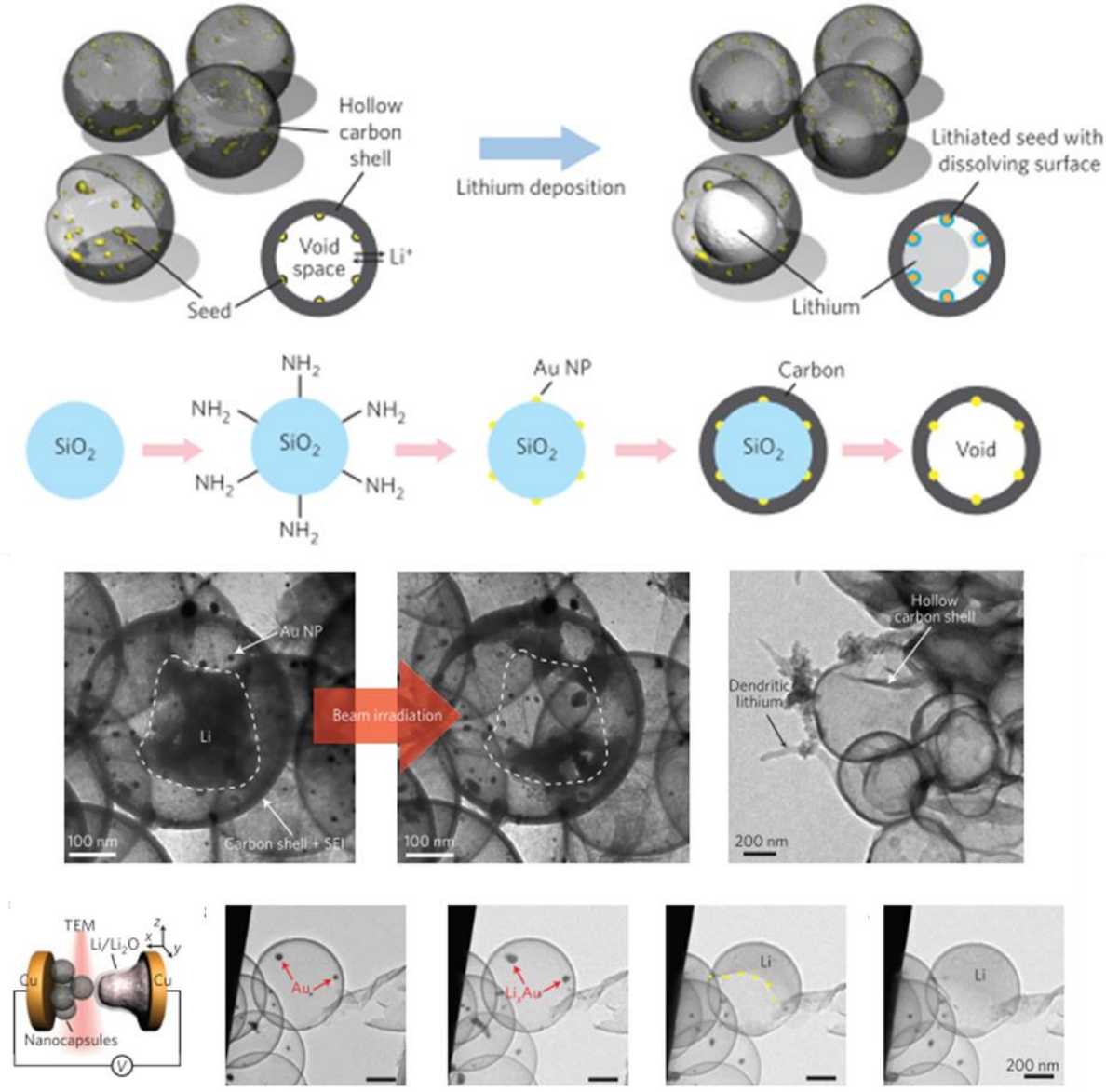

Figure 3-5. Schematic of Li metal nano capsules design for selective Li deposition by the being focused on the lithiophilic agent.

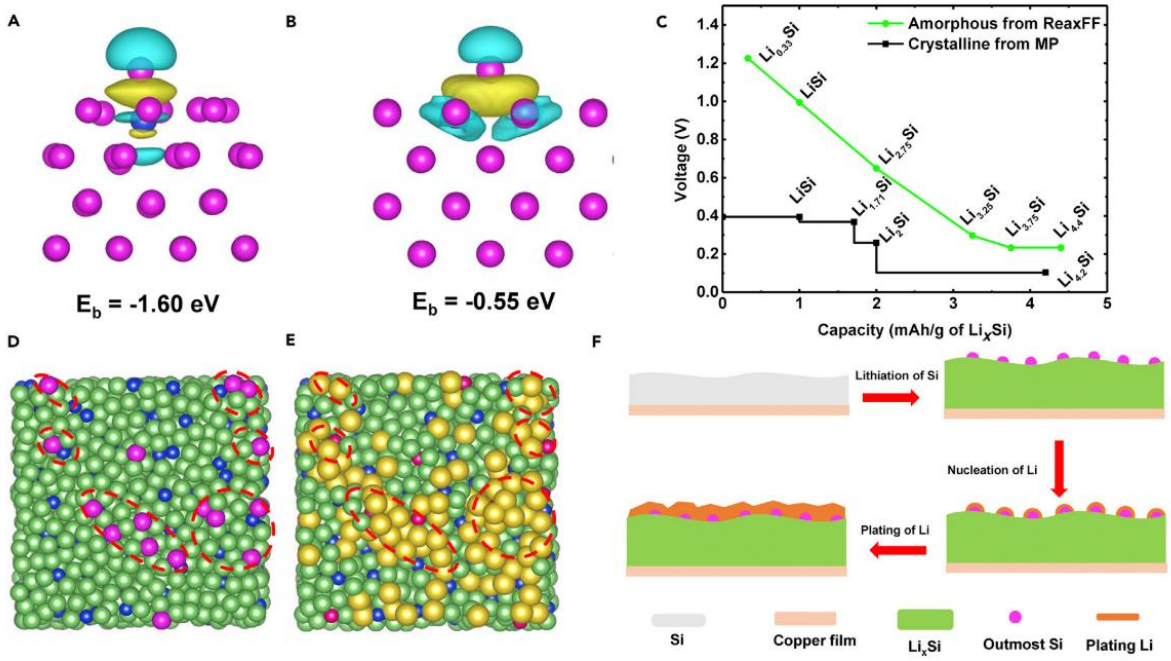

Figure 3-6. Calculation results by molecular dynamic and behaviors of Li-ion plating and stripping on the lithiated Si surface.

3.2 Experimental detail

Synthesis of PC. The porous carbon frame was synthesized via mechanical mixing with SiO_2 nanoparticle (with diverse diameter from 150 nm to 500 nm) and coal tar pitch (Posco Chemtech) in dry state. The Nobilta mixer (Hosokawa) was utilized for this mechanical mixing. The assembled SiO_2/C composite sphere was calcined with box furnace under N_2 atmosphere at 950 °C for 6 h. After the annealing procedure, the powder was dispersed in NaOH (3M) solution to form the inner pore of C framework by etching the SiO_2. Then, the solution was filtered with filter paper following several times washing with distilled water to wash out the residue from etchant. The porous carbon (PC) powder was obtained after the drying process under vacuum oven (Figure 3-7).

Synthesis of PC-S. The PC was loaded within the rotating furnace to form the uniform Si layer. High purity monosilane gas (99.9999%, KOSEM) was infused at 475 °C (50 sccm).

Materials characterization. Morphological and cross-sectional investigation of the samples was performed using scanning electron microscopy (SEM, Verios 460, FEI) with energy-dispersive spectroscopy (EDS, XFlash 6130, Bruker) and the high-resolution transmission electron microscopy (HR-TEM, JEM-2100F, JEOL) with EDS(Aztec, Oxford). To prepare the particles and electrodes for cross-sectional view, dual-beam focused ion beam (FIB, NX2000, Hitachi) and ion milling system (IM40000, Hitachi) were utilized. To investigate the crystallininty and structure, X-ray diffractometer (XRD, D/MAZX 2500V/PC, Rigaku) analysis was conducted (D/MAZX 2500V/PC, Rigaku). The specific surface area and pore volume distribution were examined with the nitrogen adsorption-desorption analyzer (TriStar II, Micromeritics).

Electrochemical characterization. The electrodes fabrication was conducted by homogeneously mixed slurry casting on Cu foil, composing of active material (PC and PC-S), conductive agent (carbon black, Super P, Imerys), carboxymethyl cellulose (CMC, Nippon paper) and styrene butadiene rubber (SBR, Zeon). The mass ratios of electrodes were 80:10:5:5. The areal capacity by plated Li can be adjusted from 1 to 5 mAh cm^{-2} (loading level with 1.2 mg cm^{-2}), followed drying process at 120 °C for 8 h under vacuum state. The electrode density was investigated in 0.26 g cm^{-3} due to the extremely low density of PC-S particles. CR2032 type half-cells were assembled in the Ar-filled glove box with separator (microporous polyethylene, 15 μm, Celgard) and electrolyte (1M LiTFSI in DOL/DME (1/1) 5% $LiNO_3$, Enchem). The electrochemical characterizations of half-cells were conducted with battery cycler (TOSCAT-3100, TOYO SYSTEM) at room temperature. The full-cell test was achieved with lithium nickel-manganess-cobalt-oxide cathode ($LiNi_{0.8}Mn_{0.1}Co_{0.1}O_2$, NMC811), which were assembled in humidity controlled dry room. Cathode was fabricated with NMC811 powder, conductive agent (Super P) and polyvinylidene fluoride (PVDF) binder at a mass ratio of 94:3:3. The areal capacity

and electrode density of cathode are 4.0 mAh cm^{-2} with the loading level of 21 mg cm^{-2} and 3.6 g cm^{-3}, respectively.

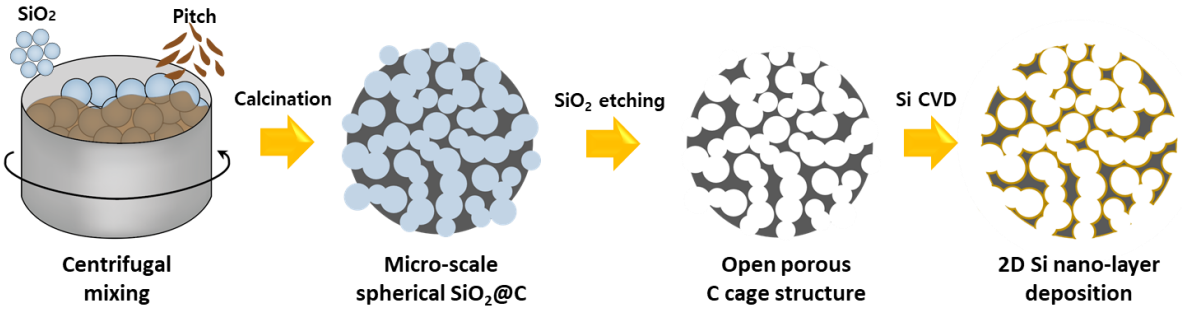

Figure 3-7. The schematic illustration to fabricate the porous carbon (PC) and silicon layered porous carbon (PC-S) by sequential steps; SiO_2@P mixing, SiO_2@C composite, porous-C framework, and Si layered porous structure.

3.3 Results and discussion

Strategy of lithiophilic layered conductive porous carbon structure for Li storage materials

Previously reported porous hosts, including the porous carbon structures and metal foams, usually exhibited poor lithiophilicity. It can lead to weak capillary force on the surface that the Li deposition was significantly hindered.[133-135] Recently, lithiophilic materials such as ZnO, Au, Ag and Si-based materials has been studied by the incorporation within the structures.[136-139] The improved lithiophilic characteristics of these hosts would accelerate the Li infusion and induce enhanced Li deposition at their surface (Figure 3-8).[140] In terms of the capillary pressure of porous structure, the radius and pore size will affect to the pressure with inversely proportional relation. Therefore, the pore size of host materials should be controlled with suitable diameter for achieving rational Li infusion. Lithiophilic porous frame can rapidly absorb the Li with smaller pore size due to large capillary force, which demonstrates increased capillary force can be induced by the Li deposition initiation due to the reduced pore size by Li deposition. This self-enhancing mechanism of Li plating will be beneficial as the Li host materials. In this regard, the large-sized pore can show the advantageous characteristics. The larger pore with large diameter would decrease the capillary pressure, resulting in slowed down Li infusion and precise Li deposition. To fabricate the porous hosts with rational surface characteristics and pore diameter is greatly important to realize desired deposition of Li metal within the anodes.

Here in, we tried to apply open porous carbon (PC) microparticles as the Li metal battery anodes. The open porous structure is advantageous for mass transfer of Li ions for the Li plating and stripping (Figure 3-9). The pore size and porosity can be adjusted by the synthetic procedure. The tap density of the synthesized PC microparticles shows a very small value, and the density of the electrodes to which it is applied exhibits very low results. This means that extremely high proportion of voids are included in the electrode, and all of these voids could be the capable volume to deposit the plated Li, ensuring sufficient energy density of the electrode (Figure 3-9b). The dense and uniform deposition of Li while suppressing dendrite growth in the void space is the most important segment of the development of Li metal anodes technology. Previous studies have tried various methods to solve this problem, and this study tried to utilize lithiophilicity.[141,142] An extremely thin lithiophilic 2D layer was introduced to induce uniform deposition of Li. This will be an efficient way to achieve optimized effect with minimum content of lithiophilic materials. In addition, we can achieve Li plating in the most effective way by giving lithiophilic properties to all exposed area compared to existing research about lithiophilic nanoparticle introduction.[137,143-145] In this study, a favorable CVD process was used for uniform deposition of Li and Si was used as a lithiophilic agent.

In particular, the amount of Si is a very important parameter for improving the energy density of a Li

ion battery, where the Si was utilized as anode active materials. In general, the theoretical capacity of Si is known to be 3579 mAh g^{-1}, but this value is calculated only by alloyed Li without considering the mass of Si. However, in order to compare the actual gravimetric capacity with the Li metal anode, the weight of Si itself must be considered. This is because the weight of the Li host materials also directly affects the gravimetric capacity and energy density of the anodes. Therefore, the theoretically calculated results in consideration of this is presented in Figure 3-10. Actual capacity considering the weight of Si does not change with 1857 mAh g^{-1}. On the other hand, Li metal anodes have confirmed that this value can be changed according to the weight of the host material, so it can be inferred that the actual energy density is improved as the weight of the host material is decreased.

Accordingly, the sequential schematic diagram during the operation process was presented, and the host materials reflected the strategy of this study (Figure 3-10). Interconnected pores improve the accessibility of Li ions by the electrolyte and provide sufficient space for Li ions to be plated. The Si layer is uniformly coated on the whole surface by the CVD process, which exhibits lithiophilic properties. In the electrochemical lithiation process, Si layer is preferentially charged into the Li_xSi phase, followed by deposition of pure Li on its surface. As the areal capacity increases, the inside pores will be filled with Li metal and will be emptied again in the stripping process. Stable charge and discharge behaviors will be possible by repeating process.

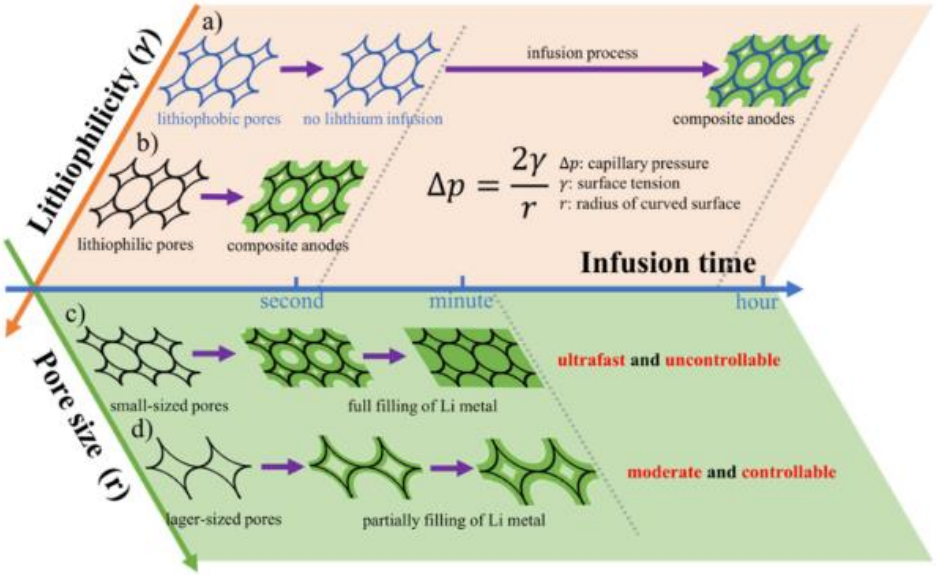

Figure 3-8. The complex effects of porous host materials (pore size and lithiophilicity) in terms of thermal infusion behaviors.

Regulating Capillary Pressure to Achieve Ultralow Areal Mass Loading Metallic Lithium Anodes

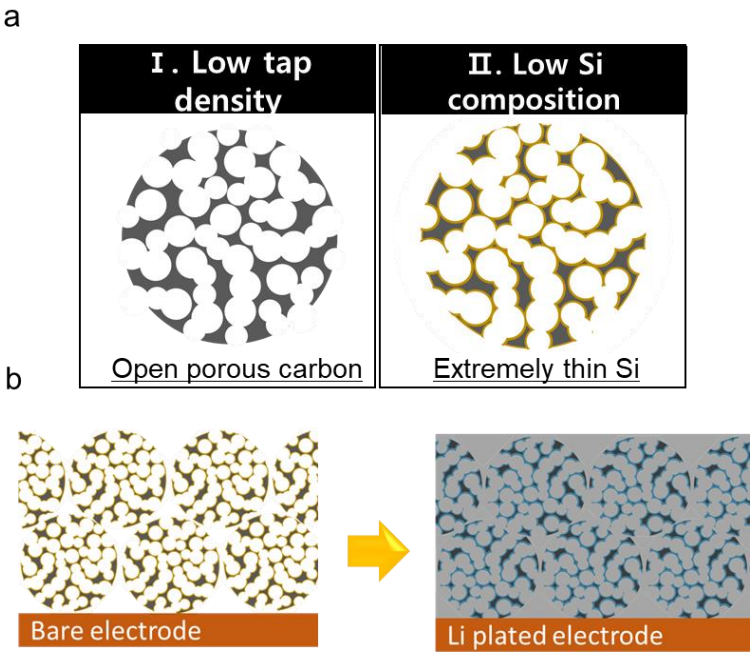

Figure 3-9. (a) Strategic strength in structural characteristics of PC and PC-S for the tap density and Si content of PC-S materials, and (b) cross-sectional schemes of bare electrode and Li plated electrode.

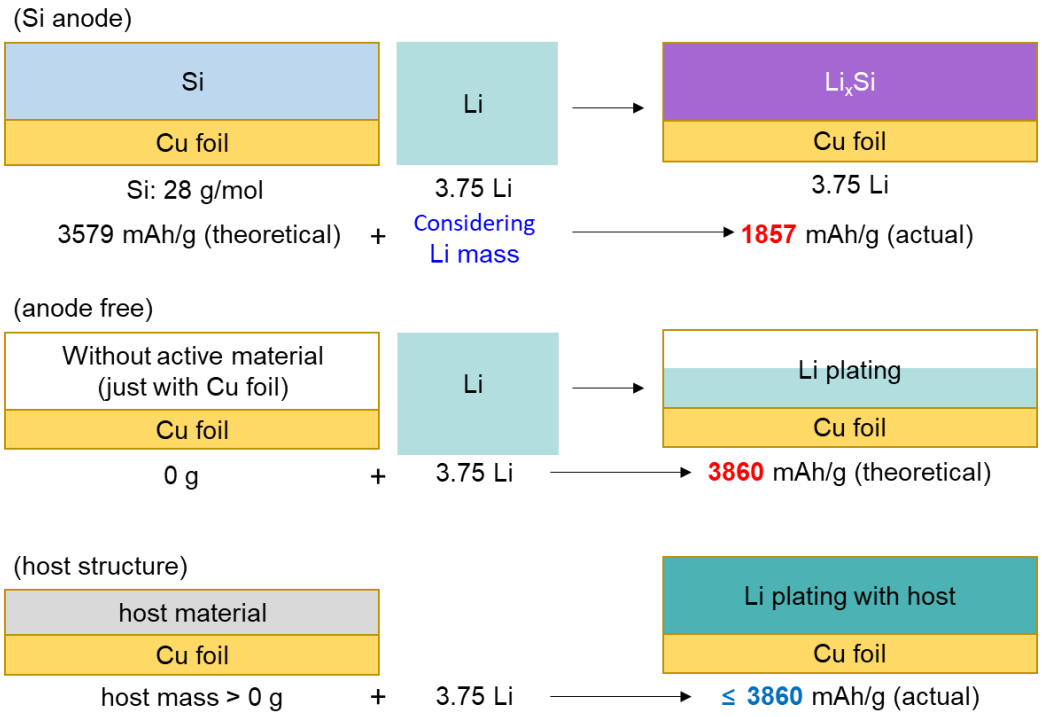

Figure 3-10. Actual gravimetric capacity of Si and Li metal anodes considering the mass of themselves within the electrodes.

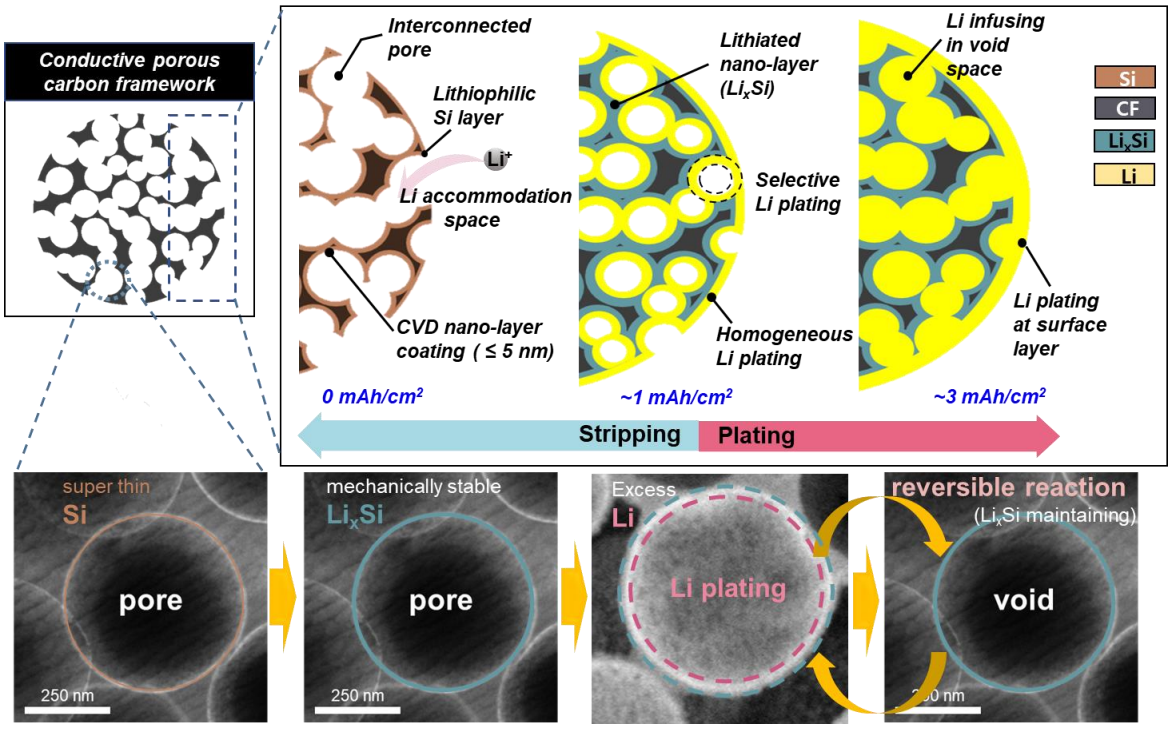

Figure 3-11. Sequential schematic illustration during the PC-S operation (plating and stripping) by the structural characteristics of the designed material.

Fabrication of rationally optimized porous carbon structure for Li storage

The pore size in the structure of porous carbon will be a important parameter in this study, and we wanted to control it. Considering the production process of porous carbon obtained by stirring the SiO_2 nano sphere, various sizes of SiO_2 were synthesized and confirmed using SEM (Figure 3-12a). The synthesized PC structures using the different sized SiO_2 nanosphere were exhibited in Figure 3-12b, and the size of each PC micro-particles were adjusted to a similar diameter. Through the figure 3-12b, each particle had a difference in density due to the size of the SiO_2 template. In the relatively small particle size of the SiO_2 template, the space excluding pores is densely filled, whereas in the large template, pitch carbon is mainly arranged around the template, and each spherical porous carbon is gathered like a grape cluster. The difference in structure may demonstrate the discrepancy in impregnation of the electrolyte. Unlike stepwise impregnation from the surface in the small sized pore structure, the large sized PC take sufficient channel to be impregnated to core region. Isotropic diffusion would be possible in 500 PC structure, resulting in uniform Li plating at any surface of Si layer. Si is deposited on the surface of each PC via the CVD process. Uniform coating using a CVD process is a very challenging assignment, and for this purpose, the flow rates of career gas and Si precursor gas were precisely controlled. For the samples by this procedure, TEM analysis was performed to investigate the structure of the synthesized Si-layered PC (PC-S). For precise observation of the Si layer, the cross-section of the synthesized powder was executed using ion slicing equipment (Figure 3-13). The TEM cross-sectional image clearly shows the conductive carbon network and Si nano layer. The Si thickness of about 3.2 nm was confirmed on the surface of the inner pore, and it was confirmed that it was formed very uniformly on the surface of PC. EDS analysis was carried out and supplemented for elemental analysis (Figure 3-14). The distribution of the Si component set to blue color showed a clear band shape on the surface of the pore, which could prove the rationally deposited Si layer on the PC surface. The uniform and suitably formed Si as intended was indicated through the above results.

After the fabrication of the PC-S, we performed pore characterization analysis at the electrode level. Mercury porosimetry was used, and the results for the smallest pore diameter sample and the largest pore diameter sample were compared (Figure 3-15 and Table 3-1). The above imaging analysis of SEM and TEM were confirmed to and matched very well with the porosimetry. The small pore diameter sample (100 PC-S) showed narrow pore size distribution in the inner pore region, and the average pore diameter was calculated to be 83 nm. In case of large pore diameter sample (500 PC-S), the inner pore size distribution demonstrated broad peak from 100 nm to 1000 nm, because the open porous structure was hostile to detect the precise pore diameter within the structure. We can also see the voids between the particles within the electrodes. There are different trends for the small and large pore samples. Small voids were confirmed from the 500 PC-S, while the larger voids were distributed with narrow size

distribution. The specification of electrodes is presented in Table 3-2. The schematic illustration of distinctively pore size demonstrates the factors affecting the Li deposition (Figure 3-16). First, the deposited Si content should be adjusted to the surface area resulting from the pore size, because to successfully form the uniform 2D layer on PC structure should be determined by the deposition area. The Si content would be higher in small sized pore sample, assuming the equal thickness of 2D Si layer with different pore diameter of PC. When the Si layer of the same thickness is formed, the remaining possible space for Li deposition is to be different. Since the volume of the Si layer increases during the lithiation process, the remaining space is further reduced. The number of pores itself is higher in small sized pore sample that it does not directly represent the difference in total void volume, but it can be confirmed that large pore diameter is more advantageous for rational Li plating.

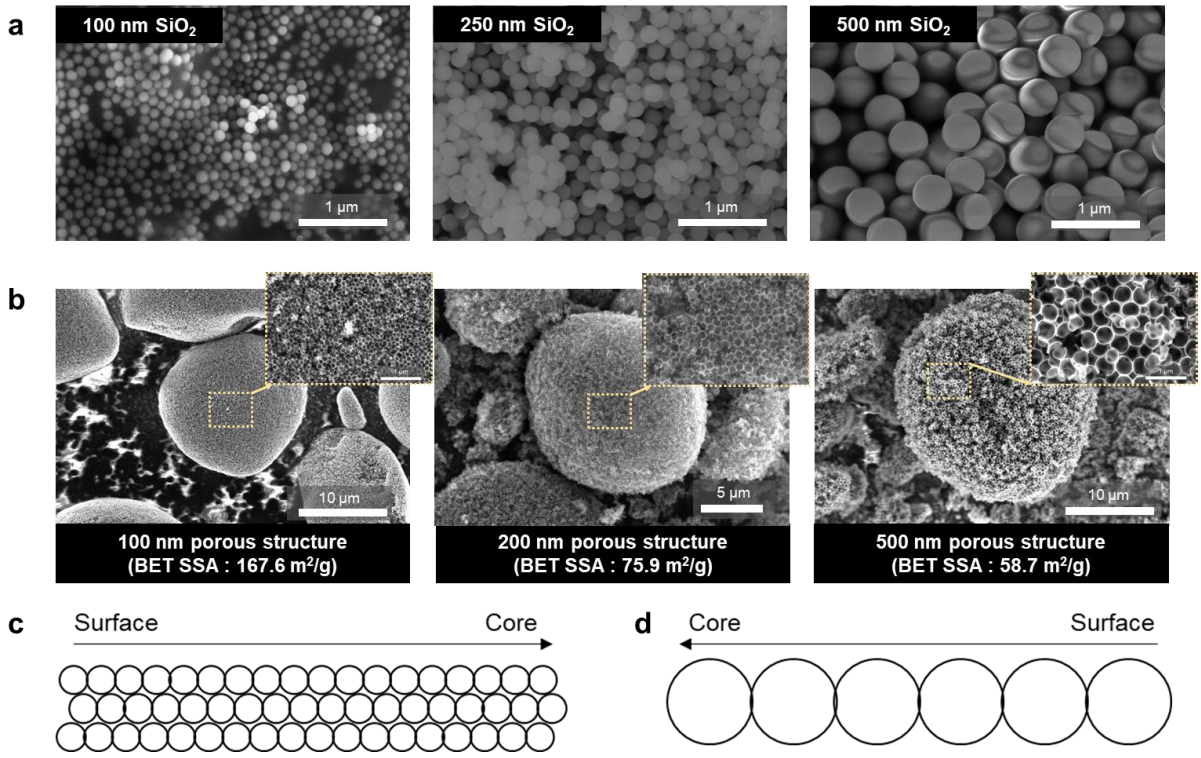

Figure 3-12. (a) SiO_2 nanoparticles synthesized in different diameter with 100, 250, and 500 nm and (b) porous carbon structure (PC) being fabricated with various diameter SiO_2 constructing the pore space by the etching process, diffusion pathway of (c) small-sized (100 nm) and (d) large-sized (500 nm) pore structure.

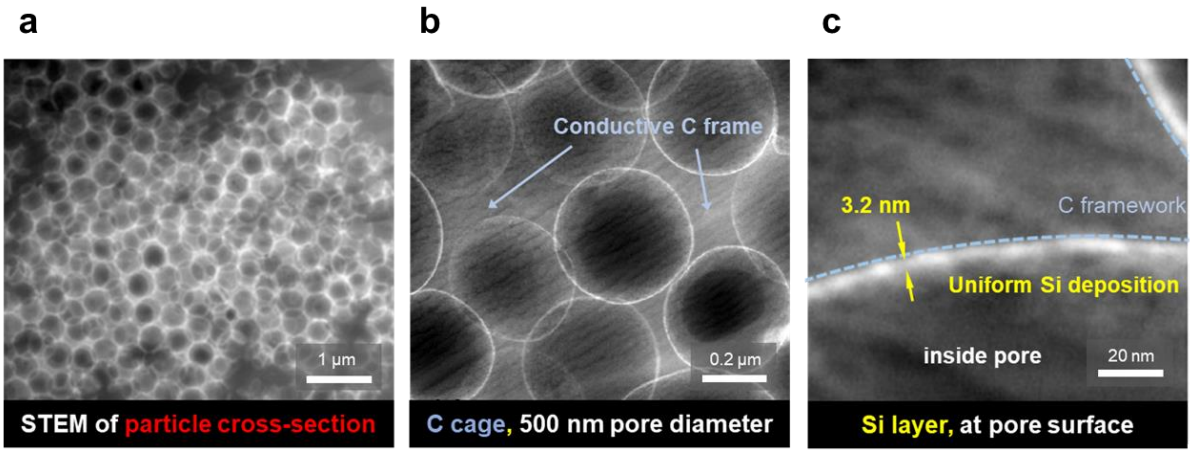

Figure 3-13. STEM cross-sectional images of (a) low magnification, (b) high magnification with structural constituents, and (c) uniform Si layer deposited PC on the inner surface of the pore.

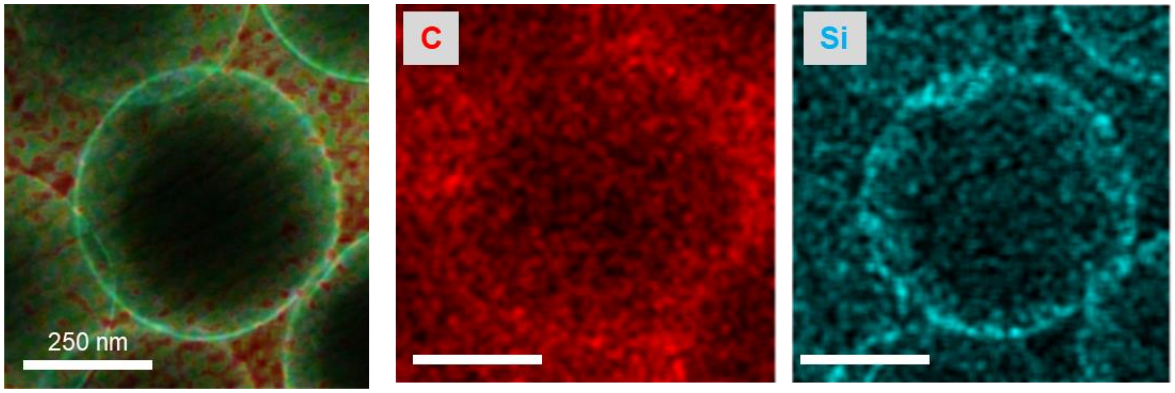

Figure 3-14. TEM-EDS mapping of the PC-S for the Si and C elements.

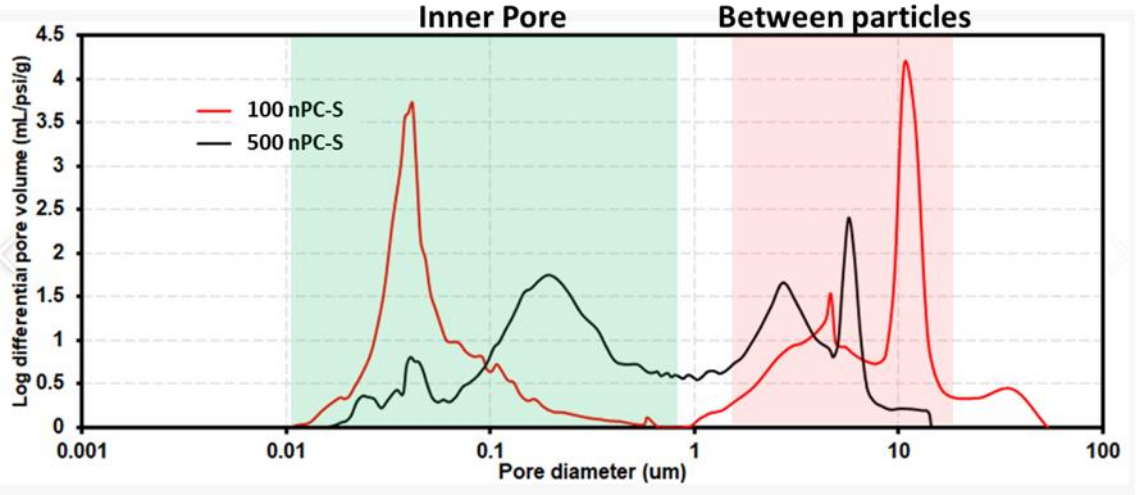

Figure 3-15. Mercury porosimetry analysis about the porosity and pore diameter distribution for the 100 nm and 500 nm PC-S applied electrodes.

Table 3-1. The results of porous structure by mercury porosimetry and BET surface area

	100nPC-S	**500nPC-S**
Porosity (%)	76.7	70.5
Average pore diameter(nm)	83	248
BET surface area (m^2/g)	167.6	58.7

Table 3-2. Electrodes specification for electrochemical characterization.

Electrode composition	≥ 85wt%
Loading level (mg cm^{-2})	1.2
Electrode density (g cm^{-3})	0.26
Electrolyte	DOL/DME(1/1), 1M LiTFSI, 5 wt% $LiNO_3$

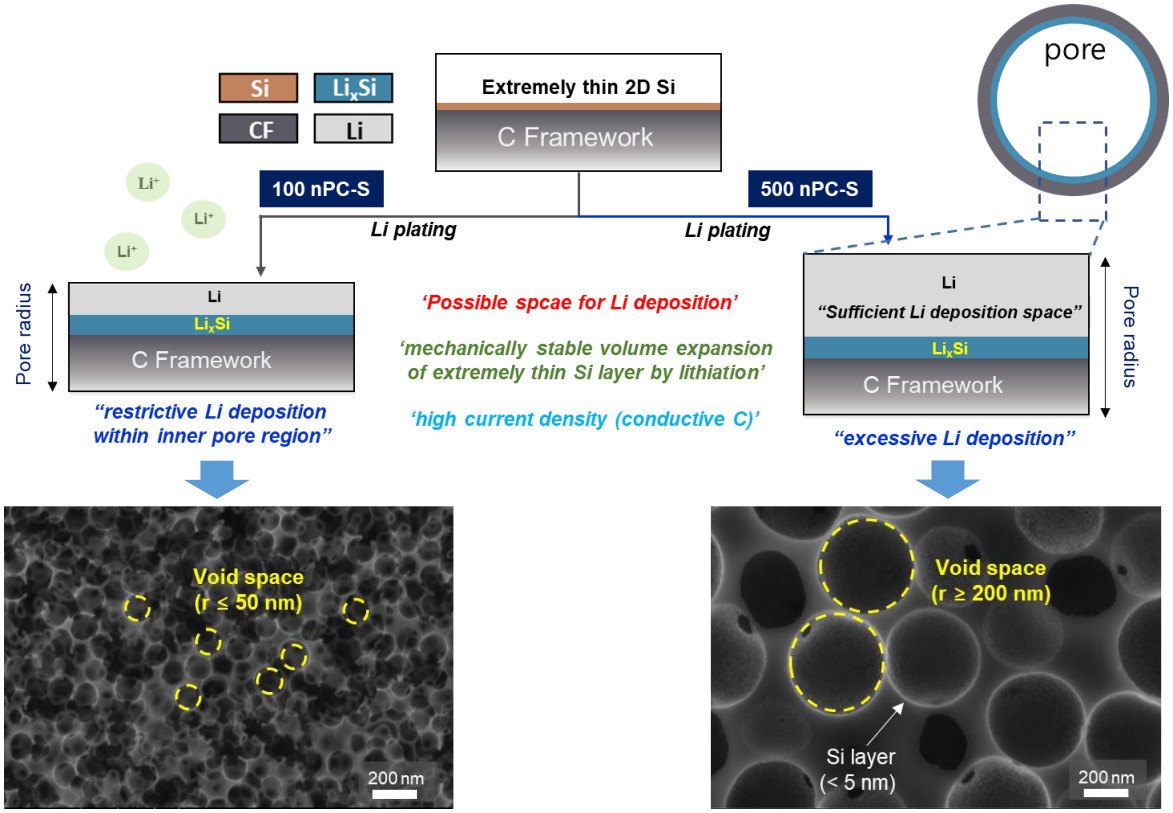

Figure 3-16. Schematic description for the advantages of increased pore diameter in terms of Li plating volume within the pore.

Li plating behaviors on the diverse lithiophilicity surface characteristics

For the different samples, lithiation reaction was conducted. Figure 3-17a shows the cross-sectional image of the electrode produced using 100 PC-S. Each PC is distributed as micro-particle, and the thickness of the electrode was 42 μm, which is much thinner than that of commercially utilized graphite electrode. This allows for greater energy density at the same areal capacity. For this electrode, when charging to 3 mAh cm^{-2}, the thickness of the electrode increased to 64 μm (Figure 3-17b). This means an electrode expansion was about 50%, and detailed changes are presented in Figure 3-17c and d. On the surface of each particle, a new material with thickness of 2 μm is deposited, and the inner region of the particle is generally empty. This result indicates the mass transfer of Li to the inner pore is not accessible. The electrochemical evaluation of 100 PC-S shows that the profile due to the lithiation of Si is observed, but the Li plating is not appeared as planned. Most of the Li did not deposit on the surface of inner pore, while substantial Li was deposited on the outmost of the PC particles. The deposited layer would be the plated Li and SEI layers. This will result in electrode expansion while widening the distance between particles by the thick outer layer. In order to improve the impregnation property of the electrolyte into the inner part of the particles, cell preparation was attempted under vacuum conditions. Figure 3-18 shows the results. After the initial lithiation, the results of the cross-section analysis confirmed that both partially filled inner pores and pores still present as empty spaces were observed. The electrolyte migration is essential to successfully increase the plated Li at the inner pore. However, Si expands during the lithiation process is expected, which interferes with the straightforward mass transfer by generating an effect of blocking the passage to the inner space. Li should be diffused from the surface region to the inner space by ionic diffusion through the active materials, which is unfavorable than direct contact of Li ion by mass transfer. Li accumulation on the surface would be ascribed by this obstacle to be diffused.

In contrast, Figure 3-19 exhibits the initial lithiation results of the 500 PC-S applied electrode. Figure 3-19a also shows the cross-sectional image of bare 500 PC-S, and the thickness of the electrode was 46 μm, which is similar to that of 100 PC-S applied electrode. The boundaries of the particles are not clear, which is thought to be due to the lack of structural stability compared to the dense cluster of 100 PC-S described above (**Strategy of lithiophilic layered conductive porous carbon structure for Li storage materials**). Nevertheless, the fundamental particle morphology appeared as it is. The cross section of the lithiated electrode with the same areal capacity (3 mAh cm^{-2}) is presented in Figure 3-19b. First, the thickness change of the electrode was reduced to about 10%, which is relatively low comparing to that of 100 PC-S. Compared with the results of 100 PC-S, no dark layer appeared on the border of each particles, and the void space distributed between the particles was reduced. Properly grown Li on the particle surface would be the result of adequately filling these voids. For a more precise analysis of this,

were we observed the inside pores (Figure 3-19c and d). Figure 3-19c demonstrates the completely filled pores with plated Li. In contrast, Figure 3-19d shows some pores still empty state, indicating that additional Li deposition space would be possible. Therefore, the 46 μm thick electrode will be able to accommodate the plated Li of areal capacity higher than 3 mAh cm^{-2}. In addition, to compare the effect of the Si layer, the results for 500 PC without Si deposition were also presented (Figure 3-20). First of all, the most prominent feature is that the electrode is detached from the current collector (Figure 3-20a and b). During the plating process of Li, the copper current collector with a higher lithiophilicity than the porous carbon structure provides a preferential Li plating area, and the metallic Li begins to grow from the interface between the active material and the current collector. Second, the Li and SEI layer deposited on the surface also appeared as in 100 PC-S (Figure 3-20c). The preference of Li deposition is improved on the surface where the SEI is formed, and the uniformity of this layer is poor comparing to that of 100 PC-S. Third, Li deposited on some inner pores was found, and it was found that the morphology is related to the appearance of dendrite. The open porous structure made it possible to transfer Li smoothly to the inside, which showed a difference in plating uniformity in contrast with the 500 PC-S with lithiophilic Si layer. This is the result showing the role of the lithiophilic Si layer.

Li dendrite investigation at the electrode surface

To investigate the effect of rational Li deposition within the inner pore region, we confirmed the top-view of the lithiated electrode using SEM (Figure 3-21). The thickness and loading of the electrode were adjusted and fabricated with similar specification, and the state of the surface was analyzed after charging with the same areal capacity (3 mAh cm^{-2}). Li dendrite was most frequently found on the surface of the 100 PC-S applied electrode. In the lithiation process, 100 PC-S with a lithiophilic Si surface layer preferentially deposited the reduced Li on the surface of particles, forming thick Li containing layer for all particles (Figure 3-17). Nevertheless, the excess Li was deposited on the surface of the electrode, plating the Li dendrite. In contrast, Li dendrite was not found on the surface of the electrode to which 500 PC-S particles were applied. If the deposition of Li is done within the pores, dendritic Li will be difficult to deposit on the electrode surface before the areal capacity exceeding the critical point. As shown in Figure 3-19d, the results of this study are quite reasonable, in which dendrite did not grow from the areal capacity of 3 mAh cm^{-2}, because there still is remaining space for deposition. In addition, the surface of each particles in the electrode exhibits spherical shapes distributed overall the particles. The deposition of Li into the pores of 500 nm size with the spherical shape is seen on the SEM image. In the case of 500 PC, the Li dendrite was occasionally found comparing to 500 PC-S, but it was significantly less than 100 PC-S. Because the deposition of Li is preferred on the surface of the copper current collector due to its higher lithiophilicity.

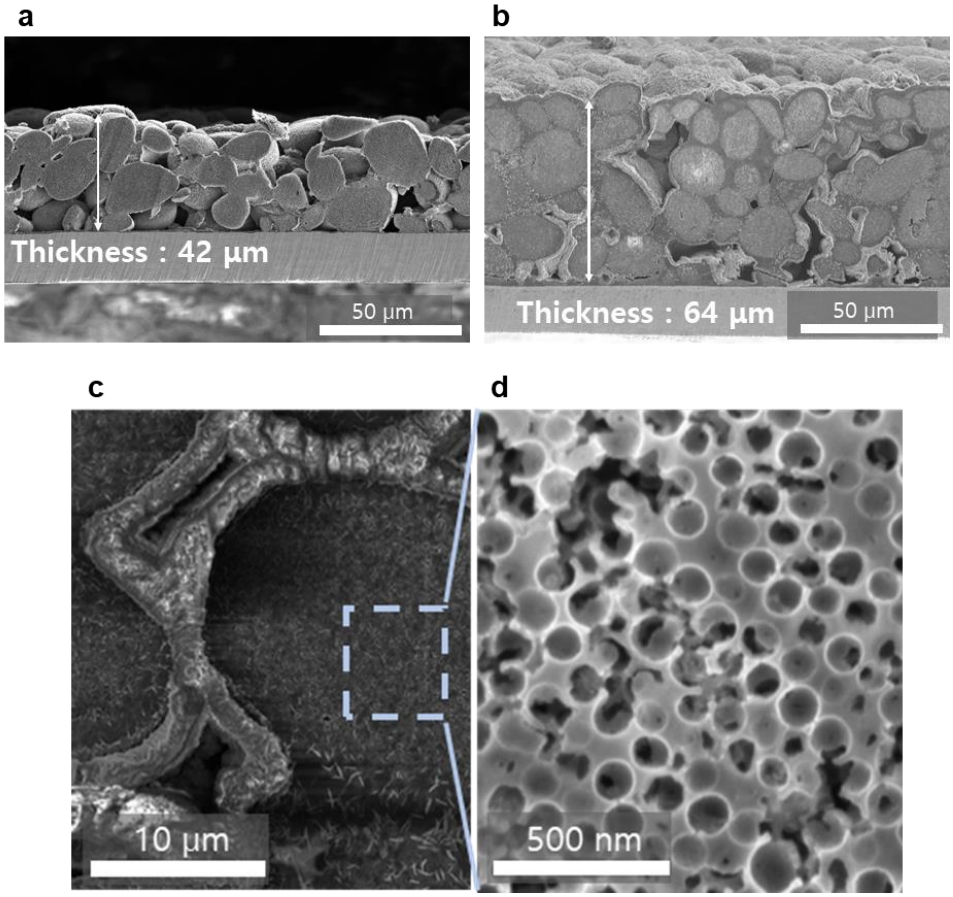

Figure 3-17. Cross-sectional SEM image of (a) bare electrode with 100 PC-S, (b) lithiated 100 PC-S of 3 mAh cm^{-2}, (c) lithiated particles with high magnification, and (d) inner pore region of lithiated particles.

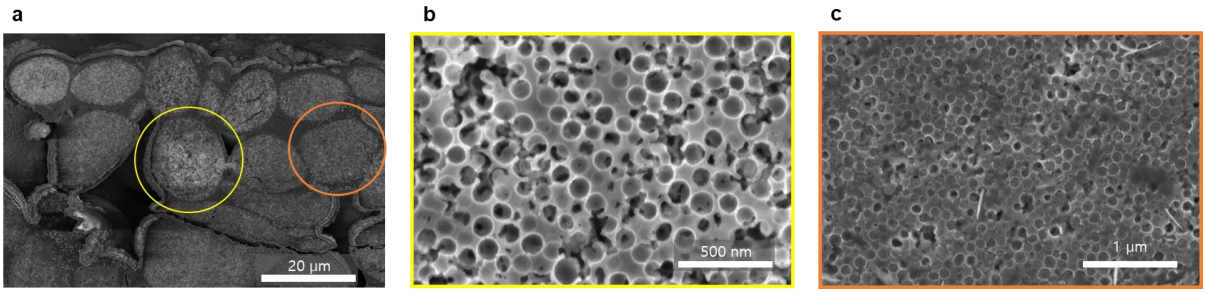

Figure 3-18. Cross-sectional SEM image of (a) lithiated electrode with 100 PC-S of 3 mAh cm^{-2}, (b) inner pore region of not totally filled (lithiated) particles, and (c) inner pore region of partially filled particles.

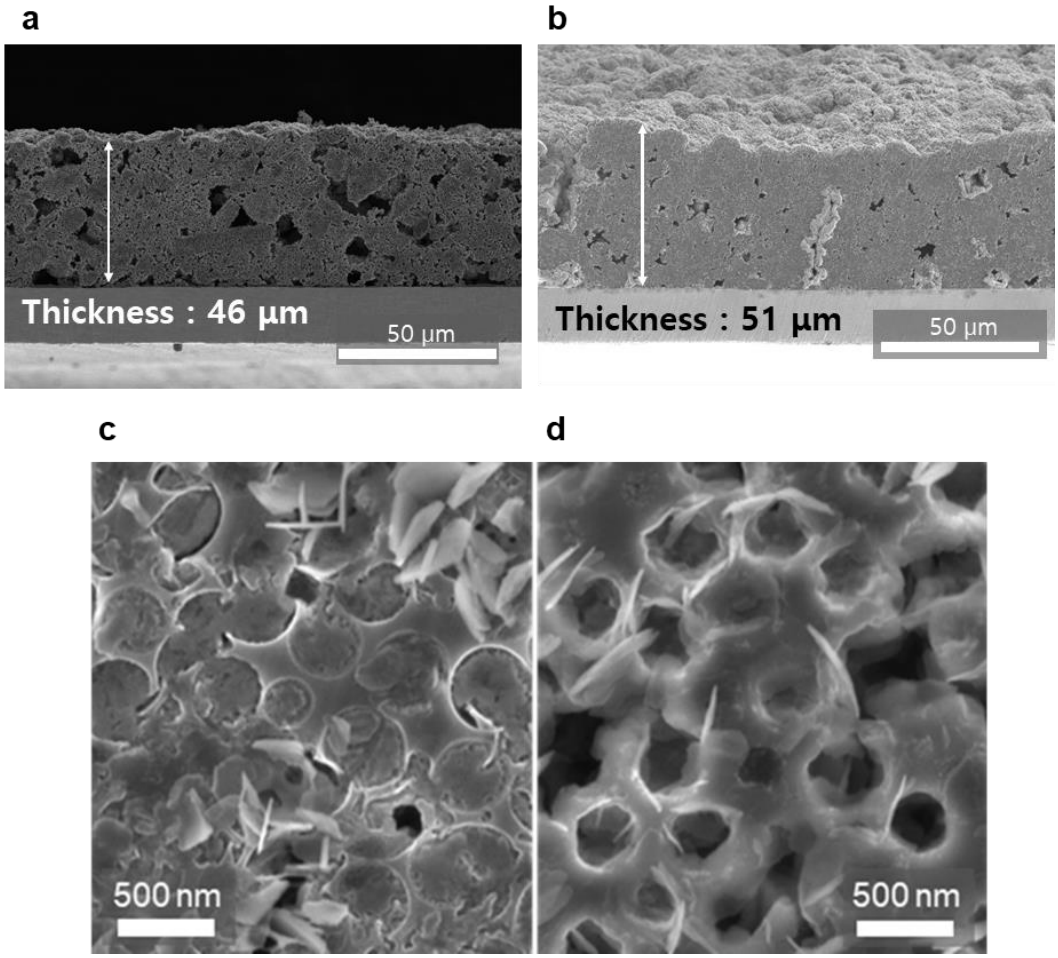

Figure 3-19. Cross-sectional SEM image of (a) bare electrode with 500 PC-S, (b) lithiated 500 PC-S of 3 mAh cm^{-2}, (c) inner pore region of totally filled state, and (d) inner pore region of partially filled state particles.

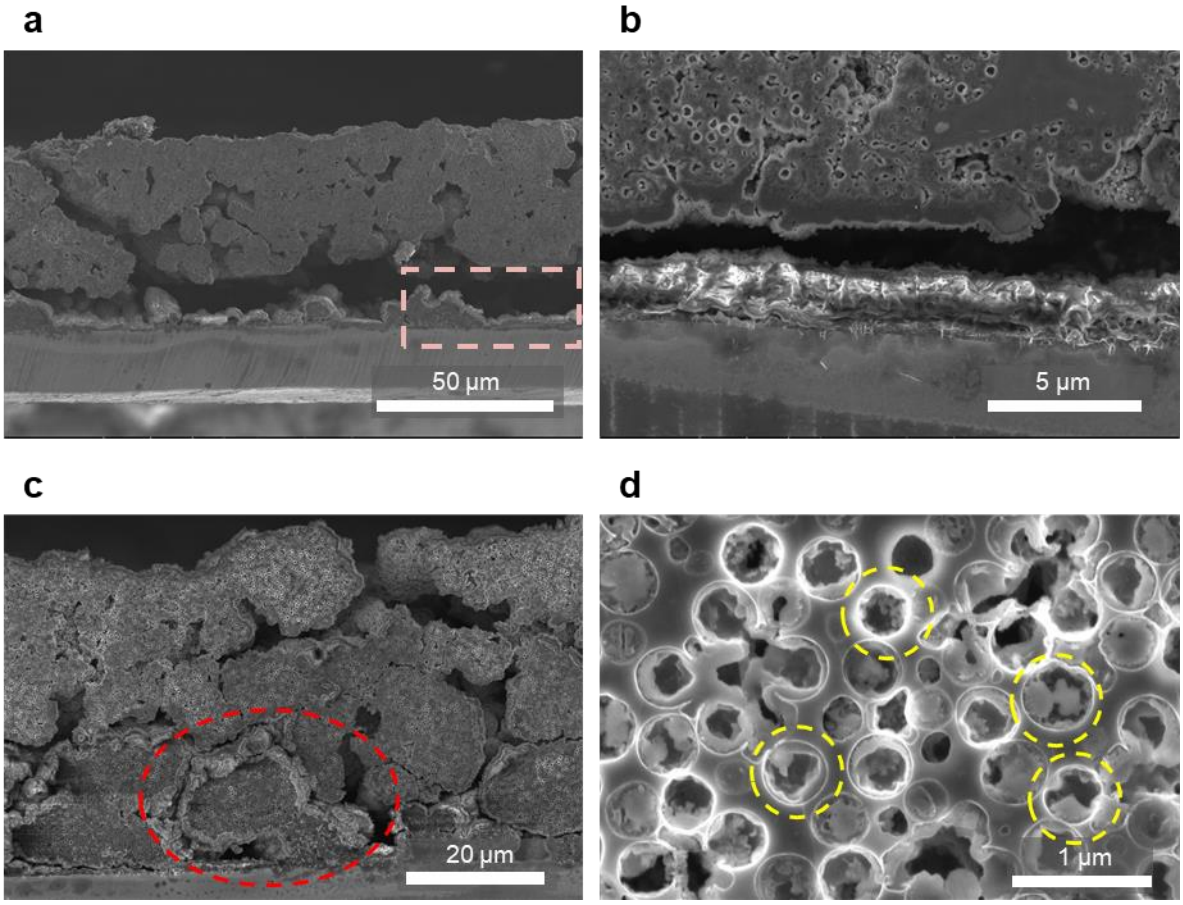

Figure 3-20. Cross-sectional SEM image of (a) lithiated 500 PC of 3 mAh cm^{-2}, (b) the region around the current collector where the Li plated, (c) particle with Li accumulation at surface, and (d) inner pore region of partially filled with Li dendrite.

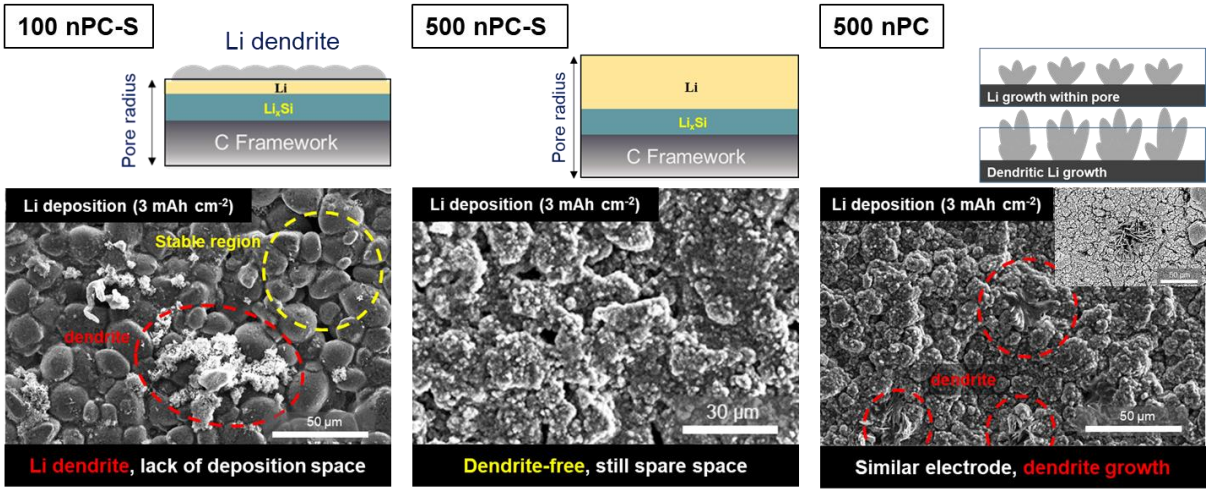

Figure 3-21. Top-view images of (a) 100 PC-S, (b) 500 PC-S, and (c) 500 PC after lithiation with 3 mAh cm^{-2}.

Simulation verification with molecular dynamics (MD): Dimensional effect of applied Si

To study the morphological effects of lithiophilic additive, we implemented molecular dynamics (MD) simulations via ReaxFF (reactive force field). Large number of studies related to previously reported lithiophilic materials utilized nano-sized seeds within the closed systems.[136,146] Synthesis of seed materials with nano-sized particle is not favorable procedure and forming them where necessary would be also difficult. Moreover, to fit the required size and dimension should be also ambitious. The results of the uniform lithiphilic layer with a thickness of several nanometers have not been reported. Furthermore, the attempts to reveal the effect of morphological characteristics of lithiophilic assistant, based on the calculation method, are still not reported. This could also be supported experimentally. Figure 3-22 shows the image of particle introduced with different dimensional Si by the schematic diagram and SEM cross-sectional image (Figure 3-22a and b).

Based on this, we presented a simple system by the schematic description for the 1D and 2D lithiophilic assistant dispersed PC surface, respectively (Figure 3-22c and d). 1D type additive will activate the Li plating at the surface along the shape as in the Figure 3-22c. In contrast, the 2D lithiophilic assistant has a structural advantage that Li grows evenly across the exposed surface coated by Si. The effect of surface roughness about the growth of Li is demonstrated using simulation tools, and then we confirmed it with the experimental verification. The results of this experiment are presented in Figure 3-23. Figure 3-23a shows the cross-sectional image after lithiation for 500 PC-S with dot type 1D Si seed assistant, and figure 3-23b shows the cross-sectional image for 500 PC-S with flat plane type 2D Si layer. In the case of seed type Si, it was deviated from the surface of PC, and the plated Li grew from the seed itself. The morphology of the grown Li is also non-uniform and grainy from the C frame surface. On the other hand, densely filled Li from the C surface was confirmed by Figure 3-23b where the inner pores were almost filled. The separation of Si layer at the surface of C structure did not occur. During the synthesis of layered Si, the large contact area of Si with the C surface could improve the binding properties between Si and C.

The simulation was performed at room temperature and the diffusion of Li was achieved by the applied electric fields with different intensities (0.001, 0.01, 0.1, 1 V/Å) in the Z-axis direction. As a test study, a system in which EC/DEC electrolyte was mixed was used, and as shown in figure 3-24, Li deposition properties are shown. In the Si layer, a dense distribution of Li atoms was exhibited at the Li_xSi layer due to the alloying reaction of Si with Li. The grown Li at the surface of Li_xSi was deposited by an electric field, and the plated Li was mixed with additives (EC and DEC). To investigate the growth model, the calculation was performed using the Convex hull algorithm. The obtained results are presented in Figure 3-25. The initially formed Li is growing with a flat surface shape until 50 ps. The Li morphology extremely changed by the additional Li deposition. The results demonstrates the critical

point to be observed for uniform Li deposition. Furthermore, we can probe the necessary parameters of lithiophilic Si for rational Li plating based on the simulation results. The Li density plot elucidates the Li distribution of plated Li at the C surface, and as in MD simulation, the most Li is distributed in the Si layer. The Li dispersion density is highest in the vicinity of Li_xSi layer, and the density tends to decrease as getting away from the Li_xSi layer. The high density at the top layer is fundamental result of being adjacent to the Li source.

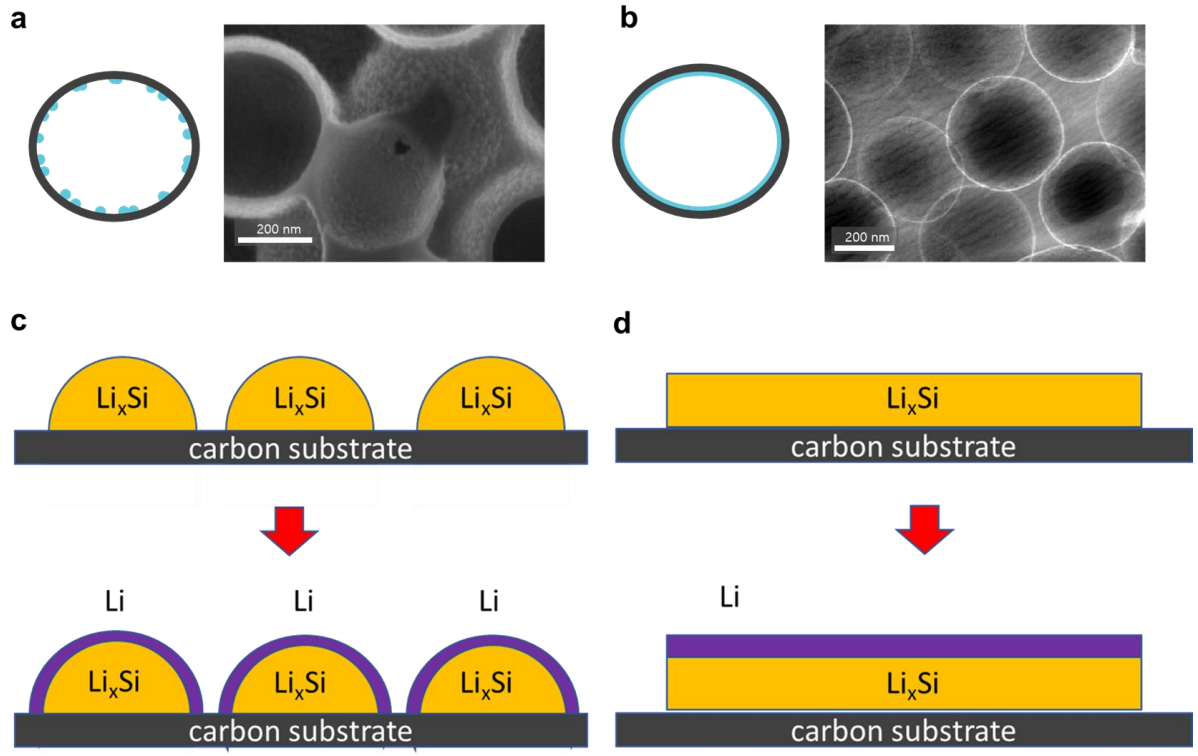

Figure 3-22. Schematic diagram and SEM image of (a) 1D Si dot introduced pore region, (b) 2D Si layered pore region, and schematic illustration of plated Li according to the surface of (c) dot type, and (d) flat plane type of Li_xSi.

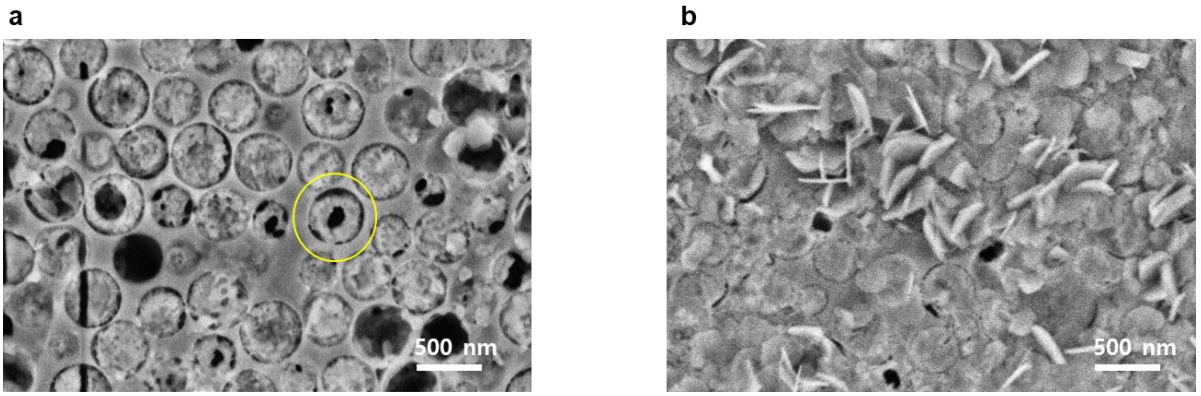

Figure 3-23. Cross-sectional SEM image of (a) 1D Si dot, and (b) 2D Si plane introduced C structure after lithiation with areal capacity of 3 mAh cm^{-2}.

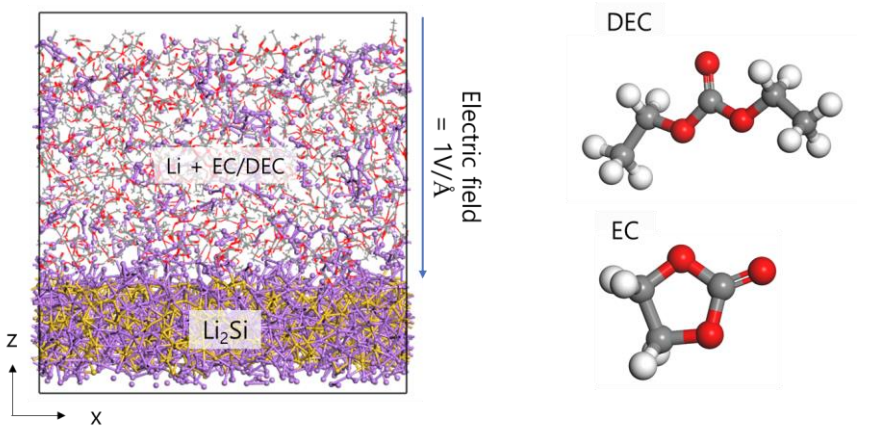

Figure 3-24. ReaxFF reactive MD simulation of lithiated Si (Li_2Si) and plated Li with EC/DEC additive.

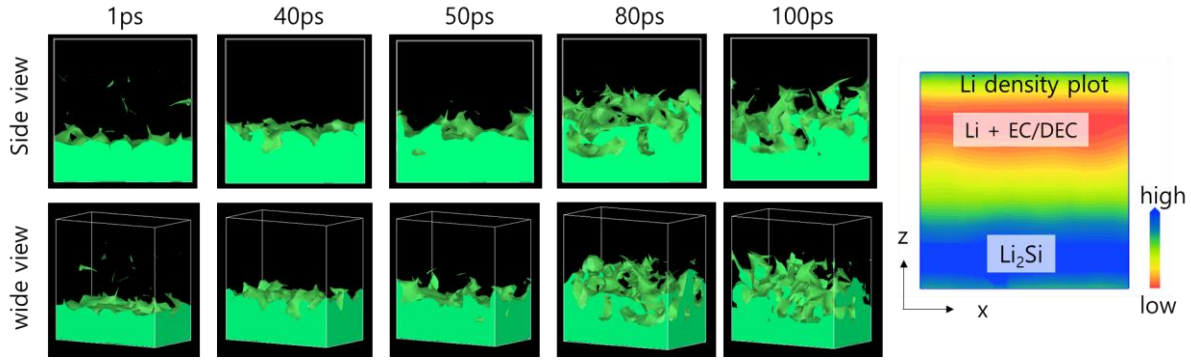

Figure 3-25. Principles of Li_xSi and plated Li formation at the surface region by convex hull algorithm and corresponding Li density plot to Z axis.

3.4 Conclusion

In summary, an effective Li hosting PC-S design, consisting of the open porous conductive carbon structure and the outermost Si covering with extremely thin layer, was prepared *via* a simple and mass production process to realize practical possibility as a next generation Li metal anode. We demonstrated that the well-defined open and macro porous structure containing ultrathin 2D Si coating layer less than 5 nm of relatively small Si content can provide sufficient space to store the plated Li even after the lithiation of Si and its volume expansion. Moreover, the outermost lithiophilic Si layer can effectively induce the accumulation of the reduced Li with flat and dense state on the inner pore region. With this unique material design, the energy density of this material exhibits relatively higher value comparing to previous reported results. And the electrochemical performance of both symmetric cell and full cell were evaluated under industrial areal capacity loading of cathode (≥ 3.4 mAh cm^{-2}). The bare electrode density introducing the PC-S was ~0.2 g cm^{-3} with the electrode thickness of 40~45 μm. In the half cell result, the open porous and Si layered PC-S showed superior cycling CE and cycle stability without operation voltage change. This multifunctional Si/C design achieved remarkable advance in Li metal battery energy density and practical viability compared with previous reported papers.

References

1 An, Y. et al. Green, Scalable, and Controllable Fabrication of Nanoporous Silicon from Commercial Alloy Precursors for High-Energy Lithium-Ion Batteries. ACS Nano, doi:10.1021/acsnano.8b02219 (2018).

2 Liu, Y. et al. An All-Integrated Anode via Interlinked Chemical Bonding between Double-Shelled-Yolk-Structured Silicon and Binder for Lithium-Ion Batteries. Adv Mater 29, doi:10.1002/adma.201703028 (2017).

3 Ma, Y. et al. Constraining Si Particles within Graphene Foam Monolith: Interfacial Modification for High-Performance Li+Storage and Flexible Integrated Configuration. Advanced Functional Materials 26, 6797-6806, doi:10.1002/adfm.201602324 (2016).

4 Park, H. et al. Design of an ultra-durable silicon-based battery anode material with exceptional high-temperature cycling stability. Nano Energy 26, 192-199, doi:10.1016/j.nanoen.2016.05.030 (2016).

5 Zhang, X., Guo, R., Li, X. & Zhi, L. Scallop-Inspired Shell Engineering of Microparticles for Stable and High Volumetric Capacity Battery Anodes. Small, e1800752, doi:10.1002/smll.201800752 (2018).

6 Yu, L., Wu, H. B. & Lou, X. W. Mesoporous Li(4)Ti(5)O(1)(2) hollow spheres with enhanced lithium storage capability. Adv Mater 25, 2296-2300, doi:10.1002/adma.201204912 (2013).

7 He, Y. B. et al. Gassing in Li(4)Ti(5)O(12)-based batteries and its remedy. Sci Rep 2, 913, doi:10.1038/srep00913 (2012).

8 Lee, J.-H., Kim, W.-J., Kim, J.-Y., Lim, S.-H. & Lee, S.-M. Spherical silicon/graphite/carbon composites as anode material for lithium-ion batteries. Journal of Power Sources 176, 353-358, doi:10.1016/j.jpowsour.2007.09.119 (2008).

9 Oumellal, Y., Rougier, A., Nazri, G. A., Tarascon, J. M. & Aymard, L. Metal hydrides for lithium-ion batteries. Nat Mater 7, 916-921, doi:10.1038/nmat2288 (2008).

10 Yang, Z. et al. Nanostructures and lithium electrochemical reactivity of lithium titanites and titanium oxides: A review. Journal of Power Sources 192, 588-598, doi:10.1016/j.jpowsour.2009.02.038 (2009).

11 Lee, H., Yanilmaz, M., Toprakci, O., Fu, K. & Zhang, X. A review of recent developments in

membrane separators for rechargeable lithium-ion batteries. Energy Environ. Sci. 7, 3857-3886, doi:10.1039/c4ee01432d (2014).

12 Alias, N. & Mohamad, A. A. Advances of aqueous rechargeable lithium-ion battery: A review. Journal of Power Sources 274, 237-251, doi:10.1016/j.jpowsour.2014.10.009 (2015).

13 Hannan, M. A., Lipu, M. S. H., Hussain, A. & Mohamed, A. A review of lithium-ion battery state of charge estimation and management system in electric vehicle applications: Challenges and recommendations. Renewable and Sustainable Energy Reviews 78, 834-854, doi:10.1016/j.rser.2017.05.001 (2017).

14 Fan, E. et al. Sustainable Recycling Technology for Li-Ion Batteries and Beyond: Challenges and Future Prospects. Chemical Reviews, doi:10.1021/acs.chemrev.9b00535 (2020).

15 Richa, K., Babbitt, C. W., Nenadic, N. G. & Gaustad, G. Environmental trade-offs across cascading lithium-ion battery life cycles. The International Journal of Life Cycle Assessment 22, 66-81, doi:10.1007/s11367-015-0942-3 (2015).

16 Qian, K., Zhou, C., Allan, M. & Yuan, Y. Modeling of Load Demand Due to EV Battery Charging in Distribution Systems. IEEE Transactions on Power Systems 26, 802-810, doi:10.1109/tpwrs.2010.2057456 (2011).

17 Dai, H., Wei, X., Sun, Z., Wang, J. & Gu, W. Online cell SOC estimation of Li-ion battery packs using a dual time-scale Kalman filtering for EV applications. Applied Energy 95, 227-237, doi:10.1016/j.apenergy.2012.02.044 (2012).

18 Han, X., Ouyang, M., Lu, L. & Li, J. A comparative study of commercial lithium ion battery cycle life in electric vehicle: Capacity loss estimation. Journal of Power Sources 268, 658-669, doi:10.1016/j.jpowsour.2014.06.111 (2014).

19 Bhatt, M. D. & O'Dwyer, C. Recent progress in theoretical and computational investigations of Li-ion battery materials and electrolytes. Phys Chem Chem Phys 17, 4799-4844, doi:10.1039/c4cp05552g (2015).

20 Gu, M., He, Y., Zheng, J. & Wang, C. Nanoscale silicon as anode for Li-ion batteries: The fundamentals, promises, and challenges. Nano Energy 17, 366-383, doi:10.1016/j.nanoen.2015.08.025 (2015).

21 Wang, L. et al. Li-free Cathode Materials for High Energy Density Lithium Batteries. Joule, doi:10.1016/j.joule.2019.07.011 (2019).

22 Wang, B. et al. Ultrafast-Charging Silicon-Based Coral-Like Network Anodes for Lithium-Ion Batteries with High Energy and Power Densities. ACS Nano, doi:10.1021/acsnano.8b09034 (2019).

23 Shin, J., Kim, T.-H., Lee, Y. & Cho, E. Key functional groups defining the formation of Si anode solid-electrolyte interphase towards high energy density Li-ion batteries. Energy Storage Materials, doi:10.1016/j.ensm.2019.09.009 (2019).

24 Fan, Y., Chen, X., Legut, D. & Zhang, Q. Modeling and theoretical design of next-generation lithium metal batteries. Energy Storage Materials 16, 169-193, doi:10.1016/j.ensm.2018.05.007 (2019).

25 Fang, C. et al. Quantifying inactive lithium in lithium metal batteries. Nature 572, 511-515, doi:10.1038/s41586-019-1481-z (2019).

26 J.-M. Tarascon, Issues and challenges facing rechargeable lithium batteries. Nature 414, 359–367 (2001).

27 Zhang, L. et al. Advanced Matrixes for Binder-Free Nanostructured Electrodes in Lithium-Ion Batteries. Adv Mater, e1908445, doi:10.1002/adma.201908445 (2020).

28 Wu, F., Maier, J. & Yu, Y. Guidelines and trends for next-generation rechargeable lithium and lithium-ion batteries. Chem Soc Rev, doi:10.1039/c7cs00863e (2020).

29 Schmuch, R., Wagner, R., Hörpel, G., Placke, T. & Winter, M. Performance and cost of materials for lithium-based rechargeable automotive batteries. Nature Energy 3, 267-278, doi:10.1038/s41560-018-0107-2 (2018).

30 Subramanian Natarajan and Vanchiappan Aravindan, Burgeoning Prospects of Spent Lithium-Ion Batteries in Multifarious Applications, Adv. Energy Mater. (2018), 1802303

31 Yan, P.; Zheng, J.; Liu, J.; Wang, B.; Cheng, X.; Zhang, Y.; Sun, X.; Wang, C.; Zhang, J.-G., Tailoring grain boundary structures and chemistry of Ni-rich layered cathodes for enhanced cycle stability of lithium-ion batteries. Nat. Energy 2018.

32 Assat, G.; Tarascon, J.-M., Fundamental understanding and practical challenges of anionic redox activity in Li-ion batteries. Nat. Energy 2018.

33 Singer, A.; Zhang, M.; Hy, S.; Cela, D.; Fang, C.; Wynn, T. A.; Qiu, B.; Xia, Y.; Liu, Z.; Ulvestad, A.; Hua, N.; Wingert, J.; Liu, H.; Sprung, M.; Zozulya, A. V.; Maxey, E.; Harder, R.; Meng, Y. S.; Shpyrko, O. G., Nucleation of dislocations and their

dynamics in layered oxide cathode materials during battery charging. Nat. Energy 2018.

34 Goriparti, S. et al. Review on recent progress of nanostructured anode materials for Li-ion batteries. Journal of Power Sources 257, 421-443, doi:10.1016/j.jpowsour.2013.11.103 (2014).

35 Chen, T., Wu, J., Zhang, Q. & Su, X. Recent advancement of SiO x based anodes for lithium-ion batteries. Journal of Power Sources 363, 126-144, doi:10.1016/j.jpowsour.2017.07.073 (2017).

36 Palacin, M. R. Recent advances in rechargeable battery materials: a chemist's perspective. Chem Soc Rev 38, 2565-2575, doi:10.1039/b820555h (2009).

37 Hu, R. et al. Stabilizing the Nanostructure of SnO2 Anodes by Transition Metals: A Route to Achieve High Initial Coulombic Efficiency and Stable Capacities for Lithium Storage. Adv Mater 29, doi:10.1002/adma.201605006 (2017).

38 Zhang, J. et al. Na-Mn-O Nanocrystals as a High Capacity and Long Life Anode Material for Li-Ion Batteries. Advanced Energy Materials 7, doi:10.1002/aenm.201602092 (2017).

39 McDowell, M. T., Woo Lee, S., Wang, C. & Cui, Y. The effect of metallic coatings and crystallinity on the volume expansion of silicon during electrochemical lithiation/delithiation. Nano Energy 1, 401-410, doi:10.1016/j.nanoen.2012.03.004 (2012).

40 Han, C. et al. A review of gassing behavior in Li4Ti5O12-based lithium ion batteries. Journal of Materials Chemistry A 5, 6368-6381, doi:10.1039/c7ta00303j (2017).

41 Placke, T., Kloepsch, R., Dühnen, S. & Winter, M. Lithium ion, lithium metal, and alternative rechargeable battery technologies: the odyssey for high energy density. Journal of Solid State Electrochemistry 21, 1939-1964, doi:10.1007/s10008-017-3610-7 (2017).

42 Magasinski, A. et al. High-performance lithium-ion anodes using a hierarchical bottom-up approach. Nat Mater 9, 353-358, doi:10.1038/nmat2725 (2010).

43 Su, L., Zhou, Z. & Ren, M. Core double-shell Si@SiO2@C nanocomposites as anode materials for Li-ion batteries. Chem Commun (Camb) 46, 2590-2592, doi:10.1039/b925696b (2010).

44 Yao, Y. et al. Interconnected silicon hollow nanospheres for lithium-ion battery anodes with long cycle life. Nano Lett 11, 2949-2954, doi:10.1021/nl201470j (2011).

45 Xu, W. et al. Lithium metal anodes for rechargeable batteries. Energy Environ. Sci. 7, 513-537, doi:10.1039/c3ee40795k (2014).

46 Zhang, Y. et al. Dendrite-free lithium deposition with self-aligned nanorod structure. Nano Lett 14, 6889-6896, doi:10.1021/nl5039117 (2014).

47 Yu, C. et al. Silicon Carbide as a Protective Layer to Stabilize Si-Based Anodes by Inhibiting Chemical Reactions. Nano Lett, doi:10.1021/acs.nanolett.9b01492 (2019).

48 Son, Y. et al. Exploring Critical Factors Affecting Strain Distribution in 1D Silicon-Based Nanostructures for Lithium-Ion Battery Anodes. Advanced Materials, doi:10.1002/adma.201705430 (2018).

49 Nie, P. et al. Graphene Caging Silicon Particles for High-Performance Lithium-Ion Batteries. Small 14, e1800635, doi:10.1002/smll.201800635 (2018).

50 Zhuang, J. et al. Silicene: A Promising Anode for Lithium-Ion Batteries. Adv Mater 29, doi:10.1002/adma.201606716 (2017).

51 Kwon, T. W., Choi, J. W. & Coskun, A. The emerging era of supramolecular polymeric binders in silicon anodes. Chem Soc Rev, doi:10.1039/c7cs00858a (2018).

52 Chae, S., Ko, M., Kim, K., Ahn, K. & Cho, J. Confronting Issues of the Practical Implementation of Si Anode in High-Energy Lithium-Ion Batteries. Joule 1, 47-60, doi:10.1016/j.joule.2017.07.006 (2017).

53 Li, X. et al. Mesoporous silicon sponge as an anti-pulverization structure for high-performance lithium-ion battery anodes. Nat Commun 5, 4105, doi:10.1038/ncomms5105 (2014).

54 Zhu, B. et al. Scalable Production of Si Nanoparticles Directly from Low Grade Sources for Lithium-Ion Battery Anode. Nano Lett 15, 5750-5754, doi:10.1021/acs.nanolett.5b01698 (2015).

55 Kimura, K. et al. Improvement of Cyclability of Li-Ion Batteries Using C-Coated Si Nanopowder Electrode Fabricated from Si Swarf with Limitation of Delithiation Capacity. Journal of The Electrochemical Society 164, A995-A1001, doi:10.1149/2.0361706jes (2017).

56 Wang, J., Cui, Y. & Wang, D. Design of Hollow Nanostructures for Energy Storage, Conversion and Production. Adv Mater, e1801993, doi:10.1002/adma.201801993 (2018).

57 Zhu, G. L. et al. Fast Charging Lithium Batteries: Recent Progress and Future Prospects. Small, e1805389, doi:10.1002/smll.201805389 (2019).

58 Zhao, Y. et al. Stable Li Metal Anode by a Hybrid Lithium Polysulfidophosphate/Polymer Cross-Linking Film. ACS Energy Letters, 1271-1278, doi:10.1021/acsenergylett.9b00539

(2019).

59 Niu, C. et al. Self-smoothing anode for achieving high-energy lithium metal batteries under realistic conditions. Nat Nanotechnol, doi:10.1038/s41565-019-0427-9 (2019).

60 Lin, D., Liu, Y. & Cui, Y. Reviving the lithium metal anode for high-energy batteries. Nat Nanotechnol 12, 194-206, doi:10.1038/nnano.2017.16 (2017).

61 Wu, H. & Cui, Y. Designing nanostructured Si anodes for high energy lithium ion batteries. Nano Today 7, 414-429, doi:10.1016/j.nantod.2012.08.004 (2012).

62 Goodenough, J. B. & Kim, Y. Challenges for Rechargeable Li Batteries†. Chemistry of Materials 22, 587-603, doi:10.1021/cm901452z (2010).

63 Obrovac, M. N. & Chevrier, V. L. Alloy negative electrodes for Li-ion batteries. Chem Rev 114, 11444-11502, doi:10.1021/cr500207g (2014).

64 Li, M., Lu, J., Chen, Z. & Amine, K. 30 Years of Lithium-Ion Batteries. Adv Mater, e1800561, doi:10.1002/adma.201800561 (2018).

65 Ryu, J., Hong, D., Lee, H.-W. & Park, S. Practical considerations of Si-based anodes for lithium-ion battery applications. Nano Research 10, 3970-4002, doi:10.1007/s12274-017-1692-2 (2017).

66 Schmuch, R., Wagner, R., Hörpel, G., Placke, T. & Winter, M. Performance and cost of materials for lithium-based rechargeable automotive batteries. Nature Energy 3, 267-278, doi:10.1038/s41560-018-0107-2 (2018).

67 Choi, J. W. & Aurbach, D. Promise and reality of post-lithium-ion batteries with high energy densities. Nature Reviews Materials 1, doi:10.1038/natrevmats.2016.13 (2016).

68 Placke, T., Kloepsch, R., Dühnen, S. & Winter, M. Lithium ion, lithium metal, and alternative rechargeable battery technologies: the odyssey for high energy density. Journal of Solid State Electrochemistry 21, 1939-1964, doi:10.1007/s10008-017-3610-7 (2017).

69 Jian Y. H., Li Z., Chong M. W., John P. S.,1 Wu X., Li Q. Z., Scott X. M., Nicholas S. H., Xiao H. L., Arunkumar S., Hongyou F., Liang Q., Akihiro K., Ju L. In Situ Observation of the Electrochemical Lithiation of a Single SnO_2 Nanowire Electrode. Science 330, 1515-1520, 10.1126/science.1195628 (2010)

70 Li, S. et al. High-rate aluminium yolk-shell nanoparticle anode for Li-ion battery with long cycle life and ultrahigh capacity. Nat Commun 6, 7872, doi:10.1038/ncomms8872 (2015).

71 Hwang, G. et al. A high-performance nanoporous Si/Al2O3 foam lithium-ion battery anode fabricated by selective chemical etching of the Al-Si alloy and subsequent thermal oxidation. Chem Commun (Camb) 51, 4429-4432, doi:10.1039/c4cc09956g (2015).

72 Rehnlund, D. et al. Lithium trapping in alloy forming electrodes and current collectors for lithium based batteries. Energy & Environmental Science 10, 1350-1357, doi:10.1039/c7ee00244k (2017).

73 Son, Y. et al. Exploring Critical Factors Affecting Strain Distribution in 1D Silicon-Based Nanostructures for Lithium-Ion Battery Anodes. Advanced Materials, doi:10.1002/adma.201705430 (2018).

74 McDowell, M. T. et al. Studying the kinetics of crystalline silicon nanoparticle lithiation with in situ transmission electron microscopy. Adv Mater 24, 6034-6041, doi:10.1002/adma.201202744 (2012).

75 Tardif, S. et al. Operando Raman Spectroscopy and Synchrotron X-ray Diffraction of Lithiation/Delithiation in Silicon Nanoparticle Anodes. ACS Nano 11, 11306-11316, doi:10.1021/acsnano.7b05796 (2017).

76 Fang, S. et al. Rational design of void-involved Si@TiO_2 nanospheres as high-performance anode material for lithium-ion batteries. ACS Appl Mater Interfaces 6, 6497-6503, doi:10.1021/am500066j (2014).

77 Jing, S., Jiang, H., Hu, Y., Shen, J. & Li, C. Face-to-Face Contact and Open-Void Coinvolved Si/C Nanohybrids Lithium-Ion Battery Anodes with Extremely Long Cycle Life. Advanced Functional Materials 25, 5395-5401, doi:10.1002/adfm.201502330 (2015).

78 Liu, Q. et al. Surface Coating Constraint Induced Anisotropic Swelling of Silicon in Si-Void@SiO x Nanowire Anode for Lithium-Ion Batteries. Small 13, doi:10.1002/smll.201603754 (2017).

79 Wei Seh, Z. et al. Sulphur-TiO2 yolk-shell nanoarchitecture with internal void space for long-cycle lithium-sulphur batteries. Nat Commun 4, 1331, doi:10.1038/ncomms2327 (2013).

80 Han, Y. et al. Si@void@C Nanofibers Fabricated Using a Self-Powered Electrospinning System for Lithium-Ion Batteries. ACS Nano, doi:10.1021/acsnano.8b01558 (2018).

81 Li, Y. et al. Growth of conformal graphene cages on micrometre-sized silicon particles as stable battery anodes. Nature Energy 1, doi:10.1038/nenergy.2015.29 (2016).

82 Orts-Gil, G., Natte, K. & Österle, W. Multi-parametric reference nanomaterials for toxicology: state of the art, future challenges and potential candidates. RSC Advances 3, doi:10.1039/c3ra42112k (2013).

83 Yi, R., Dai, F., Gordin, M. L., Sohn, H. & Wang, D. Influence of Silicon Nanoscale Building Blocks Size and Carbon Coating on the Performance of Micro-Sized Si-C Composite Li-Ion Anodes. Advanced Energy Materials 3, 1507-1515, doi:10.1002/aenm.201300496 (2013).

84 Chae, S. et al. Micron-sized Fe–Cu–Si ternary composite anodes for high energy Li-ion batteries. Energy & Environmental Science 9, 1251-1257, doi:10.1039/c6ee00023a (2016).

85 Yi, R., Dai, F., Gordin, M. L., Chen, S. & Wang, D. Micro-sized Si-C Composite with Interconnected Nanoscale Building Blocks as High-Performance Anodes for Practical Application in Lithium-Ion Batteries. Advanced Energy Materials 3, 295-300, doi:10.1002/aenm.201200857 (2013).

86 Shen, X. et al. Research progress on silicon/carbon composite anode materials for lithium-ion battery. Journal of Energy Chemistry 27, 1067-1090, doi:10.1016/j.jechem.2017.12.012 (2018).

87 Yi, R., Zai, J., Dai, F., Gordin, M. L. & Wang, D. Dual conductive network-enabled graphene/Si–C composite anode with high areal capacity for lithium-ion batteries. Nano Energy 6, 211-218, doi:10.1016/j.nanoen.2014.04.006 (2014).

88 Pharr, M., Zhao, K., Wang, X., Suo, Z. & Vlassak, J. J. Kinetics of initial lithiation of crystalline silicon electrodes of lithium-ion batteries. Nano Lett 12, 5039-5047, doi:10.1021/nl302841y (2012).

89 Choi, Y. S., Pharr, M., Oh, K. H. & Vlassak, J. J. A simple technique for measuring the fracture energy of lithiated thin-film silicon electrodes at various lithium concentrations. Journal of Power Sources 294, 159-166, doi:10.1016/j.jpowsour.2015.06.063 (2015).

90 Cui, Z., Gao, F., Cui, Z. & Qu, J. A second nearest-neighbor embedded atom method interatomic potential for Li–Si alloys. Journal of Power Sources 207, 150-159, doi:10.1016/j.jpowsour.2012.01.145 (2012).

91 Chou, C.-Y. & Hwang, G. S. On the origin of the significant difference in lithiation behavior between silicon and germanium. Journal of Power Sources 263, 252-258, doi:10.1016/j.jpowsour.2014.04.011 (2014).

92 Zhang, Y., Li, Y., Wang, Z. & Zhao, K. Lithiation of SiO2 in Li-ion batteries: in situ transmission electron microscopy experiments and theoretical studies. Nano Lett 14, 7161-7170, doi:10.1021/nl503776u (2014).

93 McDowell, M. T. et al. Novel size and surface oxide effects in silicon nanowires as lithium battery anodes. Nano Lett 11, 4018-4025, doi:10.1021/nl202630n (2011).

94 Remediakis, I. N., Fyta, M. G., Mathioudakis, C., Kopidakis, G. & Kelires, P. C. Structure, elastic properties and strength of amorphous and nanocomposite carbon. Diamond and Related Materials 16, 1835-1840, doi:10.1016/j.diamond.2007.08.010 (2007).

95 Fan, F. et al. Mechanical properties of amorphous LixSi alloys: a reactive force field study. Modelling and Simulation in Materials Science and Engineering 21, doi:10.1088/0965-0393/21/7/074002 (2013).

96 Luo, L. et al. Surface Coating Constraint Induced Self-Discharging of Silicon Nanoparticles as Anodes for Lithium Ion Batteries. Nano Lett 15, 7016-7022, doi:10.1021/acs.nanolett.5b03047 (2015).

97 Son, Y. et al. Quantification of Pseudocapacitive Contribution in Nanocage-Shaped Silicon–Carbon Composite Anode. Advanced Energy Materials 9, doi:10.1002/aenm.201803480 (2019).

98 Choi S., Nam G., Chae S., Kim D., Kim N., Kim W., Ma J., J. Sung, Han S., Ko , Lee H., Cho J., Robust Pitch on Silicon Nanolayer–Embedded Graphite for Suppressing Undesirable Volume Expansion, Advanced Energy Materials 9, DOI: 10.1002/aenm.201803121 (2019).

99 Zhang W., Cai T., Sheldon B., The Impact of Initial SEI Formation Conditions on Strain-Induced Capacity Losses in Silicon Electrodes, Advanced Energy Materials, 9, DOI: 10.1002/aenm.201803066 (2019)

100 Liang G., Qin X., Zou K., Luo L., Wang Y., Wu M., Zhu H., Chen G., Kang F., Li B., Electrosprayed silicon-embedded porous carbon microspheres as lithium-ion battery anodes with exceptional rate capacities, Carbon, 127 *doi:10.1016/j.carbon.2017.11.013. (2018)

101 Ma, J. et al. Towards maximized volumetric capacity via pore-coordinated design for large-volume-change lithium-ion battery anodes. Nat Commun 10, 475, doi:10.1038/s41467-018-08233-3 (2019).

102 Chen, Q. & Sieradzki, K. Spontaneous evolution of bicontinuous nanostructures in dealloyed

Li-based systems. Nat Mater 12, 1102-1106, doi:10.1038/nmat3741 (2013).

103 Zeng, Z. et al. Non-flammable electrolytes with high salt-to-solvent ratios for Li-ion and Li-metal batteries. Nature Energy, doi:10.1038/s41560-018-0196-y (2018).

104 Fang, C. et al. Quantifying inactive lithium in lithium metal batteries. Nature 572, 511-515, doi:10.1038/s41586-019-1481-z (2019).

105 Zhao, J. et al. Air-stable and freestanding lithium alloy/graphene foil as an alternative to lithium metal anodes. Nat Nanotechnol 12, 993-999, doi:10.1038/nnano.2017.129 (2017).

106 Li, N. et al. Suppressing Dendritic Lithium Formation Using Porous Media in Lithium Metal-Based Batteries. Nano Lett, doi:10.1021/acs.nanolett.8b00183 (2018).

107 Wu, J. et al. Electrolyte with boron nitride nanosheets as leveling agent towards dendrite-free lithium metal anodes. Nano Energy 72, doi:10.1016/j.nanoen.2020.104725 (2020).

108 Xu, W. et al. Lithium metal anodes for rechargeable batteries. Energy Environ. Sci. 7, 513-537, doi:10.1039/c3ee40795k (2014).

109 Liu, W., Lin, D., Pei, A. & Cui, Y. Stabilizing Lithium Metal Anodes by Uniform Li-Ion Flux Distribution in Nanochannel Confinement. J Am Chem Soc 138, 15443-15450, doi:10.1021/jacs.6b08730 (2016).

110 Sun, Y. et al. Graphite-Encapsulated Li-Metal Hybrid Anodes for High-Capacity Li Batteries. Chem 1, 287-297, doi:10.1016/j.chempr.2016.07.009 (2016).

111 Tian, H. et al. Theoretical Investigation of 2D Layered Materials as Protective Films for Lithium and Sodium Metal Anodes. Advanced Energy Materials 7, doi:10.1002/aenm.201602528 (2017).

112 Wang, T., Villegas Salvatierra, R., Jalilov, A. S., Tian, J. & Tour, J. M. Ultrafast Charging High Capacity Asphalt-Lithium Metal Batteries. ACS Nano 11, 10761-10767, doi:10.1021/acsnano.7b05874 (2017).

113 Xin, S. et al. Solid-State Lithium Metal Batteries Promoted by Nanotechnology: Progress and Prospects. ACS Energy Letters 2, 1385-1394, doi:10.1021/acsenergylett.7b00175 (2017).

114 Trinh, N. D. et al. An artificial lithium protective layer enables the use of acetonitrile-based electrolytes in lithium-metal batteries. Angewandte Chemie International Edition, doi:10.1002/anie.201801737 (2018).

115 Yoo, D.-J. et al. Tuning the Electron Density of Aromatic Solvent for Stable Solid-Electrolyte-

Interphase Layer in Carbonate-Based Lithium Metal Batteries. Advanced Energy Materials, doi:10.1002/aenm.201802365 (2018).

116 Yoon, G., Moon, S., Ceder, G. & Kang, K. Deposition and Stripping Behavior of Lithium Metal in Electrochemical System: Continuum Mechanics Study. Chemistry of Materials, doi:10.1021/acs.chemmater.8b02623 (2018).

117 Yan, X. et al. Bottom-top channeling Li nucleation and growth by a gradient lithiophilic 3D conductive host for highly stable Li-metal anodes. Journal of Materials Chemistry A, doi:10.1039/c9ta11311h (2020).

118 Zheng, G. et al. Interconnected hollow carbon nanospheres for stable lithium metal anodes. Nat Nanotechnol 9, 618-623, doi:10.1038/nnano.2014.152 (2014).

119 Kim, J. et al. Functionality of Dual-Phase Lithium Storage in a Porous Carbon Host for Lithium-Metal Anode. Advanced Functional Materials, doi:10.1002/adfm.201910538 (2020).

120 Son, Y. et al. Quantification of Pseudocapacitive Contribution in Nanocage-Shaped Silicon–Carbon Composite Anode. Advanced Energy Materials 9, doi:10.1002/aenm.201803480 (2019).

121 Ma, J. et al. Strategic Pore Architecture for Accommodating Volume Change from High Si Content in Lithium-Ion Battery Anodes. Advanced Energy Materials 10, doi:10.1002/aenm.201903400 (2019).

122 Fan, Y., Chen, X., Legut, D. & Zhang, Q. Modeling and theoretical design of next-generation lithium metal batteries. Energy Storage Materials 16, 169-193, doi:10.1016/j.ensm.2018.05.007 (2019).

123 Zheng, J. et al. Regulating electrodeposition morphology of lithium: towards commercially relevant secondary Li metal batteries. Chem Soc Rev, doi:10.1039/c9cs00883g (2020).

124 Zhan, H. et al. Toward Real-time Monitoring Lithium Metal Growth and Early Dendrite Formation Surveillance for Safe Lithium Metal Batteries. Journal of Materials Chemistry A, doi:10.1039/d0ta01525c (2020).

125 Xiao, J. et al. In-Situ Formed Protecting Layer from Organic/Inorganic Concrete for Dendrite-Free Lithium Metal Anodes. Nano Lett, doi:10.1021/acs.nanolett.0c01085 (2020).

126 Wang, T. S. et al. Regulating Uniform Li Plating/Stripping via Dual-Conductive Metal-Organic Frameworks for High-Rate Lithium Metal Batteries. Advanced Functional Materials,

doi:10.1002/adfm.202000786 (2020).

127 Wang, S., Qu, J., Wu, F., Yan, K. & Zhang, C. Cycling Performance and Kinetic Mechanism Analysis of Li Metal Anode in Series Concentrated Ether Electrolyte. ACS Appl Mater Interfaces, doi:10.1021/acsami.9b23251 (2020).

128 Yan, K. et al. Selective deposition and stable encapsulation of lithium through heterogeneous seeded growth. Nature Energy 1, doi:10.1038/nenergy.2016.10 (2016).

129 Huang, G. et al. Lithiophilic 3D Nanoporous Nitrogen-Doped Graphene for Dendrite-Free and Ultrahigh-Rate Lithium-Metal Anodes. Adv Mater, e1805334, doi:10.1002/adma.201805334 (2018).

130 Zhang, R. et al. Lithiophilic Sites in Doped Graphene Guide Uniform Lithium Nucleation for Dendrite-Free Lithium Metal Anodes. Angew Chem Int Ed Engl 56, 7764-7768, doi:10.1002/anie.201702099 (2017).

131 Luo, L., Li, J., Yaghoobnejad Asl, H. & Manthiram, A. A 3D Lithiophilic Mo2 N-Modified Carbon Nanofiber Architecture for Dendrite-Free Lithium-Metal Anodes in a Full Cell. Adv Mater, e1904537, doi:10.1002/adma.201904537 (2019).

132 Chen, L. et al. High-Energy Li Metal Battery with Lithiated Host. Joule, doi:10.1016/j.joule.2018.11.025 (2018).

133 Shi, H. et al. Conducting and Lithiophilic MXene/Graphene Framework for High-Capacity, Dendrite-Free Lithium-Metal Anodes. ACS Nano, doi:10.1021/acsnano.9b07710 (2019).

134 Wu, S. et al. Lithiophilic Cu-CuO-Ni Hybrid Structure: Advanced Current Collectors Toward Stable Lithium Metal Anodes. Adv Mater 30, doi:10.1002/adma.201705830 (2018).

135 Yu, B., Tao, T., Mateti, S., Lu, S. & Chen, Y. Nanoflake Arrays of Lithiophilic Metal Oxides for the Ultra-Stable Anodes of Lithium-Metal Batteries. Advanced Functional Materials, doi:10.1002/adfm.201803023 (2018).

136 Jin, C. et al. 3D lithium metal embedded within lithiophilic porous matrix for stable lithium metal batteries. Nano Energy 37, 177-186, doi:10.1016/j.nanoen.2017.05.015 (2017).

137 Yang, C. et al. Ultrafine Silver Nanoparticles for Seeded Lithium Deposition toward Stable Lithium Metal Anode. Adv Mater 29, doi:10.1002/adma.201702714 (2017).

138 Pu, J. et al. Interlayer Lithium Plating in Au Nanoparticles Pillared Reduced Graphene Oxide for Lithium Metal Anodes. Advanced Functional Materials 28, doi:10.1002/adfm.201804133

(2018).

139 Ji, X. et al. Spatially heterogeneous carbon-fiber papers as surface dendrite-free current collectors for lithium deposition. Nano Today 7, 10-20, doi:10.1016/j.nantod.2011.11.002 (2012).

140 Deng, W., Zhu, W., Zhou, X., Zhao, F. & Liu, Z. Regulating capillary pressure to achieve ultralow areal mass loading metallic lithium anodes. Energy Storage Materials, doi:10.1016/j.ensm.2019.02.027 (2019).

141 Zhang, H. et al. Lithiophilic-lithiophobic gradient interfacial layer for a highly stable lithium metal anode. Nat Commun 9, 3729, doi:10.1038/s41467-018-06126-z (2018).

142 Pu, J. et al. Conductivity and lithiophilicity gradients guide lithium deposition to mitigate short circuits. Nat Commun 10, 1896, doi:10.1038/s41467-019-09932-1 (2019).

143 Wang, H. et al. Wrinkled Graphene Cages as Hosts for High-Capacity Li Metal Anodes Shown by Cryogenic Electron Microscopy. Nano Lett, doi:10.1021/acs.nanolett.8b04906 (2019).

144 Lee, Y.-G. et al. High-energy long-cycling all-solid-state lithium metal batteries enabled by silver–carbon composite anodes. Nature Energy, doi:10.1038/s41560-020-0575-z (2020).

145 Cheng, X. B., Zhang, R., Zhao, C. Z. & Zhang, Q. Toward Safe Lithium Metal Anode in Rechargeable Batteries: A Review. Chem Rev 117, 10403-10473, doi:10.1021/acs.chemrev.7b00115 (2017).

146 Zhang, R. et al. Advanced Micro/Nanostructures for Lithium Metal Anodes. Adv Sci (Weinh) 4, 1600445, doi:10.1002/advs.201600445 (2017).

Acknowledgement

배터리를 공부해보고 싶다는 생각 하나로 멀고먼 울산까지, 한국 최고의 배터리 연구실을 찾아온 것도 벌써 4년이 흘렀습니다. 정신없이 하루하루를 배우고 고민하는 사이 어느덧 끝나지 않을 것만 같았던 7년간의 대학원 과정을 마무리할 수 있게 되었습니다. 지나올 때는 힘들고 괴롭던 시간들이 많았던 것 같은데 돌이켜보니 즐거운 기억들이 더 많이 떠오릅니다. 아마도 제 곁에서 많은 감사한 분들이 좋은 영향을 주신 덕분이 아닐까 싶습니다. 짧은 지면이지만 대학원 생활의 마침표를 앞두고 감사의 인사를 전하고자 합니다.

먼저, 지도 교수님이신 조재필 교수님께 진심으로 깊은 감사의 인사를 드립니다. UNIST에서 박사과정을 하고싶다는 마음으로 찾아 뵀을 때 교수님께서 보여주신 밝은 미소가 여전히 선명합니다. 교수님을 생각하면 항상 그 모습이 기억날 것 같습니다. 언제나 한결 같은 모습과 열정을 보여주신 교수님의 많은 것을 본받기 위해 노력해온 4년의 시간이 박사로서 성장할 수 있었던 밑거름이라고 생각합니다. 무엇보다도, 이미 많은 것들 것 이루셨음에도 끊임없이 도전하시는 모습을 통해서 크게 감명받았고 참된 공학자, 엔지니어가 어떤 것인지 직접 보여주셔서 더 많이 배울 수 있었습니다. 또, 한국 최고의 배터리 연구실을 구축하셨고 그 안에서 많은 배움의 기회를 허락해 주심에 감사드립니다. 졸업 후 어느곳에서도 교수님의 명성에 누가 되지 않는 단단한 공학박사가 되도록 끊임없이 노력하겠습니다. 표현에 서툴러서 이제서야 감사의 인사를 드리게 된 것이 가장 아쉽게 느껴지지만 항상 존경의 마음과 감사의 마음을 갖고 있었습니다. 다시 한 번 감사합니다.

바쁘신 와중에도, 저의 박사 학위 심사를 맡아 주신 송현곤 교수님, 최남순 교수님, 정경민 교수님, 그리고 김성엽 교수님께도 깊은 감사의 인사를 전합니다. 교수님들께서 해주신 날카로운 비판과 조언이 있었기 때문에, 저의 연구 방향을 바르게 설정하고 완성도 있는 학위논문을 작성할 수 있었습니다. 감사드리며 더 발전하는 연구자가 되도록 더욱 노력하겠습니다.

첫 UNIST에 발걸음이 닿았을 때, 만났던 음극팀의 큰 형 손영욱 선배의 따뜻한 마음은 언제나 그리울 것 같아요. 카리스마 넘치는 규태, 울산에서의 첫 식사를 함께해준 지영이 형 감사합니다. 그리고 우리 음극팀의 멋진 동기들! 음극을 든든히 지켜준 최고의 팀장 수종 씨! 처음 오피스에서 짝꿍 자리였는데, 좋았습니다! 묵직하고 든든하고 뭐든 다해주는 다 알고 있는 우리 남형이! 박사과정에 ‘빨간맛’이라는 명곡을 알려줬는데, 얼른 포닥 마치고 돌아와서 함께 합시다. 부족한 형인데 참 좋아해준 성현이, 앞으로는 진짜 형 다운 모습을 더 많이 보여 줄게! 내 기억의 마지막 NESM 캡틴 승규, 멋진 영국생활 마무리하고 얼른 돌아와~! 그리고 유일한 박사과정 친구 재경이. 처음 울산에 왔을 때부터 잘 적응할 수 있게 도와줬고 언제나 마음의 위안을 줬는데, 더 쓰다 보면 울 것만 같아서 여기까지. 이제는 말하지 않아도 아는 그런 친구가 된 것 같은데, 맞나? 같이

졸업하게 돼서 너무 좋다!! 언제나 함께하는 시간이 즐거운 진정한 연구자 명승준 선배, 핵심을 콕콕 찌르는 동기 웅래씨, 항상 선하고 밝은데 조금만 더 재밌었으면 좋을 것 같은 재찬이 많은 시간을 함께하지 못해서 아쉽습니다. 이제는 친동생인 것만 같은 우영이, 따로 대화를 너무 많이 하기 때문에 감사인사는 생략한다. NESM 최고 인재 형연이, 니가 없는 우리 연구실은 왠지 상상이 잘 안된다. 홍일점으로 나이 많은 오빠들하고 시간 보낸다고 고생이 많아. 미국에서 보자! 너무 늦게 친해져서 아쉬운 우리 재성이. 좀 더 일찍 재성이를 알았더라면 나의 박사과정은 더 행복했을 텐데. 나와 UNIST에 함께 도착한 기홍이, 그때나 지금이나 진짜 늘 한결같은! 잘 준비해서 졸업까지 잘 마무리하길 바란다! 그리고 우리 막내 태용이, 7살이나 차이나는 나이든 선배하고 같이 한다고 고생 많았는데 마지막까지 그토록 원하는 후배를 맞이하지 못해서 안타깝네. 가장 멋진 졸업생으로 졸업하길! 팀도 다르고 너무 바빠서 많은 시간을 함께하지 못해 아쉬운 NESM 터미네이터 준혁이, 효명이. 너희들의 미래는 반드시 멋질 것이다! 많은 시간을 함께하지 못한 윤지, 지은, 주원, 영빈, 슬기, 예현이. 먼저 다가가지 못한 선배라 미안하네.

그리고 함께 연구실 생활을 하지 못했음에도 항상 좋은 말씀해주시는 모든 선배님들 정말 감사합니다.

끝으로, 언제나 믿고 지지해 주시고 말없이 힘이 되어 주신, 항상 아들 걱정과 기도만 하시는 가장 사랑하는 부모님께 무한한 감사를 드립니다. 남은 효도는 앞으로 더 많이 하겠습니다. 그리고 아들의 빈자리까지 가득 채워주는 우리 누나 고맙고 미안하고 사랑해. 우리 가족 모두 사랑합니다.